



UNIVERSIDAD DE CHILE
FACULTAD DE CIENCIAS FÍSICAS Y MATEMÁTICAS
DEPARTAMENTO DE INGENIERÍA ELÉCTRICA

DESIGN, IMPLEMENTATION AND CHARACTERIZATION OF A RADIO
FREQUENCY INTERFERENCE DIGITAL ADAPTIVE FILTER USING A
FIELD-PROGRAMMABLE GATE ARRAY

TESIS PARA OPTAR AL GRADO DE MAGÍSTER EN CIENCIAS DE LA
INGENIERÍA, MENCIÓN ELÉCTRICA

FRANCO ANDREAS CUROTTO MOLINA

PROFESOR GUÍA:
RICARDO ALBERTO FINGER CAMUS

MIEMBROS DE LA COMISIÓN:
PATRICIO MENA MENA
RODRIGO REEVES DÍAZ

Este trabajo ha sido financiado por CONICYT a través de sus programas: Fondo Basal,
Proyecto PBF06, ALMA CONICYT 31150012 y FONDECYT 1140428.

SANTIAGO DE CHILE

2019

RESUMEN DE LA TESIS PARA OPTAR
AL GRADO DE MAGÍSTER EN CIENCIAS DE LA INGENIERÍA, MENCIÓN ELÉCTRICA
POR: FRANCO ANDREAS CUROTTO MOLINA
FECHA: 2019
PROF. GUÍA: RICARDO ALBERTO FINGER CAMUS

DESIGN, IMPLEMENTATION AND CHARACTERIZATION OF A RADIO
FREQUENCY INTERFERENCE DIGITAL ADAPTIVE FILTER USING A
FIELD-PROGRAMMABLE GATE ARRAY

En las últimas décadas ha habido un crecimiento exponencial en el uso de sistemas de comunicación inalámbrica, tanto en el mercado del consumidor como en el empresarial. Esto ha tenido como efecto secundario el que muchos radio telescopios se ven afectados por interferencia en radio frecuencia. El nivel de daño que puede causar la interferencia va desde corromper un pequeño porcentaje de los datos, a imposibilitar completamente las observaciones astronómicas en ciertas bandas de frecuencia.

A lo largo de los años, astrónomos e ingenieros han desarrollado varias técnicas de mitigación para combatir este tipo de interferencia, desde legislaciones para prohibir emisiones cerca del sitio del telescopio, a herramientas de software para etiquetar y borrar la interferencia en datos astronómicos. En este trabajo, un método de mitigación en tiempo real es desarrollado, basado en el concepto matemático del filtro adaptativo. Para usar un filtro adaptativo, se toma una segunda medida de la interferencia con una antena de referencia, y los parámetros del filtro se ajustan para cancelar ambas copias de la interferencia. Este método tiene la ventaja de ser capaz de eliminar la interferencia sin incurrir en pérdida de datos.

El desarrollo matemático del filtro es estudiado, y se prueba que el filtro es capaz de eliminar cualquier tipo de interferencia, siempre y cuando los caminos que tome la interferencia hacia el telescopio y la antena de referencia cumplan la condición de linealidad e invariancia en el tiempo. Las limitaciones del filtro también son analizadas, y se concluye que el efecto que más daña el desempeño del filtro es la presencia de señales adicionales en la antena de referencia, no correlacionadas con la señal de interferencia. Estas señales pueden provenir del ruido de los componentes del receptor, de otras fuentes de interferencia, o de efectos de propagación multicamino.

El filtro es implementado en una FPGA para alcanzar una alta velocidad y ancho de banda, y es probado tanto en un montaje de laboratorio, como en un telescopio. Se prueba que, a pesar de que el filtro funciona excelentemente bien en condiciones controladas de laboratorio, su desempeño se degrada significativamente en el escenario realista, específicamente porque todas las limitaciones prácticas son más predominantes en este caso. De todas maneras, el filtro es capaz de atenuar la interferencia con distintos grados de éxito dependiendo de las características de la señal, principalmente potencia y efectos de propagación. Para las mejores condiciones de interferencia (alta potencia, fuente localizada, y sin efectos de propagación multicamino), el filtro demostró ser capaz de eliminar señales de interferencia de 15 dB de potencia por sobre el piso de ruido.

RESUMEN DE LA TESIS PARA OPTAR
AL GRADO DE MAGÍSTER EN CIENCIAS DE LA INGENIERÍA, MENCIÓN ELÉCTRICA
POR: FRANCO ANDREAS CUROTTO MOLINA
FECHA: 2019
PROF. GUÍA: RICARDO ALBERTO FINGER CAMUS

DESIGN, IMPLEMENTATION AND CHARACTERIZATION OF A RADIO
FREQUENCY INTERFERENCE DIGITAL ADAPTIVE FILTER USING A
FIELD-PROGRAMMABLE GATE ARRAY

In the last decades, there has been an exponential growth in the use of wireless communication systems, both in the consumer and the industry market. This has had the side effect that many radio telescopes are affected by radio frequency interference. The level of damage by interference ranges from corrupting a small percentage of data, to completely preventing astronomical observations in certain bands.

Over the years, radio astronomers and engineers have developed several mitigation techniques to deal with this type of interference, from legislation to ban emissions near telescopes sites, to offline software tools to flag and delete the interference in astronomical data. In this work, a real-time mitigation method is developed, based on the mathematical concept of adaptive filters. In an adaptive filter setup, a second measurement of the interference is taken with a reference antenna, and the filter parameters are tuned in order to properly cancel out both interference copies. The method has the advantage of being able to remove the interference without incurring in any data loss.

The mathematical derivation of the filter is studied, and it is proven that the filter should remove any type of interference, granted that the paths the interference take to the telescope and reference antenna satisfy the linear time-invariant condition. The filter limitations are also analyzed, and it is concluded that the effect that harms the filter performance the most is the presence of a additional signals at the reference antenna, uncorrelated with the interference signal. These signals can come from the noise of the receiver components, from other interference sources, or from multipath propagation effects.

The filter is implemented in an FPGA to achieve high speed and bandwidth, and then is tested, both in a laboratory setup, and with a telescope. It is shown that while the filter works very well in controlled laboratory conditions, its performance degrades significantly in the realistic scenario, specifically because the practical limitations become more prevalent in this case. Nevertheless, the filter is still able to attenuate the interference with a variable degree of success depending on the signal characteristics, mainly power and propagation effects. For the best conditions of interference (high power, localized source, and without multipath effects), the filter proved to be capable of eliminating interference signals of 15 dB of power over the noise floor.

*A mi padres,
por su paciencia y comprensión*

Acknowledgments

First and foremost, I want to thank my professor, Ricardo Finger, for the opportunity to work in the challenging and thrilling field of astronomical instrumentation. I'm very grateful for all his help and guidance during the course of this work.

I would also like to thank my coworkers at the MWL laboratory, Camilo, Christopher, David, Pablo, and Rocío, for all their support, both technical and moral, and for all the quality time that helped me to relax whenever I was stressed the most. Thanks to José for his professional help with the mechanical part of this work, in particular, the construction of the analog plate.

I want to give special thanks to my 'assistant' Daniel Bravo, for his help with the installation of the SRT's wiring, and the practical experiments with the telescope, for which he helped me even on a Saturday!

Finally, I want to thank my family and friends, for their unconditional support and patience in this long journey that was my master thesis.

Contents

List of Tables	xiii
List of Figures	xiv
1 Introduction	1
1.1 Motivation	1
1.2 Hypothesis	2
1.3 Objectives and Scope	2
1.3.1 General Objective	2
1.3.2 Specific Objectives	3
1.3.3 Scope of the Work	3
1.4 Thesis Outline	3
2 Review of RFI Mitigation Techniques	4
2.1 Pro-active Methods	4
2.1.1 Radio Quiet Zones	4
2.1.2 Reserved Frequency Bands	5
2.1.3 Others Pro-active Methods	6
2.2 Analog Methods	7
2.2.1 Interferometers and Null Steering	7
2.2.2 High Linearity Components and Radio Frequency Filters	8
2.3 Digital Offline Methods	9
2.3.1 Thresholding and Statistical Methods	9
2.3.2 Machine Learning Methods	10
2.4 Digital Real-time Mitigation Methods	10
2.4.1 Thresholding	11
2.4.2 Spectral Kurtosis	11
2.4.3 Adaptive Filters	12
2.4.4 Subtraction Without a Reference Antenna	13
2.4.5 Other Methods	14
2.5 Summary	14
3 Theoretical Framework	15
3.1 Adaptive Filters	15
3.2 Adaptive Filters in Frequency Domain	16
3.3 Frequency Domain Interference Cancellation	16
3.3.1 Analog Case	16

3.3.2	Analog Sinusoid Case	18
3.4	Frequency-Domain Adaptive Filter Implementation	20
3.4.1	Signal Digitization	20
3.4.2	Cross-Correlation Computation	21
3.4.3	Adaptive Algorithm	21
3.4.4	Mathematical Derivation of the Adaptive Algorithm	23
3.5	Summary	25
4	Adaptive Filter Limitations	27
4.1	Digitization Effects	27
4.1.1	Time Quantization	27
4.1.2	Amplitude Quantization	28
4.1.3	Frequency Quantization	29
4.2	Effect of Noise	29
4.3	Multiple RFI Sources	31
4.4	Effect of Multipath Propagation	34
4.5	Violation of LTI Condition	36
4.6	Summary	36
5	Hardware Implementation and Results	37
5.1	Hardware Description	37
5.1.1	Field-Programmable Gate Arrays	37
5.1.2	ROACH2	38
5.2	Hardware Implementation	41
5.3	Results	43
5.3.1	Laboratory Tests	43
5.3.2	FM Radio Tests	47
5.3.3	Radio Telescope Tests	50
5.4	Summary	59
6	Conclusions	60
	Mathematical Symbols	62
	Acronyms	64
7	Bibliography	67
8	Appendix	71
8.1	Mathematical Derivation of the Adaptive Filter for Multiples RFI	71
8.2	ROACH2-rev2 Block Diagram	75
8.3	List of Datasheets	76
8.3.1	ROACH2 Hardware	76
8.3.2	Laboratory Test Components	77
8.3.3	SRT Test Components	78
8.4	ISE Design Suite Device Utilization Report	79
8.5	RFI Filter Model Figures	85

List of Tables

3.1	Relation between accumulation cycle index n and update cycle index i	23
5.1	Virtex-6 device utilization summary for the adaptive filter model.	42
8.1	ROACH2 Components.	76
8.2	Laboratory Test Components.	77
8.3	SRT Test Components.	78

List of Figures

2.1	List of RFI mitigation techniques in radio astronomy.	5
2.2	Radio Quiet Zones examples.	6
2.3	Radiation pattern example.	8
2.4	Adaptive filter in interference cancellation setup.	12
2.5	Time and frequency domain adaptive filters.	13
3.1	Basic adaptive filter setup.	16
3.2	Theoretical analog non-adaptive filter.	17
3.3	FDAF diagram.	20
3.4	Illustration of CW phasors and their cross-spectrum.	22
3.5	RFI filter simulated tests.	25
4.1	Visual demonstration of the aliasing effect.	28
4.2	Visual demonstration of the frequency quantization effect.	29
4.3	Illustration of the filter behavior under high noise conditions.	32
4.4	Two RFI sources scenario.	33
4.5	Illustration of the filter behavior for multiple RFI sources.	33
4.6	Illustration of the multipath problem.	34
4.7	Example of two signals produced by multipath.	35
5.1	Simple FPGA diagram.	38
5.2	iCE40 FPGA logic cell.	39
5.3	Virtex-6 FPGA DSP block.	39
5.4	Image of the ROACH2-rev2 board.	40
5.5	Designed Non-stop vector accumulator block.	43
5.6	Laboratory test setup.	44
5.7	Spectrum of astronomical signal for the laboratory test.	44
5.8	Spectra of the interference signals for the laboratory test.	45
5.9	Test results for the broadband noise RFI.	45
5.10	Test results for the multi-carrier RFI.	45
5.11	Power difference between the astronomical signal and the RFI.	46
5.12	Convergence speed for the broadband noise and the multi-carrier RFI.	46
5.13	Decimation FIR filter frequency response.	47
5.14	The three different locations for the FM radio tests.	48
5.15	Spectra of FM radio tests.	49
5.16	Attenuation ratio v/s distance for all the location tested.	50
5.17	MIT Small Radio Telescope.	51

5.18	Reference antenna.	51
5.19	SRT analog front-end diagram used for the beamwidth test.	52
5.20	Plate with the analog front-end amplification chain.	52
5.21	Illustration of the undersampling technique.	53
5.22	Radio Astronomy Supplies bandpass filters.	54
5.23	SRT test with low power RFI.	55
5.24	SRT test with high power RFI.	56
5.25	SRT test with narrowband RFI.	57
5.26	SRT test with walkie-talkie RFI.	58
8.1	ROACH2-rev2 block diagram.	75
8.2	RFI filter full model.	85
8.3	RFI filter spectrometer model.	86
8.4	Adaptive filter model.	87
8.5	RFI filter model for the FM test.	88

Chapter 1

Introduction

1.1 Motivation

One of the most challenging problems cm-wave astronomy have to face in present days is dealing with *radio frequency interference* (RFI). In radio astronomy, RFI is defined as any unwanted signal that has the potential to degrade or prevent the successful conduct of an observation. It is usually produced by telecommunication systems, man made RADARs, or unexpected emissions from electronic equipment.

Unlike thermal noise, which has a statistic behavior that is modeled as additive white Gaussian noise (AWGN), RFI usually has a complex time and frequency structure and can vary unpredictably over time, so it cannot be reduced by long integration (accumulation) times. Furthermore, all common telecommunication signals are many orders of magnitude higher in power than astronomical signals, so even the tiniest leakage of power from an RFI source to a radio telescope can degrade significantly an observation. As an example, a standard GSM mobile phone transmitting 0.5 W at 1.8 GHz at a distance of 1 km generates a flux of 110 000 000 Jy¹. In contrast, modern radio telescopes have the sensitivity to measure signals with fluxes as small as 10^{-3} Jy, a difference of 11 orders of magnitude [1].

There are many different types of RFI that can affect a radio telescope. Unintentional emissions like corona discharges in transmission lines and automobile ignitions produce broadband interference that is short in time and impulse-like. Conventional telecommunication systems like radio broadcasting (AM, FM), satellite transmission (GPS), two-way radio links (walkie-talkies), and radio navigation systems, typically use narrowband communication schemes that are persistent in time. Modern spread-spectrum technologies (cellular 3G and 4G networks) pose a significant problem for radio telescopes as their emission covers a relatively wide band, is very fast changing, and can last for long periods of time.

The amount of RFI in the environment, and the damage it produces to observations, is such that it has forced astronomers and engineers to develop a large number of RFI mitigation

¹Jansky (Jy) is a measure of spectral flux density, $1 \text{ Jy} = 10^{-26} \frac{\text{W}}{\text{m}^2\text{Hz}}$.

techniques. Although the most common procedure to deal with RFI is manual labeling and blanking, nowadays there are several motivations to implement more automated methods:

- The exponential increase of wireless communication services that has occurred in recent years has raised the amount of interference to unprecedented levels.
- The increase in the number of celestial objects of study and the large amount of data collected by telescopes make human assisted methods practically impossible.
- The development of new algorithms, and the availability of more powerful hardware have made possible the implementation of methods that were unfeasible in the past.
- Some methods have the ability to subtract the RFI from the astronomical signal in real-time, effectively avoiding the data loss produced by blanking methods.

The purpose of RFI mitigation methods goes far beyond detecting and removing unwanted signals from astronomical data. Powerful real-time mitigation techniques can make possible observations in frequency bands and locations that otherwise would not be possible, reduce observation times, and lighten the workload in post-processing.

In spite of the obvious benefits of RFI mitigations techniques, very few of these methods beyond the simplest ones have been permanently implemented in telescope's data reduction pipelines. Radio astronomers are reluctant to incorporate 'black boxes' that can potentially corrupt the data. RFI hardware can be costly and require many work hours of design or software development. Instead, they prefer to focus their resources in enhancing the receiver parameters (bandwidth and frequency resolution), as it generally gives them more scientific payoff, and decide to work around RFI instead of combat it [2]. It is the job of the instrumentation engineers to develop robust and intuitive mitigation systems, that maintain the data as clean as possible, and produce enough benefits for a telescope to be considered for permanent usage.

1.2 Hypothesis

Modern reconfigurable computing can be used as a powerful tool to combat the growing problem of radio frequency interference in radio astronomy. In particular, a digital adaptive filter method implemented in a field-programmable gate array can effectively eliminate many types of interference signals in real-time, while at the same time avoid the data loss of typical blanking methods.

1.3 Objectives and Scope

1.3.1 General Objective

To develop, implement and test a digital adaptive filter for real-time RFI cancellation. The filter must be implemented in programmable hardware to achieve high-speed mitigation as

well as reconfigurability for different scenarios. The filter must be designed to achieve several requirements for radio astronomy in terms of bandwidth, dynamic range, and frequency resolution.

1.3.2 Specific Objectives

- Study the current RFI mitigation methods used in astronomical observatories, understand their advantages and disadvantages, and analyze how modern reconfigurable hardware can overcome their limitations.
- Study the adaptive filter theory, and its applications in interference mitigation.
- Explore the limitations of adaptive filters in the context of RFI mitigation in radio astronomy.
- Design and implement a frequency-domain adaptive filter in a field-programmable gate array. In particular, the target hardware is CASPER's ROACH2 platform.
- Test the implemented design, both in a laboratory setup and in a telescope, with real astronomical data.

1.3.3 Scope of the Work

This work is focused in the implementation and testing of an adaptive filter for RFI mitigation applications. Both the hardware platform (ROACH2) and digital signal processing libraries are already available, so only the specific adaptive filtering algorithm needs to be implemented. The testing will be done both with simulated data in laboratory conditions, and with a telescope in an astronomical experiment called *sun-pointing*. The sun-pointing is used for being a simple, repeatable experiment, and because its results can be easily validated by visual inspection. Tests in more complex astronomical experiments are left for future work. Exhaustive exploration of the optimal parameters of the filter, as well as tests with different analog components, and in locations with different levels of RFI contamination are also suggested as future work.

1.4 Thesis Outline

The rest of the document is organized as follows. In Chapter 2 a review of common RFI mitigation methods in radio astronomy is presented. Chapter 3 establishes the theoretical framework for the adaptive filter. The limitations of the filter are studied in Chapter 4. The hardware implementation, and the test results for the filter, both in simulated and real scenarios, are shown in Chapter 5. Finally, Chapter 6 presents the conclusions and the suggested future work.

Chapter 2

Review of RFI Mitigation Techniques

RFI mitigation techniques can be divided into four groups: pro-active methods, analog methods, digital real-time methods, and digital offline methods. In the next sections, a brief description of common mitigation techniques used in modern observatories is presented. See Figure 2.1 for a list of all the methods mentioned in this chapter.

2.1 Pro-active Methods

The pro-active methods aim to directly modify the behavior of the RFI sources in order to reduce their impact in the telescope. This is usually done by coordinating with the responsible of the RFI emission and the corresponding governmental authorities to define regulations that restrict the interference propagation. These regulations can be implemented at any level of geopolitical size, from the local level encompassing a small town, to worldwide standards.

2.1.1 Radio Quiet Zones

The most common pro-active measure at the local level is the implementation of *Radio Quiet Zones* (RQZs), geographical areas in which radio transmissions are heavily restricted. These areas are defined either as a radius distance around the telescope, or by specific latitude and longitude coordinates. Their sizes range from 50 to 34000 km². The amount of restriction varies between RQZs, some prohibit any type of emission at any frequency within the zone, while others ban emissions on specific frequency bands. The amount of acceptable interference power also varies, while most sites consider the thresholds defined in the Recommendation ITU-R RA.769 [3] as acceptable levels for astronomical observation, depending on the type of telescope and observation, a threshold 20 dB lower than ITU-R RA.769 may be needed. In general, strict RQZ measures allow wider types of observations, while weaker ones facilitate the use of telecommunication and other services by the observatory staff and neighbors.

RQZs can also define a second *coordination zone* in which operators who are wishing to

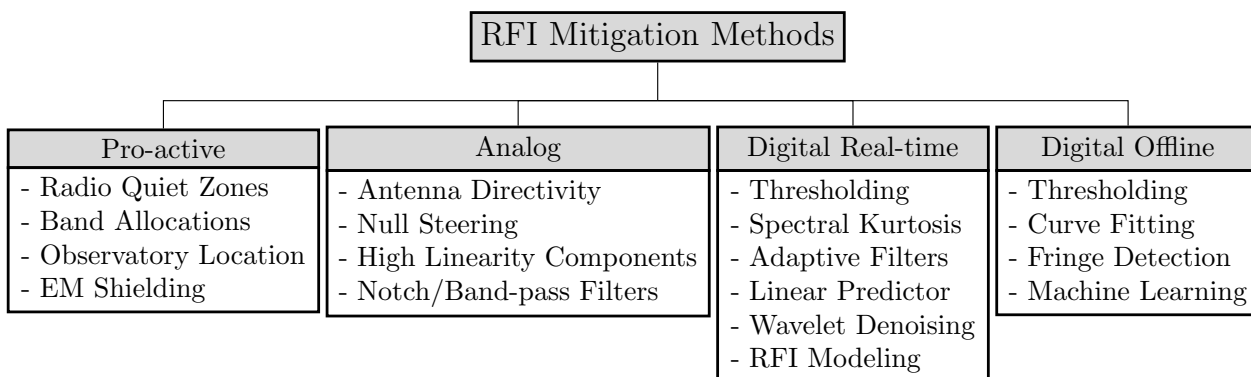


Figure 2.1: List of RFI mitigation techniques in radio astronomy.

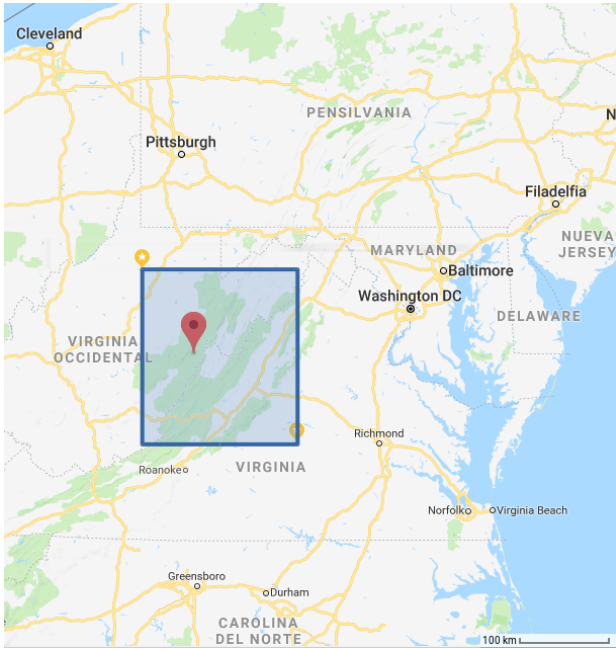
transmit on a specific frequency band are subject to coordination with the observatory. This zone is usually much greater than the original RQZ, and allows transmissions as long as it does not affect observations. To ensure the proper compliance of the RQZ norms, routine monitoring of the radio spectrum should be put in place, either by installing standalone monitoring stations, or vehicle-mounted measurement equipment. These methods are less sensitive than the radio telescope itself, so a double checking of the astronomical data should always be performed. Figure 2.2 shows two examples of operating Radio Quiet Zones. For more details on the implementation and operation for RQZ see [1].

2.1.2 Reserved Frequency Bands

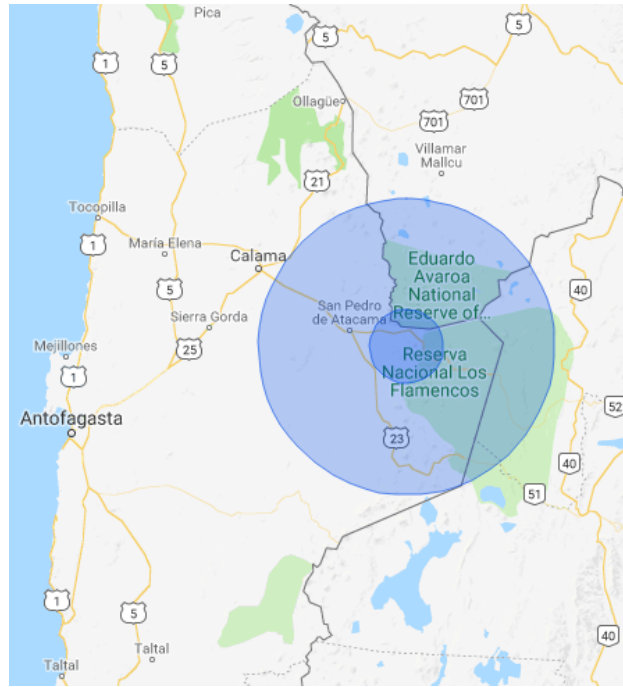
In an effort to harmonize the utilization of the electromagnetic spectrum and avoid interference between services, the International Telecommunication Union (ITU)¹, a special agency of the United Nations, coordinates the radio spectrum between 8.3 MHz and 300 GHz by dividing it into several frequency bands in which only designated services are allowed to operate [4]. Between all the bands allocated, around 70 to 80 correspond to radio astronomy (the exact amount depends on the region, and local laws). There are two types of radio astronomy bands, the ones allocated exclusively to radio astronomy (or shared with passive services), in which radio emission are strictly prohibited, and the ones shared with active services, where protection can only be partially imposed. The radio astronomy bands are selected with some scientific meaning in mind and correspond to parts of the spectrum that are of interest to astronomers. In a lot of cases, they are associated with spectral lines produced by the emission of some particular chemical substance present in space. For example, the band of 1400-1427 MHz is reserved to radio astronomy due to the hydrogen line (emission by the change of state of neutral hydrogen atoms) being located around 1420 MHz. See [5] for a comprehensive list of frequency bands of astronomical interest.

Even though emissions are prohibited in reserved bands, interference can still be present due to harmonics and power leakage from active components. For these cases, the ITU, in its ITU-R RA.769 Recommendation report [3], defines maximum acceptable interference as one that introduces an error of not more than 10% in the measured power, which is a threshold

¹<https://www.itu.int>



(a) The National Radio Quiet Zone of the United States, represented by the blue square. Comprises an area of $34\,000\text{ km}^2$, and snaps the states of West Virginia, Virginia and a small part of Maryland. The red marker indicates the Green Bank Telescope.



(b) ALMA's Radio Quiet Zone located in San Pedro de Atacama, Chile. The inner circle (30 km radius) represents the protected zone, while the outer circle (120 km radius) the coordination zone. Only Chilean territory is affected by the regulation.

Figure 2.2: Radio Quiet Zone examples. Images created with Google Maps.

that astronomers generally accept. ITU's report also presents a list of suggested thresholds for some typical astronomical bands using common telescope and observation parameters.

2.1.3 Others Pro-active Methods

A direct way to actively avoid interference is to choose a proper location for the observatory, with the most obvious choice being remote locations far away from interference sources. Natural formations, like mountains, can be effective in blocking emissions, but caution should be taken as they can as easily produce reflection and diffraction on electromagnetic waves that can worsen the interference situation, due to multipath propagation effects. Some observatories have found beneficial to surround their telescopes with coniferous trees, such as pines, as the moisture in the needles of the trees works as an absorbent for signals above 1 GHz [1]. On the other hand, some observatories are built at high altitudes in order to reduce the atmospheric absorption. This usually ensures long distances from interference sources, but also increase the chances of having line-of-site with them, so a thorough study of the location is crucial in every particular case.

Experience from telescope operators has revealed that in most cases interference sources are located within the observatory itself. The solution in this case is to cover every electronic

equipment prone to produce interference (computers, microwaves and RF components) with some kind of electromagnetic shielding. Simple methods like covering these devices in some conductive foil can be enough to suppress the interference. Room-size Faraday cages can also be built to be able to use these devices seamlessly while keeping the interference in a confined space.

In general, pro-active methods are the most effective way to deal with interference, and should always be used as a first layer of protection. Nevertheless, they still present a number of drawbacks:

- Regulations can only provide protection for a small fraction of the electromagnetic spectrum, which left behind a lot of astronomical study cases.
- Even when the protections are in place, they could be not enough for high sensitivity observations.
- There are some types of interferences that are difficult to avoid or regulate, like unlicensed radio services, and satellite communications.

Because of this limitations, every telescope must implement alternative mitigation methods.

2.2 Analog Methods

The analog methods aim to avoid the interference in the environment to enter to the telescope receiver and its digital back-end. A first layer of mitigation comes from the telescope directional radiation pattern. Since astronomers are usually interested in observing point sources, telescopes are designed to have a high angular resolution, and they point at the sky with high elevation angles, hence avoiding ground-based interference from entering through the mainlobe. However, every directional antenna suffers from the presence of sidelobes, that make unintentional measurements in different angles (see Figure 2.3). For example, parabolic antennas usually have sidelobes around 20 to 30 dB below the mainlobe. A strong enough interference picked up by the sidelobe can easily obscure an astronomical source.

2.2.1 Interferometers and Null Steering

Interferometers (array of radio telescopes) are intrinsically less affected by RFI than single dish telescopes. This is due to the fact that an interfering signal received by two widely-spaced antennas will have different relative time-delays, so they will be effectively canceled in the process of correlation. The effects of interference become significant only when they degrade the measured correlation of the signal of two antennas. It is estimated that interferometers over tens of kilometers have a protection threshold 20 dB greater than for single dish telescopes [1].

Interferometers with a large number of antennas can also implement a method called *Null Steering*. It involves controlling the delay coefficients of the interferometric array to change

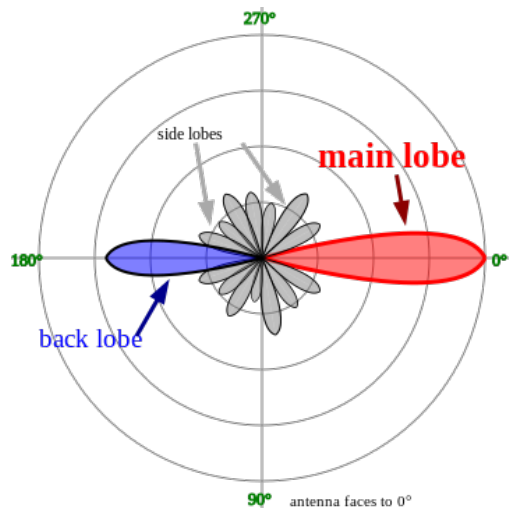


Figure 2.3: Example of radiation pattern for a typical directional antenna in polar coordinates. The mainlobe (at 0°) is the primary measurement direction for the antenna. Sidelobes are undesired, weaker measurement directions. The sidelobe at 180° is called backlobe. Directions where there is no reception are called nulls. By Timothy Truckle [CC BY-SA 4.0] (<http://creativecommons.org/licenses/by-sa/4.0>), via Wikimedia Commons².

the shape of its radiation pattern, and placing the *nulls* of the patterns in the direction of the interference. If the interference move in space (as is the case of satellites) some kind of algorithm must be put in place to automatically detect and track the source, and to dynamically compute the delay coefficients. Methods based on *minimum mean square error*, *minimum variance distortionless response* [6], *subspace estimation and projection* [7], and *genetic algorithms* [8] have been proposed for solving the tracking problem in null steering. It has been proven that for a small number of interfering sources the beam-forming algorithms can place the corresponding nulls correctly without significantly deforming the mainlobe. However, the problem becomes unfeasible for more than two RFI sources due to its increasing complexity. The tracking algorithms require a high *interference-to-noise ratio* (INR) in order to correctly detect the interference, and they expect the source to move in a relatively predictable fashion.

In general, null forming methods work better for satellites, rather than ground-based RFI, as the latter is often scattered by terrestrial obstacles. The obstacles make the interference arrive at the telescope with multiple apparent directions of incidence that cover a wide angular range. Even so, most of the null steering techniques are yet to be used in real telescopes due to their high complexity and large engineering cost associated with their implementation and design.

2.2.2 High Linearity Components and Radio Frequency Filters

The electronic components of a telescope receiver are designed to have high dynamic range, allowing them to stay in their linear region even in the presence of strong interference. For known frequency-stable RFI, like radio and TV broadcast, a notch filter can be used to

²https://en.wikipedia.org/wiki/Side_lobe#/media/File:Sidelobes_en.svg

eliminate that specific band. Conversely, band-pass filters can isolate a frequency band of interest in an environment plagued with RFI. Although analog filters can remove interference around the desired band, they are not useful if the interference has a non-static frequency behavior, or if it is located exactly at the same frequency band as the signal of interest.

2.3 Digital Offline Methods

The digital offline methods are applied at the last step of the data reduction pipeline (after accumulation and storage), just before the data is used for science. Traditionally, interference is detected in spectrogram images ‘by hand’, by performing a visual inspection in search of corrupted data spots, and labeling them accordingly. Nowadays, the volume of data recorded by telescopes is so large that makes manual labeling very time consuming and prone to error, if not impossible [9]. Instead, software-assisted methods are used in almost every observatory.

2.3.1 Thresholding and Statistical Methods

There exist several software tools to help astronomers in the detection of RFI in post-accumulation. They can be human-guided or fully-automated, and in most cases they involve some kind of thresholding (also known as flagging or blanking) and curve fitting. For example, in [10] a procedure is described to perform two-dimensional polynomial fitting in spectrogram images, by dividing the images in small windows of a few pixels. Then, a variance-based threshold is applied around the fitted 2D curve.

Other kinds of more robust thresholds have also been explored. In [11], the software `pieflag`³ uses a median filter and median absolute deviation (MAD) to flag amplitude peaks in spectrogram data. Median-base estimators are used for being robust to outliers, unlike other common estimators (mean, standard deviation) that are heavily biased towards high amplitude values. The `pieflag` software has been successfully used in the Australia Telescope Compact Array (ATCA), showing results comparable to the human eye.

The *SumThreshold* method [12, 13] uses a family of thresholds applied iteratively over the same spectrogram data. The spectrogram image is divided into overlapping windows of different sizes, the window data is added into a single value, and a specific, window dependant, threshold is applied to the value. A second step is performed where morphological operators are applied over the flagged data to cover neighbor points which are most likely also corrupted. This thresholding method has resulted in the most accurate one, and it has been incorporated in the `AOFlagger` framework⁴, which has been used extensively in many radio telescopes including LOFAR, WSRT, VLA, and GMRT.

Another interesting approach for interferometric data is presented in [14]. It uses the fact interferometer baselines create a fringe pattern in the correlated output due to Earth’s

³<https://github.com/chrishales/pieflag>

⁴<https://sourceforge.net/p/aoflagger/wiki/Home/>

rotation, which is suppressed by multiplying the data stream by a sinusoid. This process has the side effect that any source rotating at the same speed than the baseline will get modulated by the fringe stopped frequency. Fringe patterns generated by RFI sources can be detected and subtracted offline, avoiding the data loss of flagging methods. The method is extended in [15] to deal with moving, variable amplitude RFI, and implemented in the AIPS software package⁵.

2.3.2 Machine Learning Methods

Machine learning algorithms have become extremely popular in recent years for solving problems of modeling, prediction, and classification, among others. These methods try to minimize the a priori assumptions needed in statistical approaches, and instead extract all of the information directly from the data. This attribute makes machine learning methods very dependent on the size and purity of the datasets utilized.

In the field of RFI mitigation, the machine learning techniques have been scarcely used. One of the few examples is [16], where the author investigates the use of both Gaussian Mixture Models (GMM) and K-nearest neighbors (KNN) classifiers to detect RFI in data from the Square Kilometre Array (SKA) telescope. An accuracy of 87.34% and 93.2% in RFI detection was achieved for GMM and KNN, respectively.

The use of Artificial Neural Networks (ANN) as offline RFI classifiers has also been proposed, with [17] been the earliest example found. However, to the author knowledge, ANN has not been used in a real-world application for RFI mitigation in telescope data.

Offline methods are extensively used in radio astronomy because they are easy to use, they do not require expensive hardware, and they do not modify the data irreversibly. Essentially, these methods perform the data labeling that astronomers have been doing manually for years in an automatic manner. The fact that they work in accumulated data have the additional advantage that they can detect faint RFI not visible in real-time. The greatest disadvantage of flagging methods is the large amount of data loss. Even though [14] solves this issue, it only works in interferometers and it will not be effective for complex, fast-changing RFI.

2.4 Digital Real-time Mitigation Methods

Real-time mitigation methods encompass every technique implemented after signal digitization and before permanent data storage. Due to the high data sampling speed required in radio astronomy, these methods must be implemented in equally fast digital hardware. Nowadays, the most commonly used device for real-time mitigation methods are *field-programmable gate arrays* (FPGAs, see Chapter 5), for their high data throughput, large amount of resources, reconfigurability, and high parallelism capabilities. Many radio telescopes have already installed FPGAs for their primary data processing tasks, so incorporating real-time

⁵<http://www.aips.nrao.edu/index.shtml>

mitigation techniques is usually straightforward.

2.4.1 Thresholding

Similarly to how it is done offline, data thresholding can be applied in real-time. Thresholding in real-time can be done in time or frequency domain, and it has the advantage that the amount of data loss is much less than in the offline case, as it is performed before accumulation.

In [18] a simple time-domain thresholding technique is studied for pulsed type interference. The threshold is computed using the mean and standard deviation of the temporal data and implemented in FPGA hardware. More recently, the median absolute deviation (MAD) was explored as a robust threshold in [19] for interferometric data, in a similar way as it is done offline by `pieflag`. The MAD threshold was tested in recorded data in the time and frequency domain, for dealing with broadband and narrowband interference respectively.

Overall, flagging methods represent the preferred way for astronomers to mitigate RFI for their ease in design and implementation. However, it is very restricted in its mitigation capabilities, as the threshold parameters must be fine-tuned for each instance of RFI. For this reason threshold methods are normally used for persistent RFI with predictable behavior. These methods also have to define a way to replace the flagged data. Zeroing the interference has usually ill effects in posterior processing (for example, in calibration and source detection). Instead, it is preferred to replace corrupted data with some kind of artificially generated noise.

2.4.2 Spectral Kurtosis

Another kind of flagging method is proposed in [20], where an alternative statistic called *spectral kurtosis* (SK) is used. Kurtosis is a four order statistic that can be interpreted as a measure of ‘Gaussianness’ of a random variable, with a Gaussian distribution having a kurtosis equal to 0. Spectral kurtosis is the computation of kurtosis of the *Power Spectral Density* (PSD), more specifically, over every single bin of the *Discrete Fourier Transform* (DFT) output’s power. The reasoning behind this approach is that most astronomical signals behave as band-limited Gaussian noise, while most RFI has a deterministic non-Gaussian pattern. Therefore, an SK estimator can be applied as a ‘Gaussianity test’ over every individual bin in the spectral data.

In [21] the authors derived an unbiased estimator for spectral kurtosis that is easily implemented in FPGA hardware. The SK method seems effective, specially for transient, low duty cycle RFI (below 50% of appearance in a bin time-frame), but starts failing for more persistent, narrowband RFI.

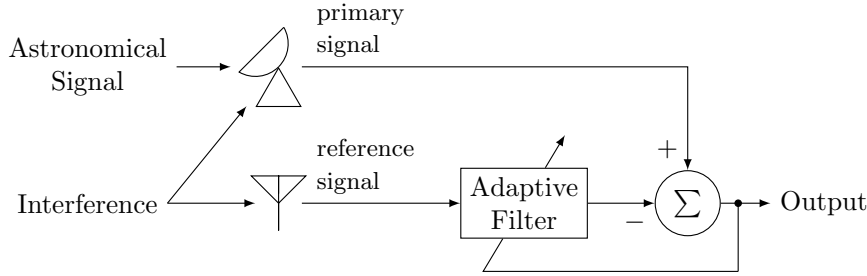


Figure 2.4: High-level diagram of an adaptive filter used in an interference cancellation setup.

2.4.3 Adaptive Filters

Apart from thresholding, there is another family of mitigation methods labeled as *waveform subtraction*. The general idea is to take a second measurement of the interference through a *reference antenna* that does not include the signal of interest. Then the signal from the telescope and from the reference antenna can get subtracted through some method in order to get a clean astronomical signal.

In general, direct subtraction is not possible as the different characteristics of the antennas and the signal paths produce a gain and phase mismatch of the signals at the receiver. Instead, a mathematical procedure is needed to adjust for the difference of both transfer functions. The more common method for this is the *Adaptive Filter* (AF). Figure 2.4 shows a high-level diagram of an adaptive filter in an interference cancellation setup. The *primary signal* contains the signal of interest plus unwanted interference. The reference signal has a second instance of the interference that is correlated with the first one in an unspecified manner. The objective of the filter is to figure out the correlation between the interferences by adjusting the filter parameters through some algorithm, effectively canceling out the interference at the output.

The first application of adaptive filters in radio astronomy is described in [22]. The authors discuss the implementation of a time domain AF for the mitigation of FM radio interference. The architecture of a time domain AF corresponds to a finite impulse response (FIR) digital filter with tunable parameters, as shown in Figure 2.5a. In this case, a nine-tap FIR filter is used, while the update algorithm minimizes the *mean squared error* (MSE) between the primary and reference signal⁶.

Frequency domain adaptive filters are also possible. In this case, the tunable parameters are complex gains values just after the DFT output, as shown in Figure 2.5b. The concept of frequency domain AF for radio astronomy is first presented in [23], and in [24] an FPGA-based implementation is proposed, and tested in the Parkes Observatory in Australia for the mitigation of a TV transmitter.

Adaptive filters represent an interesting approach for radio astronomers, as they can cancel interference without incurring in data loss, and, in theory, can deal with any kind of interference. It does, however, present several challenges, for example, it requires the addi-

⁶Adaptive filters using this type of algorithm are known as Wiener Filter.

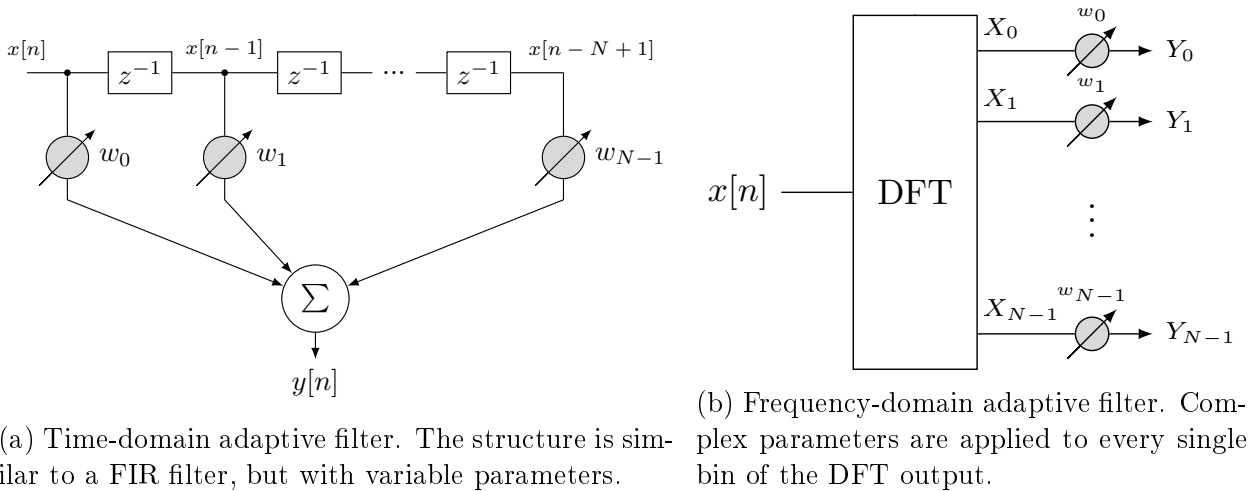


Figure 2.5: Adaptive filter diagrams in time and frequency domain. The gray circles represent the filters' parameters w which are updated by the adaptive algorithm.

tional hardware of the reference antenna that has to provide an accurate copy of the RFI entering the telescope. The AF performance is very dependent of the *interference-to-noise ratio* (INR). If the interference power is very close to the noise, the AF may not be able to cancel it completely, but it would still be visible in post accumulation. Furthermore, if the interference presents strong multipath effects, it is possible for the primary and reference measurements to be not completely correlated, making the AF not to work properly (see Chapter 4 for further discussion).

2.4.4 Subtraction Without a Reference Antenna

Other types of waveform subtraction methods have been developed, in which, by making some assumptions over the interference and/or the astronomical signal, the use of a reference antenna can be avoided. In [25], a method called *linear predictor* is implemented for RFI mitigation around the 10-100 MHz band. A linear predictor is a type of adaptive filter in which the reference input is a delayed version of the primary signal. The job of the filter is to construct an accurate model of the interference source that can predict the current input sample. Then, simple subtraction between the input signal and the predictor should yield an RFI-free signal. The main assumptions for this method are that the astronomical signal must be Gaussian, so that it does not get modeled by the predictor, and that the number of taps of the filter is enough to accurately model the interference, which is usually hard to estimate for complex multi-carrier signals.

Another similar approach is proposed in [26] with use of the *wavelet transform*. The discrete wavelet transform (DWT) is a type of signal decomposition based on localized component waves of variable duration (wavelets). The DWT can be used to decompose a signal into a primary trend, and a series of fluctuation components. In RFI mitigation applications, the lower level fluctuations (representing the signal noise) can be discarded to retrieve a denoised version of the interference. Assuming the desired signal behaves as white noise, the

original and denoised signal can get subtracted to obtain an RFI-free astronomical signal, in a similar way as the linear predictor. For this technique, only results for offline astronomical data [26], and for real-time simulated data [27] were found in the bibliography.

2.4.5 Other Methods

The use of *ad hoc* methods to deal with specific, well-known interference sources has also been studied. In [28] a parametric model is developed to very precisely predict one of the modulations of the Russian GLONASS satellite navigation system, thanks to its publicly known communication scheme. The method provides the advantage of achieving very good cancellation without introducing additional noise. The model is tested offline via software, but its implementation in modern hardware is straightforward, and can be applied for many kinds of interferences, like GPS and CDMA, as long as the communication scheme is known.

2.5 Summary

It has been shown that radio astronomers and engineers have developed several RFI mitigation techniques. In most cases, these techniques are thought for a very particular context, in terms of the type of telescope, interference, and observation. It is generally accepted that an ‘all in one’ method that can deal with any type of interference does not exist, but a good mitigation system can be built using a combination of these methods in different stages of the data reduction pipeline. Nevertheless, there is still a long way for most of these methods to be deployed in radio telescopes, as astronomers see more beneficial to spend their time, money and effort in projects with more direct scientific results.

Chapter 3

Theoretical Framework

In this chapter, the theoretical framework of the adaptive filter to be implemented is discussed, with an emphasis on the mathematical justification, and quantitative analysis.

3.1 Adaptive Filters

In general, an adaptive filter is a digital system whose transfer functions is modified over time by means of an adaptive algorithm. The most common example of an adaptive filter is a typical FIR filter with tunable parameters, as shown in Figure 2.5a. Adaptive filters become useful when the input signal of a system is difficult to model, has unknown statistics, or the statistics change rapidly over time. Depending on the configuration in which it is used, an adaptive filter can have different applications. The most common are system identification, inverse modeling, linear prediction, and interference cancellation.

In order for the adaptive filter to modify its parameters, it requires a second input, known as the desired or target signal. In the most traditional setup, the desired signal and filter output are subtracted to create the error signal, which is then fed back to the filter, as shown in Figure 3.1. The adaptive algorithm then takes the error data, and modify the filter parameters to achieve some optimization criteria, for example, minimizing the error signal power¹. The case of adaptive FIR filters has been extensively studied, and it has been proven that for signals with stationary statistics, the optimal set of parameters that minimizes the error signal power is given by the *Wiener Solution*, which is a function of the *cross-correlation* between the input and the desired signal [29]. For real applications, the correlation must be approximated using a portion of the input signals, and it must be recomputed periodically to react to changes in the signals' statistics.

¹More specifically, the mean squared error between the input signal and the desired signal.

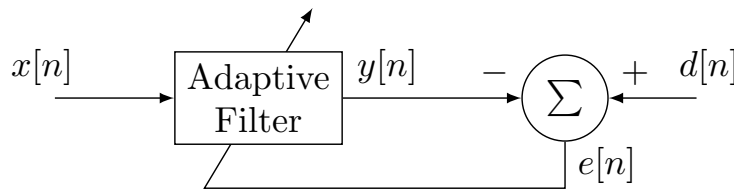


Figure 3.1: Most basic setup for an adaptive filter. The filter output $y[n]$ and the desired signal $d[n]$ are subtracted to create the error signal $e[n]$, which is then fed back to the filter.

3.2 Adaptive Filters in Frequency Domain

Alternatively to time-domain adaptive FIR filters, there exist *Frequency-Domain Adaptive Filters* (FDAF). In FDAF, the signals are converted to frequency-domain using some implementation of the Discrete Fourier Transform (DFT). Then, the adaptive algorithm is applied using the frequency version of the cross-correlation (see Section 3.4 for the details).

There are several advantages in implementing cross-correlation in frequency domain:

- Frequency correlation is more efficient than time correlation, as it is implemented using the *Fast Fourier Transform* (FFT) algorithm. This efficiency can be translated in less computational time, less digital resources, or both.
- Furthermore, if there is no need to convert the signal back to the time domain (as it is the case for spectral analysis in radio astronomy), the correlation computation only requires two FFTs and no inverse Fourier Transform.
- There are several software and hardware implementations available of the FFT algorithm, so little design effort is needed to compute the correlation.

In FDAF, the tunable parameters become complex weights applied independently to every bin of the DFT output, as shown in Figure 2.5b. The weights control the phase and amplitude of the DFT outputs in order to achieve the desired result.

3.3 Frequency Domain Interference Cancellation

3.3.1 Analog Case

In order to better understand how to implement an interference cancellation FDAF, it is useful to first review the non-adaptive analog case². Figure 3.2 shows the block diagram for a theoretical interference cancellation filter in an astronomical application, where all signals are considered analog. In this case, the inputs of the filter take the following roles:

- The desired signal becomes the primary signal, which combines the astronomical signal of interest $a(t)$ and the interference measurement $i(t)$: $a(t) + i(t)$.

²For this work, analog signals refer to non-digitized signals, that is, signal with domain and codomain in the real numbers \mathbb{R} .

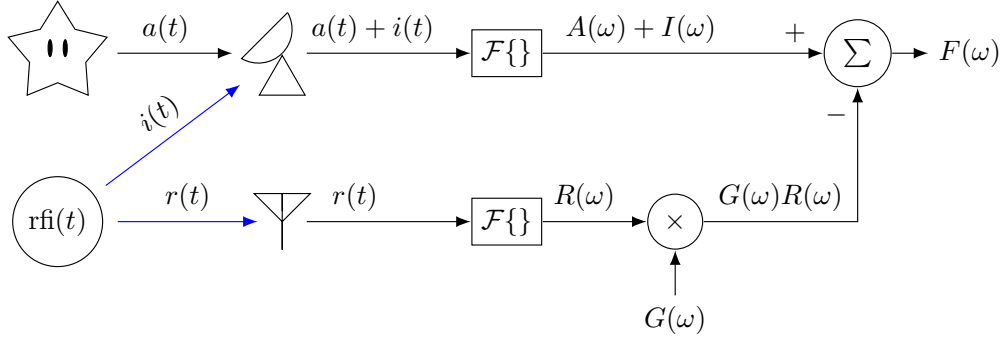


Figure 3.2: Theoretical non-adaptive filter for analog signals. The signal captured by the telescope is the primary signal $a(t) + i(t)$, while the one from the antenna is called reference signal $r(t)$. The filter parameters $G(\omega)$ and the filter output $F(\omega)$ are in the frequency domain. Paths in blue must be Linear Time-Invariant in order for the filter to work.

- The filter reference input becomes the interference measurement by the reference antenna $r(t)$.
- The filter parameters are represented as an analog, frequency domain function $G(\omega)$.

In this case $i(t)$ and $r(t)$ are closely related, as both come from the RFI source $\text{rfi}(t)$. An important condition in order for the filter to work properly is that the paths the RFI take to both the telescope and the reference antenna must be *Linear Time-Invariant* (LTI) systems. If that is the case, then LTI theory states that $i(t)$ and $r(t)$ can be written as:

$$i(t) = \text{rfi}(t) * h_i(t) \quad (3.1)$$

$$r(t) = \text{rfi}(t) * h_r(t). \quad (3.2)$$

Where $*$ is the convolution operator and $h_i(t)$ and $h_r(t)$ are the impulse response of the primary path and the reference path respectively. The equations (3.1) and (3.2) can be transformed to the frequency domain using the *Convolution Theorem* [30]. The Convolution Theorem states that convolution in time is translated to multiplication in the frequency domain,

$$\mathcal{F}\{f * g\} = \mathcal{F}\{f\} \cdot \mathcal{F}\{g\}, \quad (3.3)$$

where \mathcal{F} denotes the Fourier Transform. Therefore, applying the Fourier Transform at both sides in equations (3.1) and (3.2) we obtain

$$I(\omega) = \text{RFI}(\omega) \cdot H_i(\omega) \quad (3.4)$$

$$R(\omega) = \text{RFI}(\omega) \cdot H_r(\omega), \quad (3.5)$$

where ω represents frequency, and the uppercase functions I , R , H_i , H_r and RFI correspond to the Fourier transformed versions of their lowercase counterparts. Then, I and R can be related in the frequency domain by

$$\text{RFI}(\omega) = \frac{I(\omega)}{H_i(\omega)} = \frac{R(\omega)}{H_r(\omega)}. \quad (3.6)$$

This expression is the same as saying that, if the effect of the signals path is reverted, both signals $I(\omega)$ and $R(\omega)$ return to their original form $\text{RFI}(\omega)$.

The relation in (3.6) can be used to get the parameters $G(\omega)$ that provide the desired output of the filter. From Figure 3.2 the output of the filter is given by

$$F(\omega) = A(\omega) + I(\omega) - G(\omega)R(\omega). \quad (3.7)$$

The desired output is to cancel the interference $I(\omega)$ while keeping the astronomical signal intact. Therefore, by imposing $F(\omega) = A(\omega)$, one can solve for $G(\omega)$ to get the optimal parameters of the filter

$$G(\omega) = \frac{I(\omega)}{R(\omega)}. \quad (3.8)$$

The expression (3.8) can be rewritten in terms of the transfer functions of the paths by using the relation (3.6)

$$G(\omega) = \frac{H_i(\omega)}{H_r(\omega)}. \quad (3.9)$$

Equation (3.9) proves that the optimal parameters of the filter do not depend on the input signals $A(\omega), I(\omega), R(\omega)$, but only on the nature of both paths the interference take to the receiver. Since it is required of the signals path to be time-invariant, this filter cannot adapt to changes in the characteristics of the paths.

3.3.2 Analog Sinusoid Case

An important case of study is the one where the inputs are analog sinusoid waves (CW). In this case the input signals can be rewritten as

$$a(t) = Ae^{j\omega_0 t} = |A|e^{j(\omega_0 t + \phi_A)} \quad (3.10)$$

$$i(t) = Ie^{j\omega_0 t} = |I|e^{j(\omega_0 t + \phi_I)} \quad (3.11)$$

$$r(t) = Re^{j\omega_0 t} = |R|e^{j(\omega_0 t + \phi_R)}, \quad (3.12)$$

where $A = |A|e^{j\phi_A}$, $I = |I|e^{j\phi_I}$, $R = |R|e^{j\phi_R} \in \mathbb{C}$ are the signals' phasors that define the CWs amplitude and phase, and ω_0 represents a fixed frequency. As the time domain signals have an unique, constant frequency, their Fourier Transform is given by a single complex value, $A(\omega) = A$, $I(\omega) = I$, $R(\omega) = R$. Similarly, the transfer functions and the filter parameters turn into single phasors,³

$$H_i(\omega) = H_i = |H_i|e^{j\phi_{H_i}}, \quad H_r(\omega) = H_r = |H_r|e^{j\phi_{H_r}}, \quad G(\omega) = G = |G|e^{j\phi_G}. \quad (3.13)$$

Then, relation (3.6) turns into the following:

$$\frac{I}{H_i} = \frac{R}{H_r} \quad (3.14)$$

³Assuming the LTI condition for the signals' path still hold.

$$\Leftrightarrow \frac{|I|}{|H_i|} e^{j(\phi_I - \phi_{H_i})} = \frac{|R|}{|H_r|} e^{j(\phi_R - \phi_{H_r})} \quad (3.15)$$

$$\Leftrightarrow \frac{|I|}{|H_i|} = \frac{|R|}{|H_r|} \quad \text{and} \quad \phi_I - \phi_{H_i} = \phi_R - \phi_{H_r} \quad (3.16)$$

$$\Leftrightarrow \frac{|I|}{|R|} = \frac{|H_i|}{|H_r|} \quad \text{and} \quad \phi_I - \phi_R = \phi_{H_i} - \phi_{H_r}. \quad (3.17)$$

Therefore the amplitude ratio and phase difference of signals $i(t)$ and $r(t)$ can be derived from the amplitude ratio phase difference of the signals' path. Then, starting from equation (3.8), the optimal value for the filter parameter G is given by

$$G = \frac{I}{R} \quad (3.18)$$

$$= \frac{|I|}{|R|} e^{j(\phi_I - \phi_R)} \quad (3.19)$$

$$= \frac{|H_i|}{|H_r|} e^{j(\phi_{H_i} - \phi_{H_r})}. \quad (3.20)$$

Equation (3.19) can be used to compute G if one has full control of signal $a(t)$ and $\text{rfi}(t)$. By setting $a(t) = 0$ and $\text{rfi}(t)$ to a CW, the magnitude ratio and phase difference between both inputs can be computed for every desired frequency ω_0 in an offline manner, and the digital constant G can then be loaded to a digital processing unit to correct for the path imbalances. This scheme is similar to the one used to calibrate the digital back-end of astronomical receivers, as shown in [31] for sideband separating receivers, and in [32] for digital orthomode transducers.

Unfortunately, for RFI mitigation this approach cannot be used, as the sources cannot be controlled by the telescope operator. In this case, the constants G can only be computed for the interference present at the time of calibration. If the interference changes in frequency, the calibration process must be performed again. This become practically impossible for modern, fast changing communication schemes like *Frequency-Hopping Spread Spectrum* (FHSS) and *Direct-sequence spread spectrum* (DSSS). Furthermore, the RFI environment can change rapidly over time, violating the LTI condition. Some of the reasons the LTI assumption no longer holds for the RFI scenario are:

- Telescopes move as they follow astronomical sources, which changes the directions of the sidelobes that measure the interference. As the sidelobes move, the path of the interference to the telescope changes, yielding a different phase and amplitude measurements. Some interferences can effectively disappear from the sidelobe field of vision, while new RFI can emerge.
- The RFI sources can also be moving, which effectively changes the path the signal takes to both the telescope and the reference antenna. Non-geostationary satellites are an example of high elevation moving RFI sources.
- The environment itself can change. The propagation medium is affected by changes in temperature and pressure. Some air molecules can produce absorption, refraction, and scattering effects at certain frequencies. Large moving objects, like vehicles or construction machines, can produce reflections over the signals.

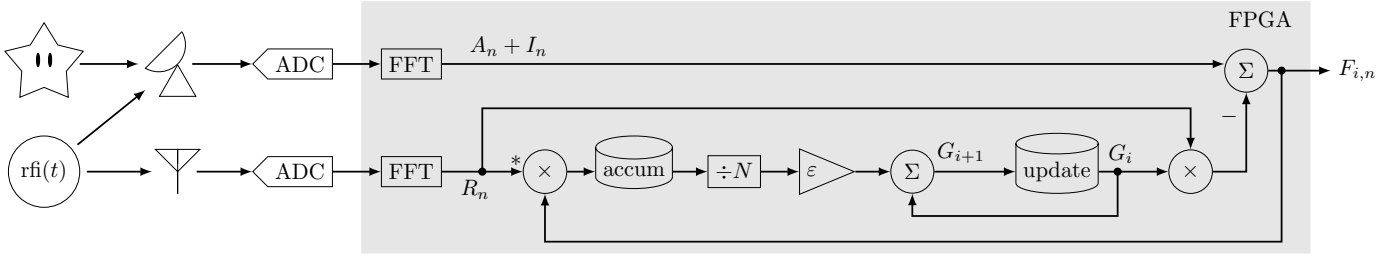


Figure 3.3: Diagram of the implemented FDAF. Lines after the FFT blocks represent a single bin of the Discrete Fourier Transform. In a real implementation every bin of the DFT is processed independently.

Adaptive filters are able to react to changes in the interference and the environment. Hence, they are more effective for the RFI problem. Next section presents a digital implementation of an FDAF for RFI mitigation.

3.4 Frequency-Domain Adaptive Filter Implementation

In an FDAF, the filter parameters are constantly tuned through the adaptive algorithm. Therefore, it is only required that the LTI condition holds for the small period of time the filter is converging. If the RFI environment changes slow enough, the filter can adapt in time to accommodate its parameters to the current state of the environment.

Figure 3.3 shows a schematic diagram of the FDAF implemented for this work. The design is based in the one presented in [24]. The same nomenclature of the previous sections is used for the FDAF. The next two sections explain the filter stages and the mathematical derivation of the adaptive algorithm.

3.4.1 Signal Digitization

Since adaptive filters are digital systems, the primary and the reference signals must be digitized by *Analog-Digital Converters* (ADC). It is assumed that the telescope and antenna back-ends properly amplify and down-convert the analog signals in order for the ADC to sample them correctly. The implications of the signal digitization over the filter performance are various and are studied in Chapter 4.

After the ADCs, the digital spectrum of the signals is computed using Fast Fourier Transform blocks. In a discrete spectrum, the signals bandwidth is divided in a finite number of equally spaced frequency bins. The FFT block computes a complex value for each frequency bin that represents the spectral content of the bin in amplitude and phase.

For a non-adaptive case, a scheme similar to the one described for the CW case (Section 3.3.2) can be used, where a complex weight, given by equation (3.19), is computed and applied to each frequency bin, effectively removing the interference in the whole bandwidth.

The implementation of the adaptive algorithm provides the mechanism to update the weight over time for changes in the RFI environment.

3.4.2 Cross-Correlation Computation

As stated in Section 3.1, the most common adaptive algorithm uses the cross-correlation as a measure of similarity between two signals, which then is used to compute the error signal intended to be minimized. The mathematical expression for cross-correlation is

$$(f \star g)(\tau) := \int_{-\infty}^{\infty} f(t)g(t + \tau)dt, \quad (3.21)$$

where \star is the cross-correlation operator. Similarly to the Convolution Theorem, there exists the *Correlation Theorem* [30], which provides a simple expression for the cross-correlation in the frequency domain,

$$\mathcal{F}\{f \star g\} = \mathcal{F}\{f\}^* \cdot \mathcal{F}\{g\}, \quad (3.22)$$

where $*$ denotes complex conjugation. This property, combined with the FFT algorithm, is exploited in FDAFs for efficient computation of cross-correlation. For the discrete case, the cross-correlation has a simple interpretation. Considering two complex values F and G , generated from a single bin of two FFT, their cross-correlation is given by

$$F \star G = F^* \cdot G = |F|e^{-j\phi_F} \cdot |G|e^{j\phi_G} = |G||F|e^{j(\phi_G - \phi_F)}. \quad (3.23)$$

That is, the discrete frequency domain cross-correlation is given by the bin-wise complex multiplication of the spectra, equal to their amplitude multiplication and phase difference. This type of computation is the same used in FX correlators implemented for interferometric arrays in radio astronomy [33]. In the FDAF algorithm, the cross-correlation between the reference signal and the filter output is computed (represented by the conjugated multiplication after the FFT, in the reference signal in Figure 3.3), which is then used to minimize the power of the filter output.

3.4.3 Adaptive Algorithm

The adaptive algorithm of the FDAF implemented can be thought as a set of discrete difference equations derived from the Figure 3.3. The FFT blocks are considered pipeline FFTs that continuously computes new spectra as the data arrives. The subindex $n \in \mathbb{N}$ of the signals indicate the discrete time index of the spectrum computed. For the mathematical derivation, a single frequency bin of the FFTs output is analyzed, represented by the phasors $A_n + I_n$ for the primary signal and R_n for the reference signal.

The implemented adaptive filter presents two type of cycles: accumulation cycles and update cycles. In the accumulation cycles the cross-correlation between the reference signal R_n and the filter output $F_{i,n}$ is computed, and the result is accumulated. Every new cycle a new cross-spectrum is added to the accumulation. The number of accumulations performed is given by the user-defined parameter N , after which the accumulation value is reset. It is

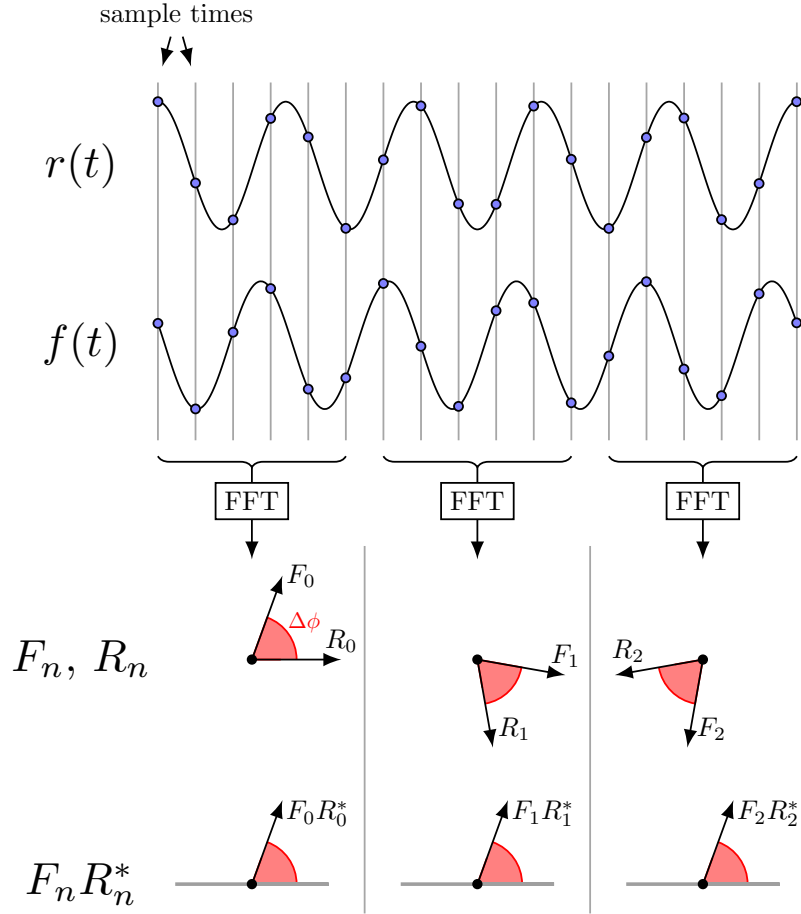


Figure 3.4: Illustration of the phasors of two CW and their cross-spectrum. It can be seen that the 6-points FFTs are computed in arbitrary segments of the CWs so the resulting phasors seem to have random phases. However, the phase difference is preserved, then the cross-spectrum produces a phasor with constant phase that can be accumulated in a digital system.

important to notice that for the digital case, the complex phasors of the input signals cannot be accumulated, even when they are produced by CW signals. That is because Discrete Fourier Transform blocks compute the spectrum from an arbitrary slice of the signal, which in general produces a phasor with a random phase. However, it is valid to accumulate the cross-spectrum of two CW with constant phase difference $\Delta\phi$, as the resulting phasor will have constant phase equal to $\Delta\phi$. This property is illustrated in Figure 3.4. Therefore, the accumulation cycle can be thought as the accumulation of a phasor with phase equal to the phase difference between the filter output and the reference signal.

After N accumulation cycles have passed a new update cycle starts. In an update cycle the accumulated cross-spectrum is scaled by N (to remove the increase of amplitude produced by the accumulation), and multiplied by the filter gain ε . The resulted value is used to update the filter parameter G_i . The subindex $i \in \mathbb{N}$ indicates the number of the update cycle. The relation between the subindices n and i is shown in Table 3.1. The gain ε is an user-defined parameter that controls the convergence speed of the filter. The updated parameter G_i is then used to remove the interference of the primary signal and produce the filter output $F_{i,n}$.

new spectra/ accumulation cycle (n)	0	1	2	...	$N-1$	N	$N+1$...	$2N-1$	$2N$...	
update cycle (i)	0						1					

Table 3.1: Relation between accumulation cycle index n and update cycle index i . After N accumulation cycles a new accumulation starts and the filter parameters are updated.

3.4.4 Mathematical Derivation of the Adaptive Algorithm

The discrete equations of difference that describe the adaptive filter, as derived from the diagram in Figure 3.3, are

$$G_0 = 0 \quad (3.24)$$

$$G_{i+1} = \varepsilon \frac{1}{N} \sum_{j=Ni}^{N(i+1)-1} F_{i,j} R_j^* + G_i \quad (3.25)$$

$$F_{i,n} = A_n + I_n - G_i R_n, \quad (3.26)$$

where (3.24) states the initial values of the filter parameters, (3.25) is the equation for the update of the filter parameters, and (3.26) is the filter output equation. To solve this system of equations one should replace (3.26) in (3.25)

$$G_{i+1} = \varepsilon \frac{1}{N} \sum_{j=Ni}^{N(i+1)-1} (A_j + I_j - G_i R_j) R_j^* + G_i \quad (3.27)$$

$$= \varepsilon \frac{1}{N} \sum_{j=Ni}^{N(i+1)-1} A_j R_j^* + I_j R_j^* - G_i R_j R_j^* + G_i \quad (3.28)$$

$$= \varepsilon \frac{1}{N} \underbrace{\sum_{j=Ni}^{N(i+1)-1} A_j R_j^*}_{:=C_i} + \varepsilon \frac{1}{N} \sum_{j=Ni}^{N(i+1)-1} \underbrace{I_j R_j^*}_{:=K} - \varepsilon \frac{1}{N} G_i \sum_{j=Ni}^{N(i+1)-1} \underbrace{R_j R_j^*}_{:=r^2} + G_i \quad (3.29)$$

$$= \varepsilon \frac{1}{N} C_i + \varepsilon \frac{1}{N} \sum_{j=Ni}^{N(i+1)-1} K - \varepsilon \frac{1}{N} G_i \sum_{j=Ni}^{N(i+1)-1} r^2 + G_i \quad (3.30)$$

$$= G_i - \varepsilon r^2 G_i + \frac{\varepsilon}{N} C_i + \varepsilon K \quad (3.31)$$

$$= \underbrace{(1 - \varepsilon r^2)}_{:=b} G_i + \frac{\varepsilon}{N} C_i + \varepsilon K \quad (3.32)$$

$$G_{i+1} = b G_i + \frac{\varepsilon}{N} C_i + \varepsilon K. \quad (3.33)$$

In these equations the following definitions were made $r^2 := |R_j|^2 = R_j R_j^*$, $b := 1 - \varepsilon r^2$, and $C_i = \sum_{j=Ni}^{N(i+1)-1} A_j R_j^*$. These definitions require the assumption that the input does not significantly change in frequency or power during the accumulation cycle. Additionally, assuming that the LTI condition holds during this same cycle, the constant phasor K can be

defined as correlation between the two interference signals $K := I_j R_j^*$. The equation (3.33) is a first order difference equation which solution is given by

$$G_i = \frac{\varepsilon}{N} \sum_{k=0}^{i-1} b^k C_{i-k-1} + \frac{K}{r^2} (1 - b^i). \quad (3.34)$$

Choosing $\varepsilon \in (-1/r^2, 1/r^2)$, so that $|b| < 1$, ensures that the algorithm converges. Replacing expression (3.34) for G_i in (3.26)

$$F_{i,n} = A_n + I_n - R_n \left(\frac{\varepsilon}{N} \sum_{k=0}^{i-1} b^k C_{i-k-1} + \frac{K}{r^2} (1 - b^i) \right) \quad (3.35)$$

$$= A_n + I_n - R_n \frac{K}{r^2} (1 - b^i) - \frac{\varepsilon}{N} R_n \sum_{k=0}^{i-1} b^k C_{i-k-1} \quad (3.36)$$

$$= A_n + I_n - \frac{R_n R_n^*}{r^2} (1 - b^i) I_n - \frac{\varepsilon}{N} R_n \sum_{k=0}^{i-1} b^k C_{i-k-1} \quad (3.37)$$

$$= A_n + b^i I_n - \underbrace{\frac{\varepsilon}{N} R_n \sum_{k=0}^{i-1} b^k C_{i-k-1}}_{:=D_i} \quad (3.38)$$

$$F_{i,n} = A_n + b^i I_n - D_i. \quad (3.39)$$

Therefore, as long as $|b| < 1$, the interference from the telescope I_n gets canceled out for $i \rightarrow \infty$. The ideal case is when $\varepsilon = 1/r^2$, then $b = 0$ and the filters converges in a single accumulation cycle (as long as r^2 remains constant).

The last term D_i in (3.39) represents the added noise of the filter. Its complex structure makes it difficult to analyze it mathematically. Intuitively, the magnitude of D_i can be reduced by either decreasing the value of ε or increasing the accumulation number N . In the extreme case where fastest convergence speed is required, the filter parameters must be set to $\varepsilon = 1/r^2$ and $N = 1$, in which case the filter noise is also maximized. For this parameter selection, the filter noise is given by

$$D_i = \varepsilon R_i C_{i-1} \quad (3.40)$$

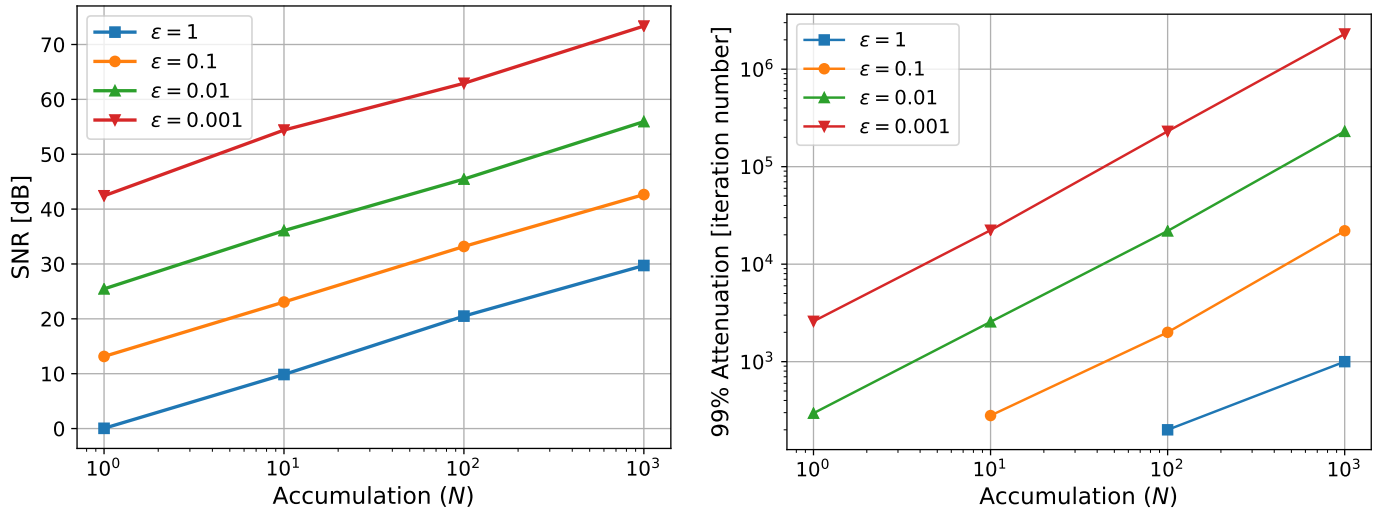
$$= \frac{R_i R_{i-1}^*}{r^2} A_{i-1}. \quad (3.41)$$

So the noise magnitude is

$$|D_i| = \frac{|R_i| |R_{i-1}^*|}{r^2} |A_{i-1}| \quad (3.42)$$

$$= |A_{i-1}|. \quad (3.43)$$

Therefore, for the parameter combination of fastest convergence, the filter noise has the same magnitude as the astronomical signal, which can or cannot be acceptable depending on the



(a) Simulated SNR test for the RFI filter, for different parameter choices. The interference power is normalized at $r^2 = 1$. Varying the astronomical signal power does not significantly change the results.

(b) Simulated convergence test for the RFI filter, for different parameter choices. The interference and astronomical signals power are normalized to 1. Reducing the astronomical signal power does not significantly change the results. Some parameters combinations are not show as the filter noise prohibits 99% attenuation.

Figure 3.5: RFI filter simulated tests.

application. The term *Signal-to-Noise ratio* (SNR) is defined as the ratio between a signal power and the power of the noise affecting the signal. For the filter case, the SNR is given by $|A_n|^2/|D_i|^2 = 0$ dB. If lower SNR is required, the user should modify the ϵ and N parameters.

In order to have more quantitative information of the effects of the filter parameters, computer simulations were performed to calculate the SNR of the filter for different combinations of ϵ and N . The analysis is done for a single frequency bin, and the signals are assumed to have random phases. The results are shown in Figure 3.5a.

The previous analysis does not take in account the convergence speed of the filter, so a second round of simulations is performed where the convergence time is computed as the number of iterations required to reduce an artificial interference signal to 1% of its original power (99% of attenuation). The results are shown in Figure 3.5b. Combining the information of both figures, the filter user should be able to choose a set of parameters that satisfy the requirements of SNR and speed. Although this analysis was done for a single frequency bin, it can be extended to all the bins of the FFT output, as the filter is applied to every bin independently.

3.5 Summary

In this chapter, the mathematical description of a digital frequency-domain adaptive filter is presented. It is proven that the filter is able to remove interference from an astronomical

signal of arbitrary bandwidth. The filter parameters ε and N provide a trade-off between the convergence speed, the convergence stability, and added noise. The combination of parameters that provide the best performance are dependent of the RFI situation of the telescope, and it should be determined on-site. The required assumptions for the filter to work are that the input signals remain relatively constant in frequency and power, and the RFI environment satisfies the LTI condition. Both of these assumptions must hold for at least the time the filter takes to converge.

Chapter 4

Adaptive Filter Limitations

In this chapter, the effects of digitization, noise, and other implementation phenomena are studied, with an emphasis on their impact on the filter performance.

4.1 Digitization Effects

4.1.1 Time Quantization

All Analog-Digital Converters run at a *sampling frequency* F_s that determines the number of samples per second it digitizes from the analog signal. A finite sampling frequency imposes a theoretical limitation on digital systems, stated in the *Nyquist Sampling Theorem*: in order to sample an analog signal without loss of information, the sampling frequency must be greater than twice the signal bandwidth [34]. Mathematically, to sample a signal with bandwidth BW the ADC must satisfy

$$F_s > 2BW. \quad (4.1)$$

Then, the adaptive filter processing bandwidth is given by half the sampling frequency its ADCs are working at.

Time discretization comes with an additional undesired effect known as *Aliasing*. The aliasing phenomenon distorts the sampled signal by wrapping around frequency components above the maximum baseband frequency into the system operating bandwidth, as shown in Figure 4.1. This produces an ambiguity in the measured data, where baseband signals are mixed up with out-of-band signals in the frequency spectrum. The aliasing effect is particularly harmful for the RFI filter because it can combine multiple RFI signals of different frequencies into a single spectral band. As explained in Section 4.3, the filter performance greatly degrades when multiple uncorrelated RFI sources are measured in the same FFT bin. The best way to avoid aliasing is to use bandpass filters in the analog front-end of the receiver to cancel any out-of-band signal before they enter the ADC.

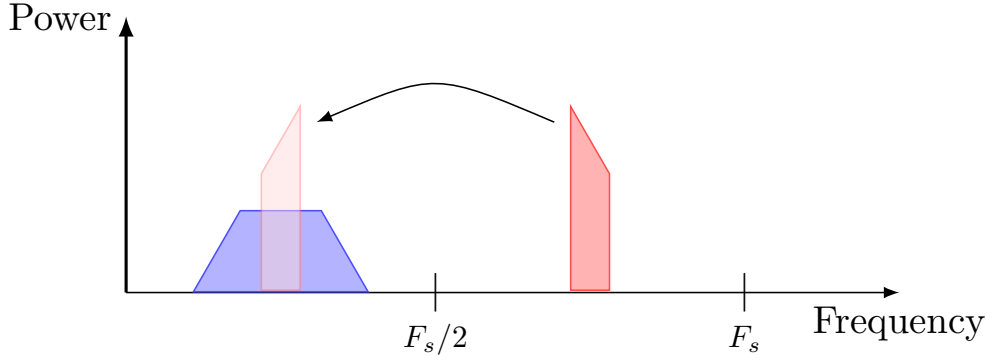


Figure 4.1: Visual demonstration of the aliasing effect. The frequency component in red gets wrapped around since it is above $F_s/2$, and overlaps with the blue frequency component. Overlapping RFI signals damage the filter performance, as explained in Section 4.3.

4.1.2 Amplitude Quantization

In addition to time quantization, ADCs digitize the voltage or amplitude of its input signal, meaning that the exact analog value of the signal at the sampled time gets approximated by the closest digital ADC output. This effect produces distortions in the measured signal in the form of added noise, known as *quantization noise*. The most common formula to approximate the quantization noise effects from an ideal N bits ADC is given by [35]

$$\text{SNR} = 6.02N + 1.76 \text{ dB}, \quad (4.2)$$

where SNR is the signal-to-noise ratio between a sinewave signal using the full range of the ADC, and the quantization noise. The last equation corresponds to the noise across the whole bandwidth of the ADC. If instead, the SNR on a single frequency bin of a spectrometer is needed (also known as dynamic range), the equation changes slightly,

$$\text{SNR} = 6.02N + 1.76 + 10 \log_{10} \left(\frac{\text{FFT_Size}}{2} \right) \text{ dB}, \quad (4.3)$$

where FFT_Size is the number of samples used to compute the FFT of the spectrometer. In reality, the ADC noise is also affected by non-linearities of its electronic components. To have a more realistic account of the ADC noise, empiric quality measures, like the *Signal-to-Noise-and-Distortion Ratio* (SINAD), and *Effective Number of Bits* (ENOB), can be taken.

The maximum attenuation level achievable by the adaptive filter is given by the signal-to-noise ratio of the used ADC. Below that level the canceled signal would get buried into the quantization noise. This fact imposes a theoretical limitation on the use of the filter. The power difference between the interference signal and the signal of interest cannot be greater than the ADC's SNR. If the interference power is too high, an ADC with a larger number of bits may be needed. In practice, the attenuation level is usually first limited by the effect of phase noise produced by external signals, as explained in Section 4.2.

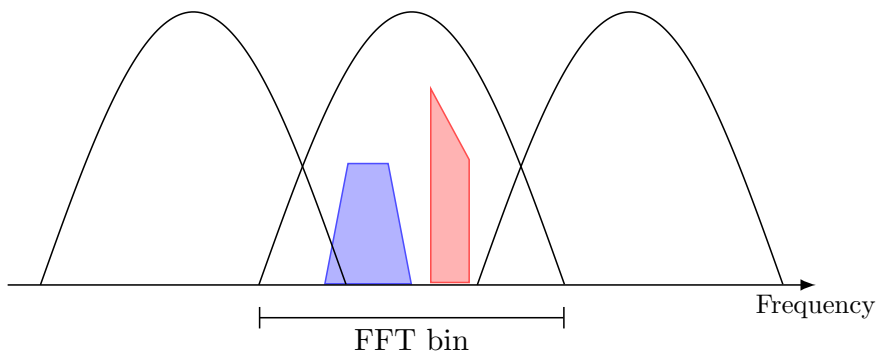


Figure 4.2: Black lines represent FFT frequency bins. The blue and red frequency components landed in the same bin. The output of that bin combines the information of both signal, making them indistinguishable.

4.1.3 Frequency Quantization

The frequency resolution of a spectrometer is defined as the bandwidth of each individual bin of its FFT. It can be computed as

$$BW_{bin} = \frac{BW}{\text{FFT_Size}/2} = \frac{F_s}{\text{FFT_Size}}, \quad (4.4)$$

where BW and BW_{bin} are the bandwidth of the whole spectrum and a single bin respectively. Reducing the value of BW_{bin} provides a clearer image of the frequency components of the spectrum. To improve the frequency resolution one can either reduce the operating bandwidth, which can be restricted by the ADC allowed frequency rates, or increase the FFT_Size , which increases the required computational resources.

For the adaptive filter, the frequency resolution should be enough so that two independent interferences do not overlap in the same frequency bin, as shown in Figure 4.2. This scenario is equivalent to having two overlapping RFI sources in the same bin, which is known to degrade the filter performance (see Section 4.3). The exact resolution required depends on the characteristics of the astronomical signal and the RFI involved in the observation.

4.2 Effect of Noise

External noise is one of the primary factors that affect the filter performance. To mathematically analyze the effect of noise, three noisy versions of the filter inputs are defined as

$$\tilde{A}_n = A_n + W_{A,n} \quad (4.5)$$

$$\tilde{I}_n = I_n + W_{I,n} \quad (4.6)$$

$$\tilde{R}_n = R_n + W_{R,n}, \quad (4.7)$$

where the signals $W_{A,n}$, $W_{I,n}$, and $W_{R,n}$ represent constant-power noise added to the inputs. Then, doing a similar analysis to the one in Section 3.4.3, one can arrive to an equation for

G_i equivalent to (3.29):

$$G_{i+1} = \underbrace{\varepsilon \frac{1}{N} \sum_{j=Ni}^{N(i+1)-1} \tilde{A}_j \tilde{R}_j^*}_{(a)} + \underbrace{\varepsilon \frac{1}{N} \sum_{j=Ni}^{N(i+1)-1} \tilde{I}_j \tilde{R}_j^*}_{(b)} - \varepsilon G_i \underbrace{\frac{1}{N} \sum_{j=Ni}^{N(i+1)-1} \tilde{R}_j \tilde{R}_j^*}_{(c)} + G_i. \quad (4.8)$$

To simplify the analysis, it is assumed that the accumulation number N is large enough that any accumulation product of uncorrelated signals becomes negligible. With this assumption in mind, the different terms of equation (8.3) become: (a) = 0, (b) = K , and (c) = \tilde{r}^2 , where $\tilde{r}^2 = r^2 + w^2$, and $w^2 = |W_{R,n}|^2$. Then it follows that

$$G_{i+1} = \varepsilon K - \varepsilon \tilde{r}^2 G_i + G_i \quad (4.9)$$

$$= \underbrace{(1 - \varepsilon \tilde{r}^2)}_{:=\tilde{b}} G_i + \varepsilon K \quad (4.10)$$

$$G_{i+1} = \tilde{b} G_i + \varepsilon K. \quad (4.11)$$

Therefore, the only noise component that affects the filter parameters is the noise from the reference signal $W_{R,n}$. Solving the difference equation from (4.11) yields

$$G_i = \frac{K}{\tilde{r}^2} (1 - \tilde{b}^i). \quad (4.12)$$

Replacing this value into the equation for the filter output (3.26) (using the appropriate noisy inputs) gives the expression for the filter output

$$F_{i,n} = \tilde{A}_n + \tilde{I}_n - G_i \tilde{R}_n \quad (4.13)$$

$$= A_n + W_{A,n} + I_n + W_{I,n} - \frac{K}{\tilde{r}^2} (1 - \tilde{b}^i) (R_n + W_{R,n}) \quad (4.14)$$

$$= A_n + W_{A,n} + I_n + W_{I,n} - \frac{K}{\tilde{r}^2} (R_n + W_{R,n}) + \tilde{b}^i \frac{K}{\tilde{r}^2} (R_n + W_{R,n}). \quad (4.15)$$

For the sake of simplification, it is assumed that the filter has already converged, that is, $\tilde{b}^i \xrightarrow{i \rightarrow \infty} 0$. Then,

$$F_{i,n} = A_n + W_{A,n} + I_n + W_{I,n} - \frac{K}{\tilde{r}^2} (R_n + W_{R,n}) \quad (4.16)$$

$$= A_n + W_{A,n} + I_n + W_{I,n} - \frac{K R_n}{\tilde{r}^2} - \frac{K W_{R,n}}{\tilde{r}^2} \quad (4.17)$$

$$= A_n + W_{A,n} + W_{I,n} + I_n - \frac{r^2}{\tilde{r}^2} I_n - \frac{R_n W_{R,n}}{\tilde{r}^2} I_n \quad (4.18)$$

$$= A_n + W_{A,n} + W_{I,n} + \underbrace{\left(1 - \frac{r^2}{\tilde{r}^2} - \frac{R_n W_{R,n}}{\tilde{r}^2}\right)}_{:=E_n} I_n. \quad (4.19)$$

The middle terms $W_{A,n}$ and $W_{I,n}$ represent the expected noise entering through the primary channel. The last term E_n is residual interference uncanceled by the filter due to the

reference channel noise. The impact of E_n in the performance of the filter can be understood by computing the magnitude $|E_n|$,

$$|E_n| = \left| 1 - \frac{r^2}{\tilde{r}^2} - \frac{R_n W_{R,n}}{\tilde{r}^2} \right| |I_n| \quad (4.20)$$

$$\leq \left(\left| 1 - \frac{r^2}{\tilde{r}^2} \right| + \left| \frac{R_n W_{R,n}}{\tilde{r}^2} \right| \right) |I_n| \quad (4.21)$$

$$= \left(\frac{\tilde{r}^2 - r^2}{\tilde{r}^2} + \frac{rw}{\tilde{r}^2} \right) |I_n| \quad (4.22)$$

$$= \frac{r^2 + w^2 - r^2 + rw}{r^2 + w^2} |I_n| \quad (4.23)$$

$$= \frac{rw + w^2}{r^2 + w^2} |I_n| \quad (4.24)$$

$$\Rightarrow |E_n| \leq \frac{\frac{r}{w} + 1}{\left(\frac{r}{w}\right)^2 + 1} |I_n|. \quad (4.25)$$

To obtain (4.21) the triangular inequality was used¹. The inequality in (4.25) provides a worst case scenario for the magnitude of the residual interference. The ratio $\text{INR} := r/w$ is the *Interference-to-Noise ratio* of the filter. Intuitively, when $\text{INR} \in [0, 1]$ then $|E_n| \geq |I_n|$, so the filter is not properly mitigating the interference. Otherwise if $\text{INR} \gg 1$ then $|E_n| \approx 1/(r/w)|I_n|$, that is, the interference is reduced by a factor of $1/\text{INR}$. As a rule of thumb, the amount of attenuation expected in a noisy environment should be around the same as the INR value, where $\text{INR} = 0$ dB means no attenuation at all. This property is illustrated in Figure 4.3.

4.3 Multiple RFI Sources

Another scenario that can significantly harm the filter performance is when multiple RFI sources are present. If multiple interference signals are measured by the system, one should distinguish between two cases, either if the interferences are located in the same, or different frequency bands. If the RFI signals are sufficiently separated in the frequency spectrum, then the filter does not incur in any penalty, as the algorithm treats every frequency bin independently. However, if the RFI signals share a portion of their frequency band or are close enough that they get measured by the same frequency bin, then, major performance degradation should be expected.

To illustrate the problem consider the scenario of Figure 4.4, where two independent RFI sources are measured by the telescope and reference antenna. Signals generated by the same source are correlated, while signals from different sources present no correlation. The combined interference entering the telescope and the antenna are defined as

$$I_n = I_{1,n} + I_{2,n} \quad (4.26)$$

$$R_n = R_{1,n} + R_{2,n}. \quad (4.27)$$

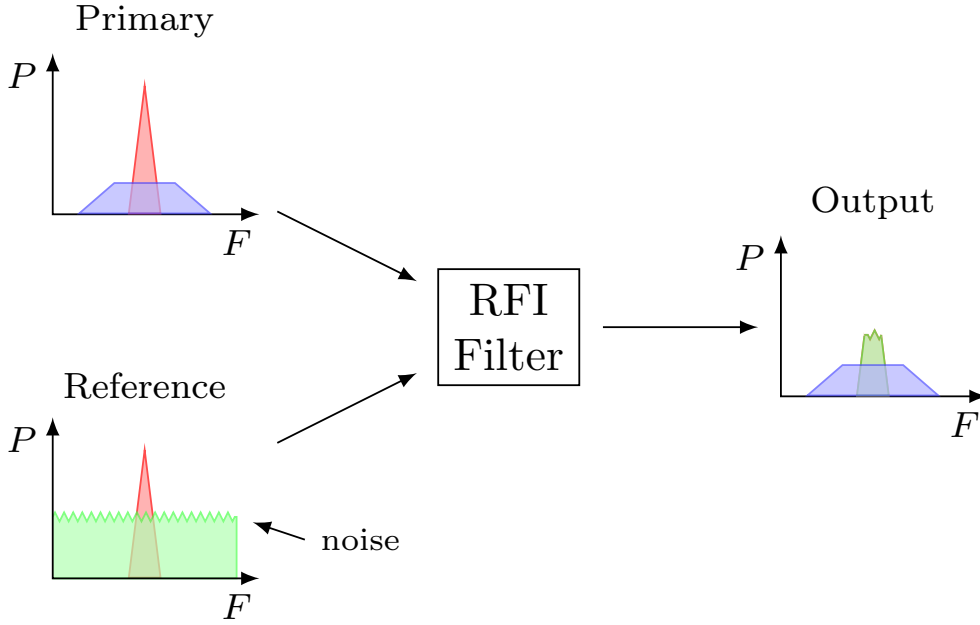


Figure 4.3: Illustration of the filter behavior under high noise conditions. The F and P axes represent frequency and power respectively. Blue curves represent the astronomical signal, red is interference, and green is noise. The interference is not totally cancelled at the filter output due to the low INR at the reference input.

As presented in Section 8.1 of the Appendix, the analysis of two uncorrelated RFI sources is analogous to the noise analysis from section 4.2, for which the filter output is given by

$$F_{i,n} = A_n + \underbrace{\left(1 + \frac{r_1^2}{r_1^2 + r_2^2} - \frac{R_{1,n}^* R_{2,n}}{r_1^2 + r_2^2}\right)}_{:=J_{1,n}} I_{1,n} + \underbrace{\left(1 + \frac{r_2^2}{r_1^2 + r_2^2} - \frac{R_{1,n} R_{2,n}^*}{r_1^2 + r_2^2}\right)}_{:=J_{2,n}} I_{2,n}, \quad (4.28)$$

where $r_1^2 := |R_{1,n}|^2 = R_{1,n} R_{1,n}^*$, and $r_2^2 := |R_{2,n}|^2 = R_{2,n} R_{2,n}^*$. The terms $J_{1,n}$ and $J_{2,n}$ are the uncanceled interference due to the presence of multiple RFI sources. Similar to the noise case, the magnitude of $J_{1,n}$ and $J_{2,n}$ can be upper limited as

$$|J_{1,n}| \leq \frac{\frac{r_1}{r_2} + 1}{\left(\frac{r_1}{r_2}\right)^2 + 1} |I_{n,1}| \quad (4.29)$$

$$|J_{2,n}| \leq \frac{\frac{r_2}{r_1} + 1}{\left(\frac{r_2}{r_1}\right)^2 + 1} |I_{n,2}|. \quad (4.30)$$

In this case the ratios r_1/r_2 and r_2/r_1 act as the INR for the terms $|J_{1,n}|$ and $|J_{2,n}|$ respectively. Therefore, when two interference signals are found in the same frequency bin, only the interference with the higher power is mitigated, and only to the point where the two interferences have the same power level. After that, the INR becomes 0 dB and no more attenuation is possible. This situation is portrayed in Figure 4.5. The two RFI case can

¹The triangular inequality states that: $|a + b| \leq |a| + |b|$, for $a, b \in \mathbb{C}$.

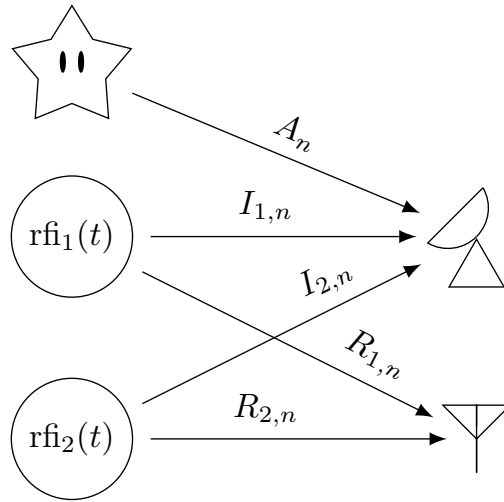


Figure 4.4: Two RFI sources scenario.

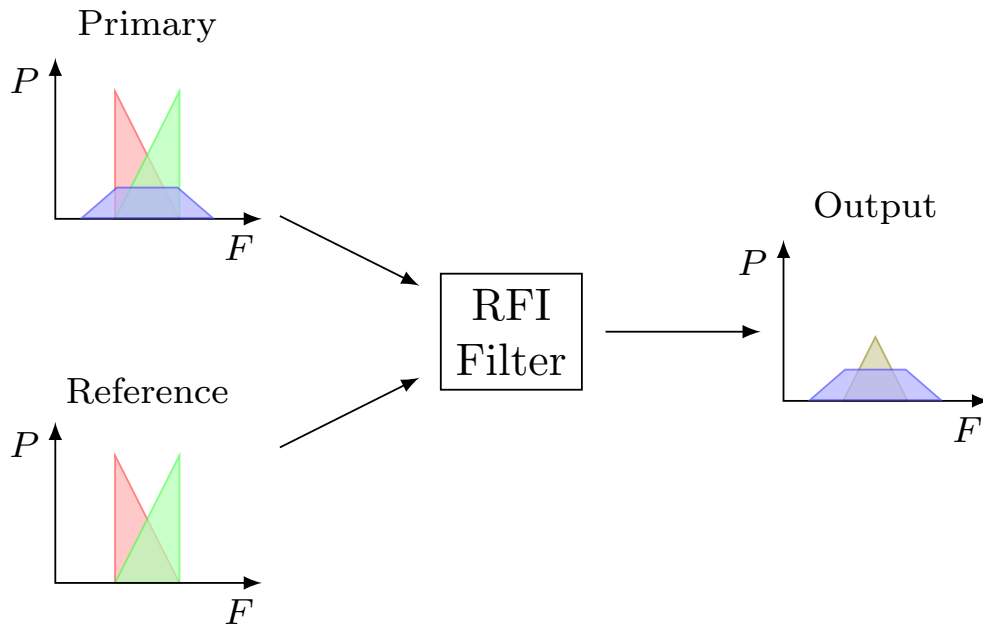


Figure 4.5: Illustration of the filter behavior for multiple RFI sources. The F and P axes represent frequency and power respectively. Blue curves represent the astronomical signal, red and green are interference. High power interference is only canceled to the level of the lower interference.

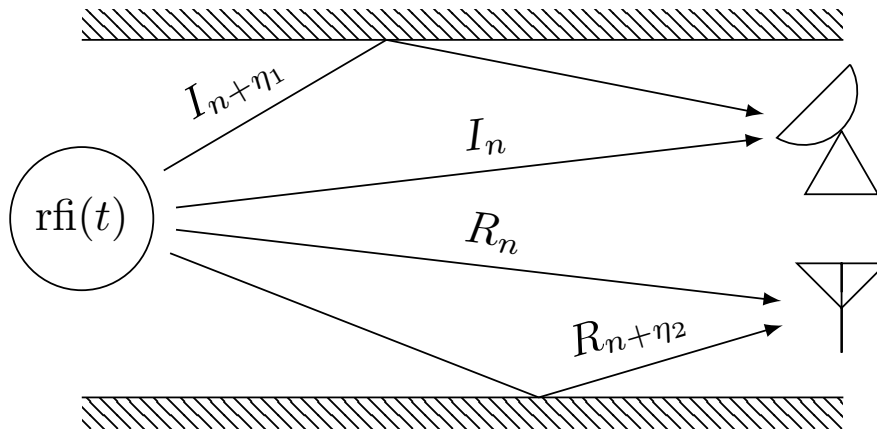


Figure 4.6: Illustration of the multipath problem for an RFI mitigation setup. The values η_1 and η_2 represent the delay with respect the line of sight of the copies created by the multipath effect.

be extended to more sources, where only the one with the higher power is mitigated, until it reaches the added power of the rest of the sources. The multiple RFI scenario can be particularly harmful for the filter, due to the great amount of RFI signals present in most locations, and their high power compared to astronomical signals.

4.4 Effect of Multipath Propagation

Multipath propagation is the phenomenon of measuring multiple copies of the same signal, due to the different path that the signal may have taken to reach the receiving antenna. It is most commonly produced by reflections on large terrestrial objects (mountains, buildings), large water bodies (lakes, lagoons), and ionospheric reflections.

Figure 4.6 depicts an RFI mitigation scenario with multipath propagation is affecting the interference signals. Multipath can be very harmful for the RFI filter because the multiple copies that arrive at the telescope and the reference antenna are delayed by different amounts of time. If the delays are large enough, then the added signals can be seen as completely uncorrelated by the receivers. In this case, the multipath situation becomes equivalent to the multiple RFI problem of the previous section.

The exact delay difference for which the multipath signals become uncorrelated depends on two factors, the nature of the interference signal, and the spectrometer characteristics. For the simplest case of the interference being a CW, multipath propagation does not affect the filter performance, independently of the delay difference. That is because delayed versions of an infinite long CWs are always completely correlated. Adding multiple copies of the same CW with different delays just change the phase of the resulting signal, as measured by the spectrometer. On the other hand, the most harmful case of multipath propagation is the interference that has a noise-like behavior, that is, every sample of the signal is uncorrelated from the previous sample. In this case, the different copies of the signals would only be partially correlated, where the level of correlation depends on the number of shared samples

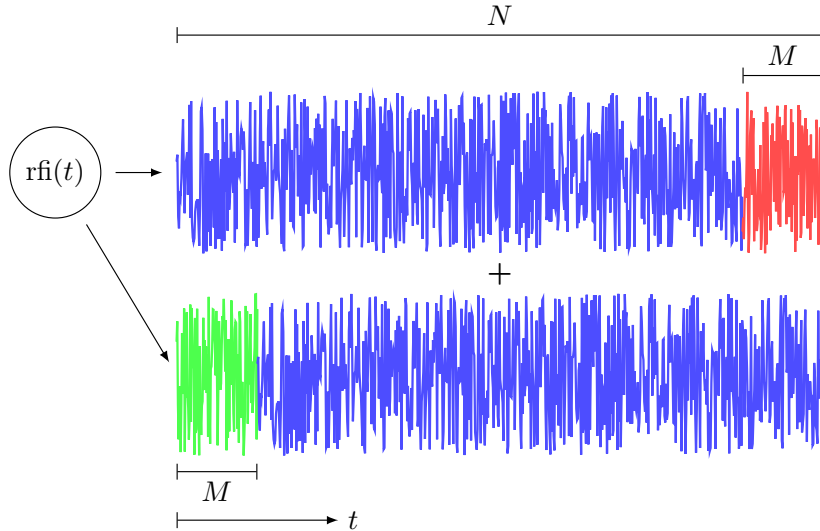


Figure 4.7: Example of two copies of constant power, noise-like signals produced by multipath. The bottom signal is delayed in M samples with respect to the top signal. The resulting signal entering the receiver is the addition of these two signals. If two slices of N samples are extracted from the signals, only the shared samples (plotted in blue) present correlation, and the SNR of the resulting signal is computed as $SNR = (N - M)/M$.

by the copies at the input of the spectrometer's FFT blocks. The unshared samples become noise to the computed spectrum. As an example, consider two copies of a constant power noise signal, where one copy is delayed by M samples. The two copies are added and enter a spectrometer of FFT size N , this is illustrated in Figure 4.7. The signal-to-noise ratio is computed as the ratio between the shared samples and the unshared samples, that is, $SNR = (N - M)/M$. For an FFT size of 8192, the SNR is reduced to 30 dB (assuming no other external noise contributions) with a delay of only 8 samples. For a sampling frequency of 1 GSPS², it is equivalent to having a multipath propagation delay of 8 ns, or a propagation distance difference of 2.4 m.

A general expression for the effect of multipath propagation over the filter is difficult to achieve, due to the wide variety of existing RFI signals. However, it can be assumed that the amount of degradation will be in the range of the two extreme cases of CWs and noise RFI. If the telescope is located in a place that increases the existence of multipath (like places with many buildings or mountains), then the damage is dominated by the path with the longest propagation delay. From the point of view of the telescope operator, the best action against multipath propagation is to locate the telescope and the reference antenna as close as possible to reduce the propagation distance differences, and to increase the spectrometer frequency resolution, either by increasing the FFT size, or reducing the system bandwidth.

²GSPS: giga-samples per second.

4.5 Violation of LTI Condition

For the mathematical derivation of the filter presented in Section 3.4.4, it was assumed that the interference propagation path satisfy the linear time-invariant condition for at least the time the filter is converging. If the LTI condition is not met, it means that somewhere the RFI path is presenting non-linear or time-varying propagation characteristics. At first glance, the main suspect for non-LTI conditions is the atmospheric medium where the signals travel from the source to the receivers. However, there is no natural medium that exhibits strong enough non-linearities, or has fast-changing propagation properties, to meaningfully damage the performance the filter, specially considering that the final implementation converges in fractions of a millisecond (see Section 5.3.1 for laboratory test results).

A possible source of time variance is present when the telescope moves while tracking a celestial source. As the sidelobes capturing the RFI move along with the telescope, the path characteristics of the measured interference gradually change over time. Then again, the implemented filter has proven to be fast enough to not significantly be affected by the slow movement of a telescope.

A more significant cause of non-linearities can be found in some analog components in the receivers' front-end, used before signal digitization. The typical receiver components that produces non-linearities are the ones that can get saturated by the input signal, like amplifiers and frequency mixers. When a component get saturated the amplitude of the input signal gets clipped, which has the undesired effect of producing harmonic distortion. This distortion can easily be seen in spectral data as additional corrupting signals located in frequency in multiples of the center frequency of the original input signal. Furthermore, due to the effect of aliasing after digitization, the harmonic signals can always get wrapped around into the baseband, corrupting the astronomical data. In the RFI mitigation context, harmonic distortion of the interference in the primary channel can significantly damage the filter performance, as the additional harmonic signals would not be present in the reference channel, making them impossible to eliminate.

4.6 Summary

The most important limitations of the RFI filter have been studied, where the conditions that damage the filter performance the most are low INR in the reference antenna, multiple RFI sources in the same frequency band, and multipath propagation. When designing the RFI filter, the spectrometer characteristics should be chosen considering both the desired astronomical observation to be made, and the required mitigation level of the filter. The spectrometer parameters to consider are the ADC number of bits, the sampling rate, and the FFT size. Other aspects that affect the filter performance are the distance between the telescope and the reference antenna, and the analog components used in the front-end.

Chapter 5

Hardware Implementation and Results

In this chapter, the hardware implementation of the RFI filter is presented, along with the results for both laboratory tests, and experiments using real interference and receivers. The results are discussed considering the theoretical foundations from the previous chapters.

5.1 Hardware Description

5.1.1 Field-Programmable Gate Arrays

The actual implementation of the RFI filter was done in a field-programmable gate array (FPGA). An FPGA is an integrated circuit containing a large array of relatively small digital *configurable logic blocks* (CLB), also known as logic cells. These logic blocks can be configured to perform basic digital operations, like boolean logic or data storage of a small number of bits. The CLB array is surrounded by routing channels, which are wires where the digital information can flow. The routing channels intersect in elements called switch boxes, which can be programmed to interconnect different channels and create large paths for the digital signals inside the FPGA. Another basic element of the FPGA are the I/O pads, which provide an interface for the signals entering and leaving the FPGA chip. A simple FPGA diagram with all its basic components is shown in Figure 5.1. By configuring the CLBs, switch boxes, and I/O pads of an FPGA, electronic engineers can implement complex circuits for digital signal processing and other applications.

The description of the digital circuit to implement is usually done in a *hardware description language* (HDL), or a graphical schematic software. Both methods are human-readable representations of the desired circuit. Software tools are then used to generate a bitstream file that indicates the exact configuration of the different resources in the FPGA in order to implement the circuit. This file is then passed to an internal Control Processing Unit (CPU) of the FPGA capable of setting each individual resource to its required configuration.

Aside from the more basic elements, modern FPGAs can present more advanced, high

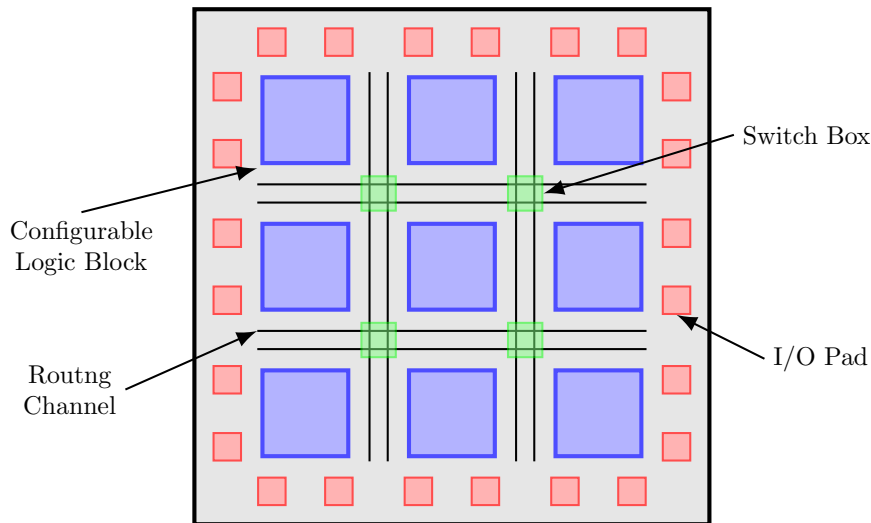


Figure 5.1: Simple FPGA diagram. Real FPGAs can have from the order of hundreds to millions of CLB blocks.

bitwidth blocks that simplify the circuit design, and alleviate the resources requirements. Examples of these complex blocks are multipliers, digital signal processing (DSP) blocks, and block RAMs. Figures 5.2 and 5.3 show the architecture of a CLB and a DSP block respectively, for two different FPGA chips.

FPGAs differ from microcontrollers in that microcontrollers are fixed digital circuits, which is programmed by loading a list of instructions into the instruction memory of the chip. In a microcontroller both the hardware architecture and the instruction set are non-configurable. In contrast, in an FPGA the hardware itself can be reprogrammed, giving the user the ability to create efficient, application-specific circuits of every individual problem, at the expense of more design complexity. FPGAs can also implement systems with a great degree of space parallelism (multiple circuits in a single chip), and time parallelism (multiple dataflows being processed simultaneously by the same circuit¹). All these characteristics make FPGA achieve greater data rates and operating bandwidths, which for some applications, like radio astronomy, make them the hardware of choice.

5.1.2 ROACH2

The specific FPGA platform used to implement the filter was the ROACH2-rev2 board², developed by the CASPER group [36, 37]³, in the University of California, Berkeley. The ROACH2 board uses a Xilinx Virtex-6⁴ FPGA, model XC6VSX475T. The board also comes

¹Also known as pipelining.

²Reconfigurable Open Architecture Computing Hardware. See https://casper.berkeley.edu/wiki/ROACH-2_Revision_2.

³Collaboration for Astronomy Signal Processing and Electronics Research. See https://casper.berkeley.edu/wiki/Main_Page.

⁴See Section 8.3 for a link to datasheets of all the relevant hardware.

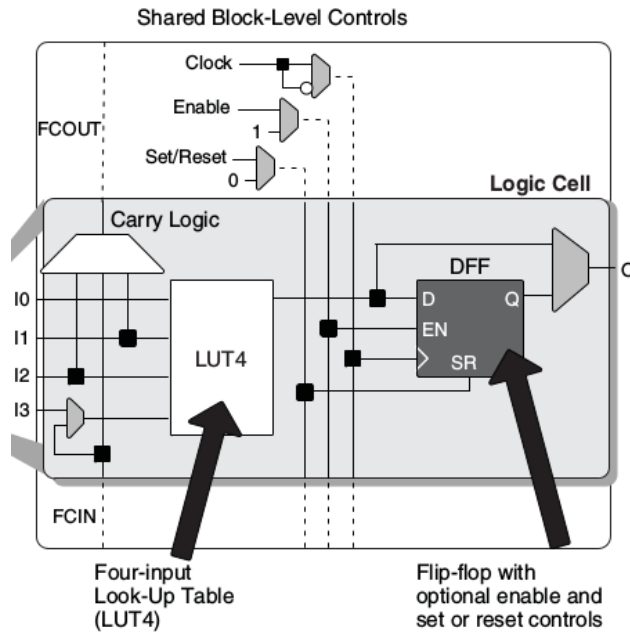


Figure 5.2: Logic cell architecture of the low-end Lattice iCE40 FPGA. The LP8K model of this FPGA contains 7680 of these logic cells. Exrtacted from <http://www.latticesemi.com/~media/LatticeSemi/Documents/DataSheets/iCE/iCE40LPHXFamilyDataSheet.pdf>.

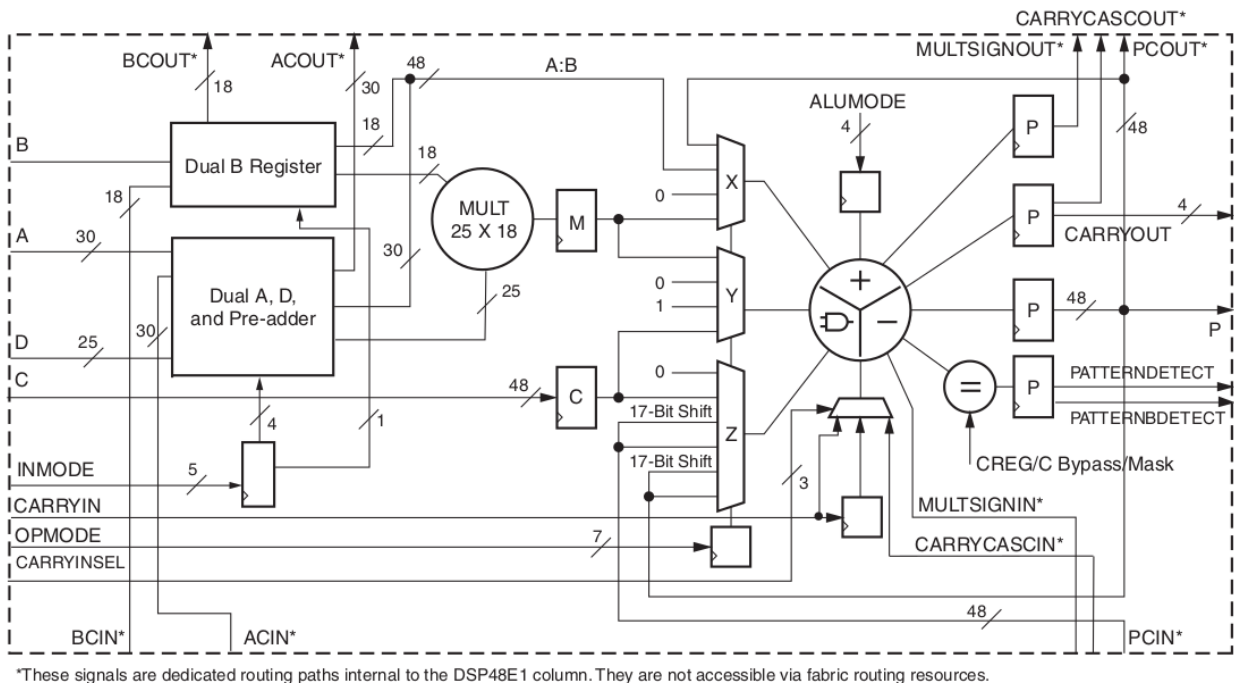


Figure 5.3: DSP block architecture of the high-end Xilinx Virtex-6 FPGA, called the DSP48E1. The XC6VSX475T model of this FPGA contains 2016 the these DSP blocks, alongside with 74400 CLBs (roughly equivalent to 476 160 iCE40's logic cells). Extracted from https://www.xilinx.com/support/documentation/user_guides/ug369.pdf.

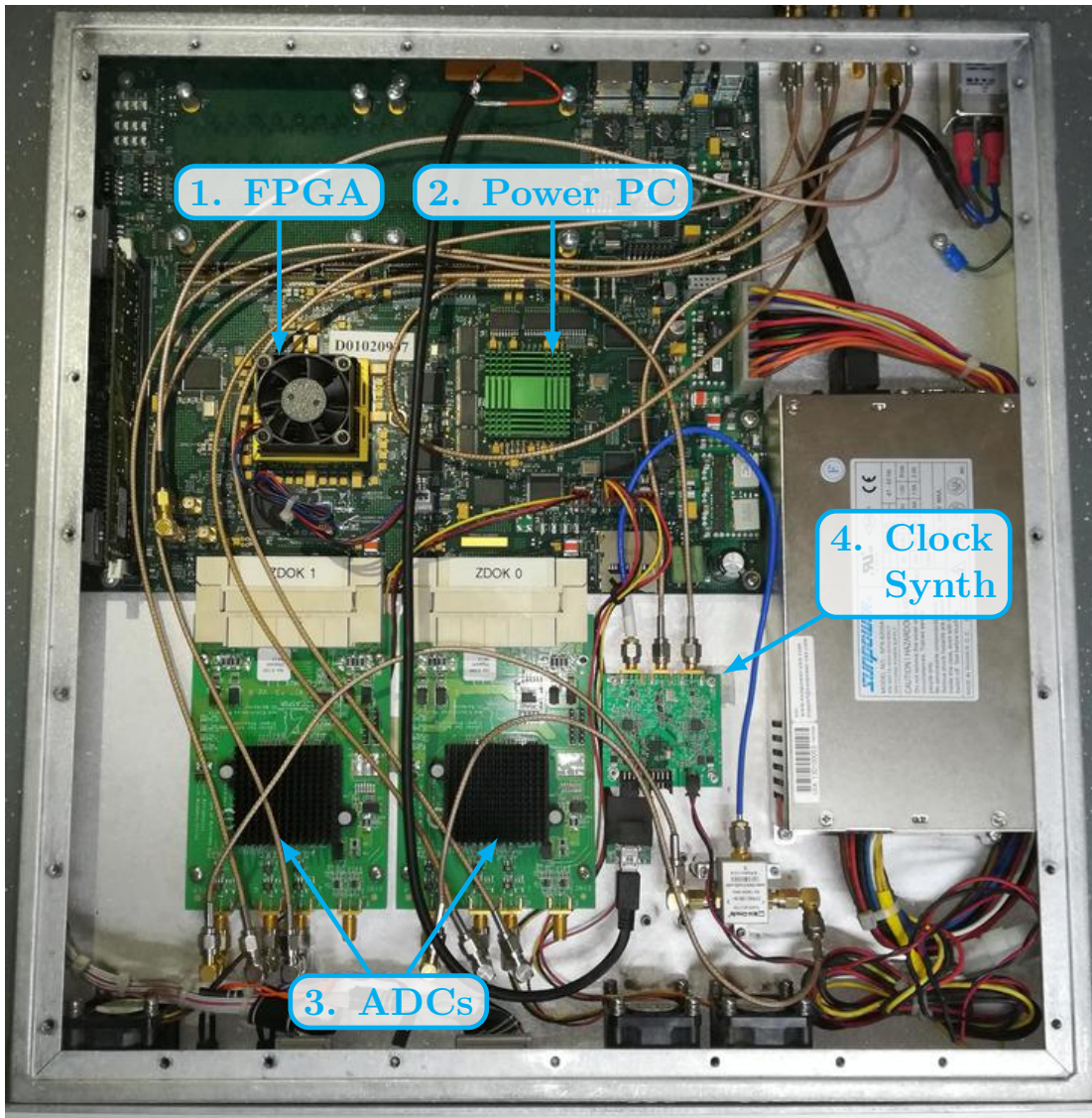


Figure 5.4: Image of the ROACH2-rev2 board. For a list of the components see Section 8.3.1 in the Appendix.

with two ADC5G ADC boards [38]⁵, developed by ASIAA⁶, in Taipei, Taiwan. These boards use the e2V EV8AQ160 ADC chips, which are 8-bits, 5GSPS ADCs. The ADC5Gs are connected through high-performance Z-Dok docking connectors. An image of the board is shown in Figure 5.4. A block diagram for the ROACH2-rev2 can be found in the Appendix (Figure 8.1).

The ROACH2 board uses a 440EPx PowerPC processor running the BORPH [39]⁷ operating system to provide control functions. BORPH is an extended version of the Linux kernel specifically design for FPGAs, were hardware design files are treated as software processes.

⁵<https://casper.berkeley.edu/wiki/ADC1x5000-8>

⁶Academia Sinica Institute for Astronomy and Astrophysics.

⁷Berkeley Operating system for ReProgrammable Hardware. See <https://www.eee.hku.hk/~hso/borph.html>.

The memory resources of the FPGA can be accessed via standard UNIX file pipes, easing the process of programming the ROACH and interchanging data with a computer.

As a communication system, ROACH boards use KATCP⁸, which is a simple text-based protocol for RS232 or TCP/IP connections, developed by CASPER for all their hardware platforms. Client libraries for KATCP are available in many programming languages, including Python⁹. Using these libraries, the user can easily perform many control tasks in the ROACH board directly from computer scripts. Examples of these tasks include programming a model file, reading and writing registers and block RAMs, and uploading and deleting files in the non-volatile memory.

5.2 Hardware Implementation

In the ROACH ecosystem, circuit models are designed in the MATLAB Simulink graphical programming environment¹⁰, where functional block can be interconnected to simulate dynamic systems. In order to produce valid ROACH models, the Xilinx ISE Design Suite¹¹ must be integrated into the Simulink environment. The ISE Design Suite provides both the tools to compile the bitstream file, and a collection of block libraries with mostly basic digital operations (e.g. boolean algebra, binary arithmetic, memory resources).

Using the Xilinx library as a base, the CASPER group developed their own high-level library¹², which provides both complex digital signal processing blocks (white and green blocks), like multi-channel FFT blocks, specialized FIR Filters and Vector Accumulators. It also provides interfacing blocks (yellow blocks) to easily configure input and output ROACH resources (ADCs, registers and block RAMs). The CASPER library is extensively used in the RFI filter implementation.

The actual implementation of the RFI filter was mainly a direct translation of the theoretical diagram in Figure 3.3. Various segments of the final Simulink model are shown in figures 8.2, 8.3 and 8.4 of the Appendix, with its different sections labeled for readability¹³. The model uses two ADC5G ADC, one for the primary and other for the reference channel, running with a clock signal of 1 GHz, provided by a Valon 5007 synthesizer (see Section 8.3.1 in the Appendix). The ADCs were set to work in single channel mode. In this mode, the ADC5G samples both in the rising and falling edge of the clock, so their actual sampling rate was 2 GSPS. Therefore, the system achieved an operating bandwidth of 1 GHz. Since the FPGA chip cannot normally run at such high clock speed, the clock frequency was divided by 16 before is passed to the FPGA. To compensate for the lower speed, 16 consecutive ADC outputs were buffered and enter simultaneously to the FPGA, this means that 16 8-bit inputs must be processed in parallel (this is a good example of the parallelism capabilities of

⁸Karoo Array Telescope Control Protocol. See <https://casper.berkeley.edu/wiki/KATCP>

⁹<https://pypi.org/project/katcp/>

¹⁰<https://www.mathworks.com/products/simulink.html>

¹¹<https://www.xilinx.com/products/design-tools/ise-design-suite.html>

¹²https://github.com/casper-astro/mlib_devel

¹³The model file can be downloaded from this repository: https://github.com/FrancoCalan/simulink_models/blob/master/RFI_Mitigation/ROACH2/kestfilt_4096ch_1080mhz.slx.

Resource	Available in Virtex-6	Model Utilization	Percentage of Utilization
CLB Slices	74400	47986	64%
DSP Blocks	2016	948	47%
Block RAM Memory	38340	11376	30%

Table 5.1: Virtex-6 device utilization summary for the adaptive filter model.

an FPGA).

After the ADC, the digital signals go through a *polyphase filter bank* (PFB), which consists in a specialized FIR filter and a pipeline FFT block (see [34] for a detail explanation on PFBs). The FFT blocks were set to a size 8192 (4096 unique spectral bins), which provide a spectral resolution of 244.14 kHz/bin, and a dynamic range of 86 dB. After the FFT, the signals enter the RFI filter, implemented mostly with blocks from the CASPER library. The power of the filter output, the unfiltered primary channel, and the reference channel were then computed by squaring the magnitudes of their spectral bins. Finally, the three spectra were accumulated, and then saved into block RAMs, where they can be read from an external computer.

The filter model was designed to be reconfigured in real-time, that is, the filter and the spectrometer parameters can be modified on-the-fly, the filter can be turned on and off at will, and the results are immediately visible in an interactive plot. Furthermore, additional circuitry was added to the model to measure the attenuation speed of the filter. Three pieces of data are collected for this propose: the power of a specific (user selectable) bin, the maximum power among spectral bins, and the mean spectral power. These statistics are computed for 1024 consecutive spectra, which can later be plotted in a time scale¹⁴.

Most of the design was done using blocks already implemented either in the CASPER or the Xilinx libraries. The most notable exception is the memory blocks that save the filter parameters G_i , as there exists no block in those libraries that can accumulate data uninterruptedly, and can be controlled by user input. For this reason, the non-stop vector accumulator was designed using Xilinx blocks, as shown in Figure 5.5. These and other auxiliary blocks were added to a fork of the CASPER library¹⁵.

Table 5.1 presents the percentages of the most important FPGA resources utilized by the final model. The complete device utilization report can be found in Section 8.4 of the Appendix.

¹⁴Repository of plotting software: https://github.com/FrancoCalan/roach_tools.

¹⁵Repository link: https://github.com/FrancoCalan/mlib_devel.

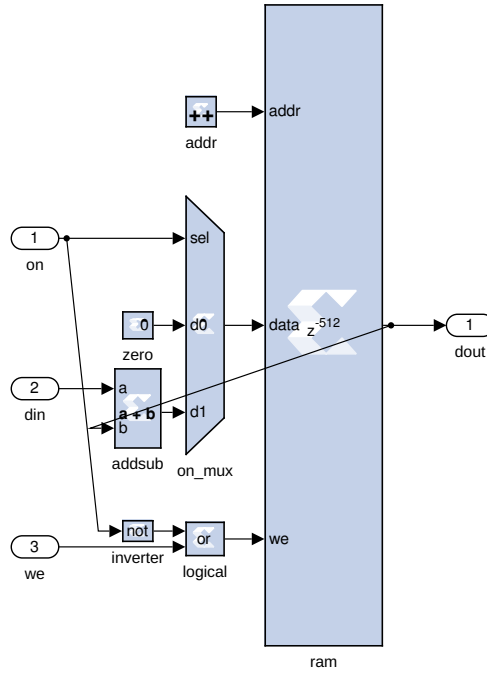


Figure 5.5: Designed Non-stop vector accumulator block. It is essentially an uninterrupted vector accumulator with a control signal to reset its memory.

5.3 Results

5.3.1 Laboratory Tests

The first round of tests to measure the filter performance was done in a controlled laboratory environment, to minimize the effects of noise, multiple RFIs, and multipath. A diagram of the test setup is shown in Figure 5.6. For the astronomical signal, a band-limited noise signal was used, generated from a noise diode. A second noise source provided a wideband noise floor for the astronomical signal, controlled by a variable attenuator. The resulting signal was properly filtered and amplified to utilize the full dynamic range of the ROACH2 ADC. The spectrum of the created signal can be seen in Figure 5.7.

On the other hand, the test interference was created by an arbitrary wave generator, with an up-conversion phase to control its frequency location. The RFI signal was divided with a power splitter, where one copy was mixed with the astronomical signal to create the primary input, while the other goes directly to the reference input. Two types of interference signals were used for this test, a broadband computer-generated noise signal, and complex multiple-carrier signal. The later was recreated from recorded RFI data at the Five Hundred Meter Aperture Spherical Telescope (FAST) [40] site, measured with a reference antenna mounted on top of one of the towers that hold the feed horn cabin of the telescope. The spectra of both RFI signals are shown in Figure 5.8.

The results of the tests are presented in figures 5.9 and 5.10 for the noise and multi-carrier RFI respectively. The filter accumulation length is set to $N = 1$ as it was empirically shown

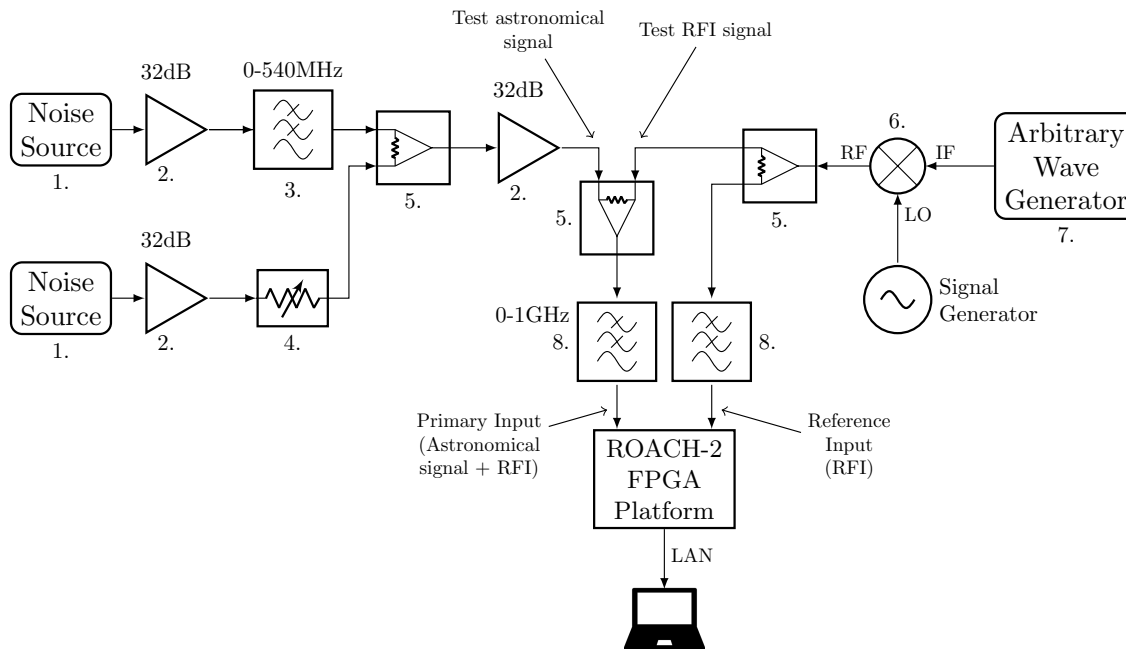


Figure 5.6: Laboratory test setup. For a list of the exact components used see Section 8.3.2 in the Appendix.

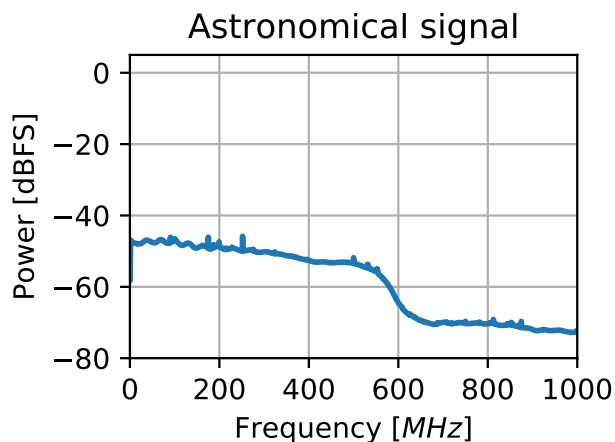


Figure 5.7: Spectrum of astronomical signal for the laboratory test.

that produces the fastest convergence, and the filter gain ε was set to the highest power of 2 that does not make the filter to diverge (2^{15} for noise RFI and 2^{11} for multiple-carrier). From the figures it can be seen that the filter successfully removes the RFI, and the astronomical signal is recovered almost intact. The exact amount of attenuation achieved is 20 dB for the noise RFI and 35 dB for the multiple-carrier. To better visualize the filter performance, the power difference between the astronomical signal and the filter output for both scenarios are plotted in Figure 5.11. The plots show a power difference below 2 dB for most of the band, with a maximum difference of 4 dB.

Finally, using the auxiliary circuitry added to the model, the convergence speed of the filter was analysed. Figure 5.12 shows the filter attenuation level using three metrics: a specific bin in the spectrum, the maximum power among spectral bins, and the mean spectral power. In

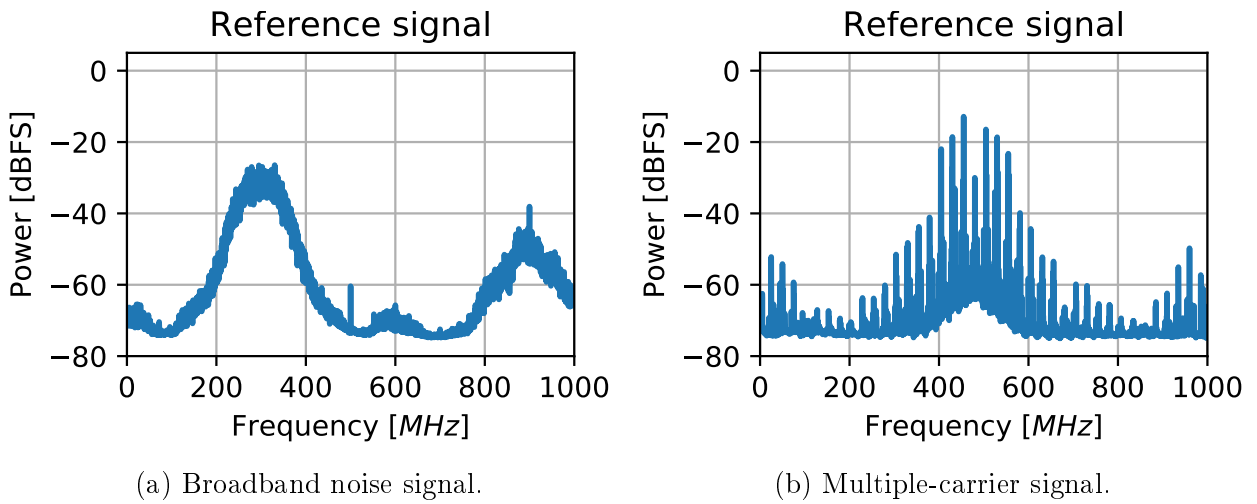


Figure 5.8: Spectra of the interference signals for the laboratory test.

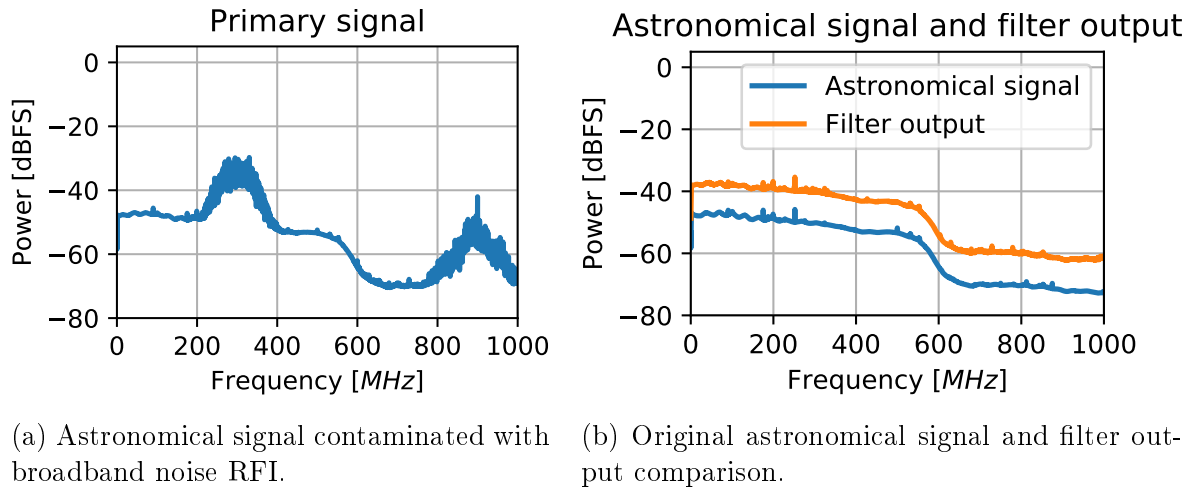


Figure 5.9: Test results for the broadband noise RFI. The filter parameters are $N = 1$ and $\varepsilon = 2^{15}$. The filter output was offset by 10 dB for better visualization.

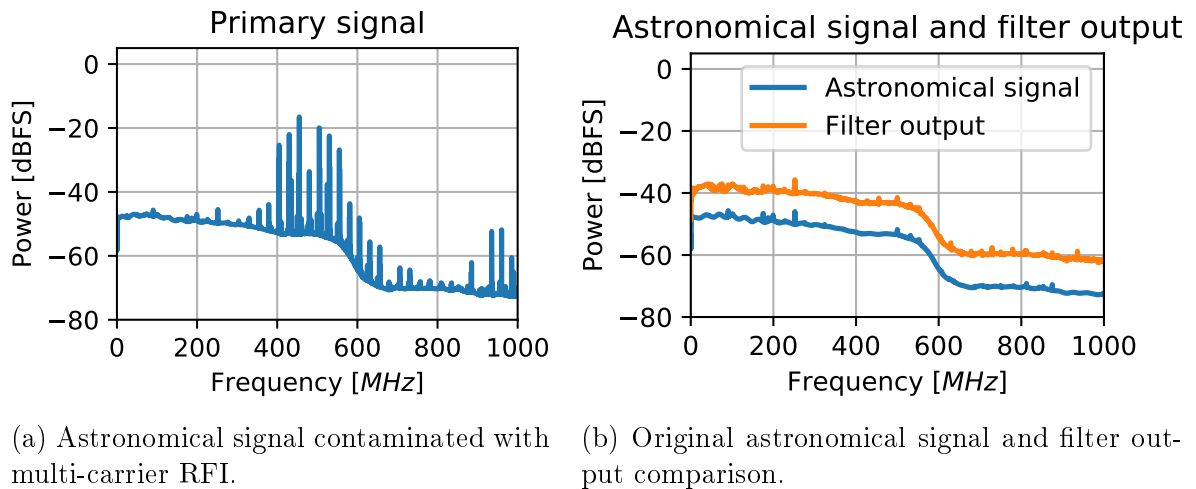


Figure 5.10: Test results for the multi-carrier RFI. The filter parameters are $N = 1$ and $\varepsilon = 2^{11}$. The filter output was offset by 10 dB for better visualization.

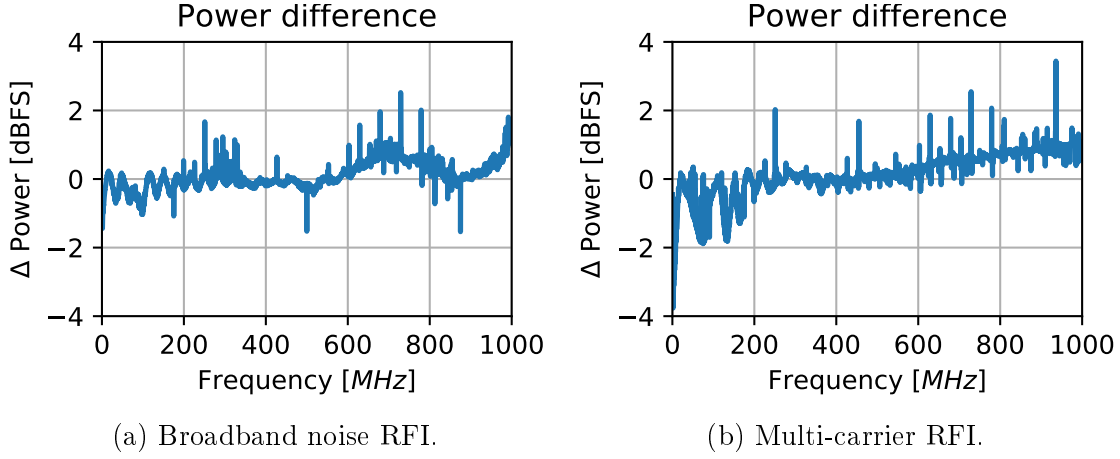


Figure 5.11: Power difference between the astronomical signal and the filter output, for both broadband noise and multi-carrier RFI.

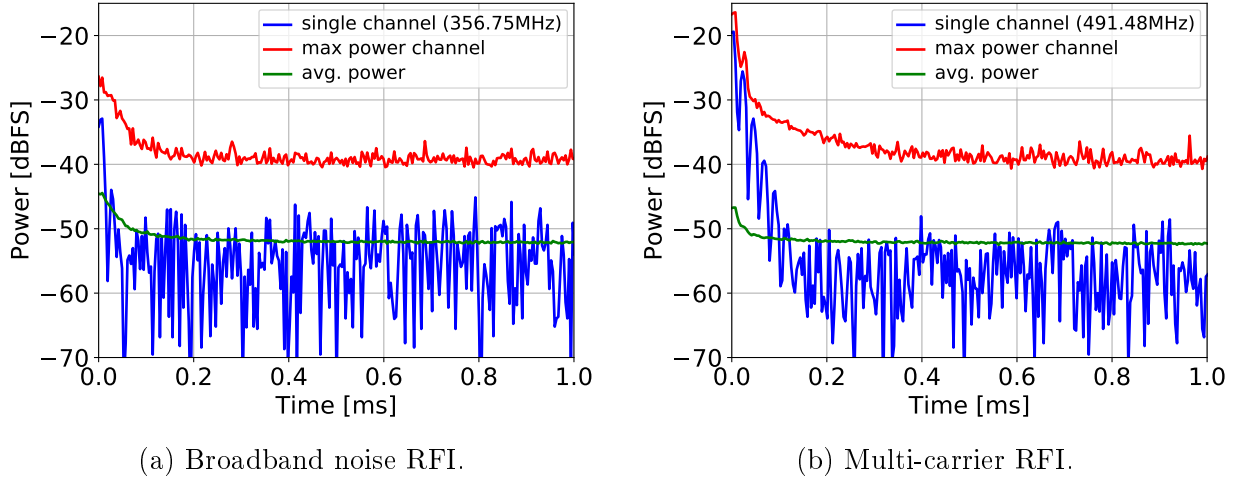


Figure 5.12: Convergence speed for the broadband noise and the multi-carrier RFI. Three convergence metrics are plotted: blue: single bin, red: maximum power among bins, green: mean spectral power. For the single bin plot, the bin with maximum power at $t = 0$ is chosen.

the plots, $t = 0$ indicates the instant the filter is activated, with $G_0 = 0$ as initial condition. To quantify the convergence speed of the filter, first the notion of *attenuation ratio* is defined as the ratio of the mean spectral power at the filter output at times $t = 0$ and $t = n$, minus the astronomical signals power,

$$att\ ratio_n = \frac{mean_{bin}(|F_0|^2) - mean_{bin}(|A_0|^2)}{mean_{bin}(|F_n|^2) - mean_{bin}(|A_n|^2)}, \quad (5.1)$$

where $mean_{bin}$ is the average among all spectral bins. The astronomical signal power must be subtracted so that it does not influence the filter performance metric. Then, the convergence time is computed as the time t_{conv} at which the filter attenuates the interference to 1% its original power. In terms of the attenuation ratio that is

$$t_{conv} = \text{first } n \text{ such as } att\ ratio_n \geq 100. \quad (5.2)$$

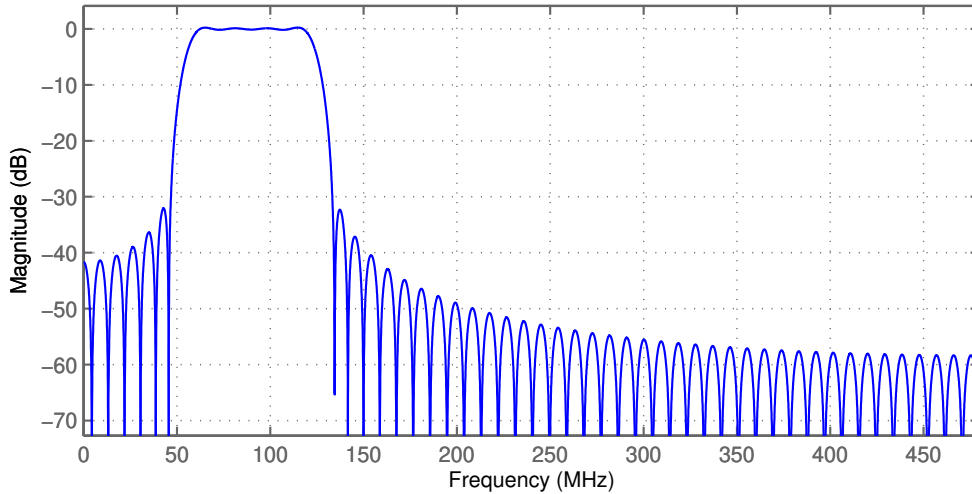


Figure 5.13: Decimation FIR filter frequency response.

Using this formula, the convergence time is $208.1\mu s$ for the broadband noise RFI, and $125.5\mu s$ for the multiple-carrier RFI, which is more than enough to deal with most of radio communication schemes. Convergence time can be even lower if the gain parameter ε were fine-tuned for every specific interference.

5.3.2 FM Radio Tests

The second experiment consisted of measuring and mitigating the FM radio signals present in the environment. Some hardware modifications were done for this test. First, the FPGA board used on the test is the ROACH1 (the previous version of ROACH2) for hardware availability reasons. Second, since the FM radio has a relatively short bandwidth (88-108 MHz), the ROACH1 ADC must be run to its lowest allowable sampling rate, that is, 960 MSPS¹⁶. To further reduce the operating bandwidth, a technique called *decimation* [34] is employed. Decimation consists of combining a number of successive samples of a digital signal in a FIR filter. The number of combined samples indicates the reduction of the sampling rate, which in turns decreases the bandwidth, while the filter coefficients provide the passband frequency location of the decimation system. For this test, a decimation by 8 is used, which provides an operating bandwidth of $480 \text{ MHz}/8 = 60 \text{ MHz}$, and a bandpass FIR filter is implemented to locate the passband at 60-120 MHz. The frequency response of the FIR filter is shown in Figure 5.13, while the modified Simulink model is presented in Figure 8.5 in the Appendix¹⁷.

The tests were performed in three distinct locations. The first one was a corridor in the National Astronomical Observatory building of the University of Chile, in Las Condes, Santiago¹⁸. The second location is an outside parking lot near the same building. The last

¹⁶MSPS: mega-samples per second.

¹⁷The model file can be downloaded from this repository: https://github.com/FrancoCalan/simulink_models/blob/master/RFI_Mitigation/ROACH1/kestfilt_60mhz_fm.slx.

¹⁸Geographical coordinates: $33^{\circ}23'46.2''\text{S } 70^{\circ}32'13.2''\text{W}$. <https://goo.gl/maps/aZ1u9b8HGaeJaMX48>.



(a) Observatory corridor. (b) Observatory parking lot. (c) Rooftop of Electric Department building.

Figure 5.14: The three different locations for the FM radio tests.

location was the rooftop the Electrical Engineer Department building of the University of Chile, in Santiago¹⁹. Pictures of the three locations are shown in Figure 5.14. Notice how all the locations present some number of obstacles that can produce different degrees of multipath propagation.

To measure the FM signals, two standard monopole omnidirectional antennas, the same used in FM radio receivers, were connected directly to the ROACH board. The reference antenna is connected through a 40 m RG-58 coaxial cable, in order to measure the performance of the filter at different distances from the receivers. The use of omnidirectional antennas is not the optimal setup for this test, as they are the most susceptible to multipath propagation and multiple RFIs. They were used anyway because the interference signals come from multiple directions, and their sources have an unknown location.

Spectral images of the filter performance are presented in Figure 5.15. For each location, the distance with the best and worst level of attenuation is shown. It can be seen that, unlike the laboratory test, complete cancellation is not achieved in this case. Instead, attenuation from around 34 dB to as little as 2 dB are observed. Nevertheless, in all the cases the RFI filter never worsen the situation of the interference.

The attenuation ratio was computed for every measured distance, and every tested location, considering only the frequency band of 88-108 MHz. The results are plotted in Figure 5.16. Since this test does not present an astronomical signal, only the quantization noise power of the ADC is subtracted when using the formula (5.1), which is a signal of around -71 dB/bin. From the plot it can be seen that the only location that exhibits a clear downwards tendency with respect to the distance is the parking lot, most probably because is the location with fewer obstacles, which reduces the chances of multipath effects. The results

¹⁹Geographical coordinates: 33°27'29.5"S 70°39'43.4"W. <https://goo.gl/maps/yVMvZbccwUoiUTHe6>.

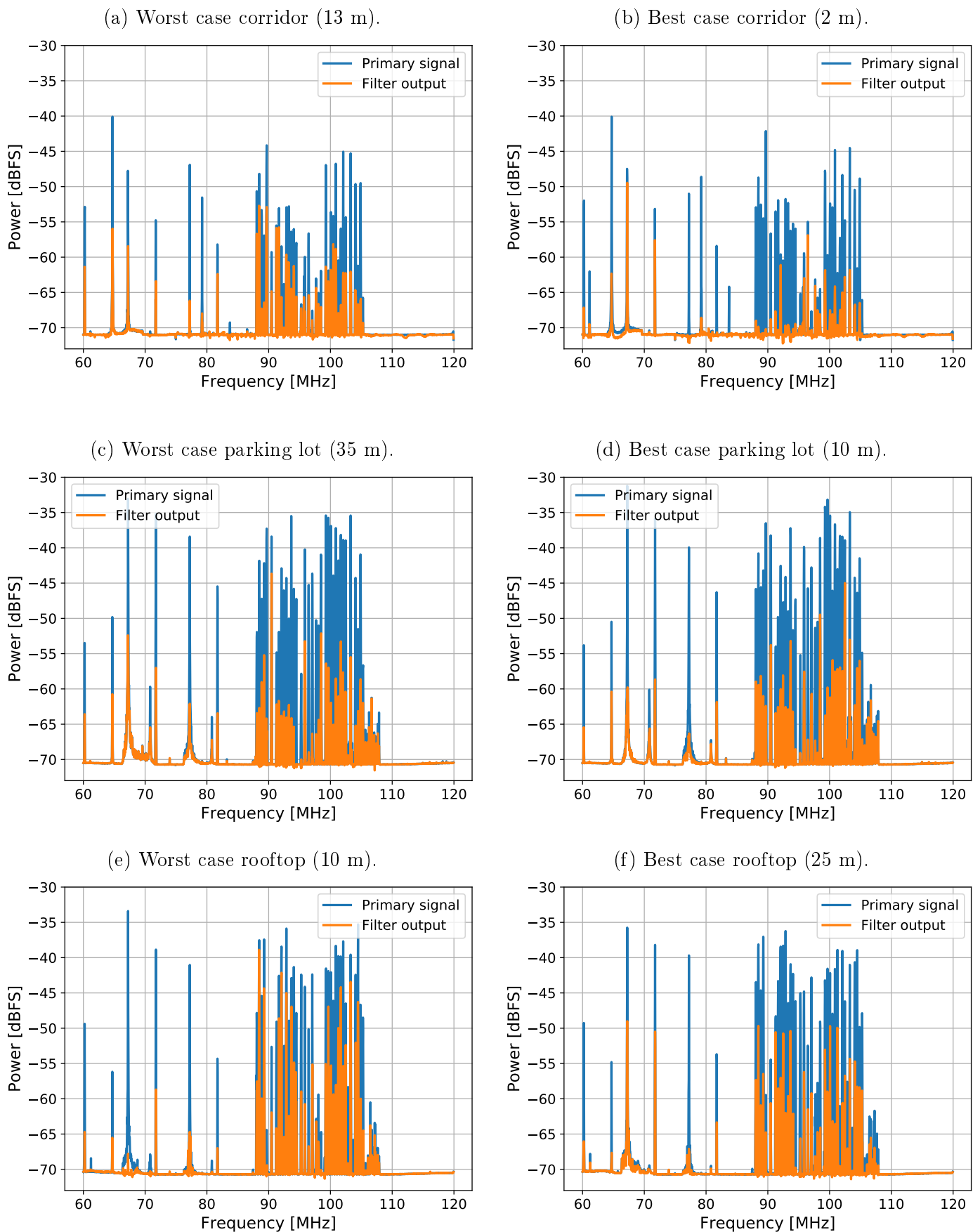


Figure 5.15: Spectra of best and worst mitigation results for the filter, for every location tested.

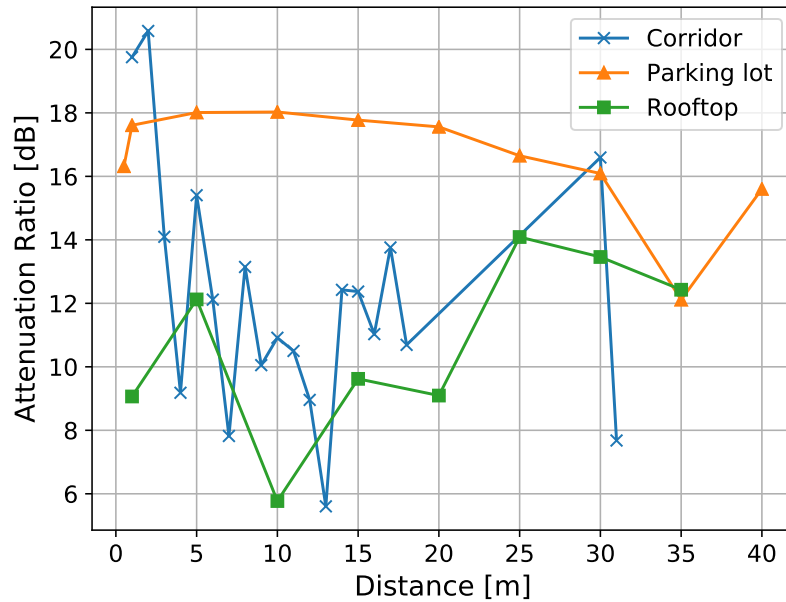


Figure 5.16: Attenuation ratio v/s distance between primary and reference antenna, for all the location tested.

for the corridor are particularly noisy. This is due to the complex geometry of the corridor that produces multiple reflections on the walls and windows, creating sectors of high noise and multipath. For the rooftop data, the attenuation drop at 10 m is caused by the location of the concrete structure at the left of the testing area, which is partially obstructing the interference signals for the reference antenna.

All in all, this experiment shows that RFI mitigation is far more challenging in a real environment than in a laboratory setting. A more careful choice of the test components and setup is needed, as well as a less contaminated area, to optimize the RFI filter results.

5.3.3 Radio Telescope Tests

The final experiment for the RFI filter was performed using a *small radio telescope* (SRT)²⁰ located in the rooftop of the Electrical Engineering Department of the University of Chile. The SRT is a 2.4 m dish telescope developed by the MIT Haystack Observatory, to make spectral line and continuum observations in the L-band (1.42 GHz). Figure 5.17 shows a picture of the SRT. For the reference antenna, a Linx 1.4 GHz omnidirectional dipole was used (see Figure 5.18).

The test consisted in measuring the beamwidth pattern of the SRT by pointing it at the sun, and then performing a horizontal scan from -15° to 15° , with 0° being the center of the sun. By recording the total power measured at each angle, the radiation pattern of the SRT in the scanned direction can be plotted. In radio astronomy, this process is called *sun-pointing*. This experiment was tried in the past using the SRT original back-

²⁰<https://www.haystack.mit.edu/edu/undergrad/srt/oldsrt.html>



Figure 5.17: MIT Small Radio Telescope at the rooftop of the Electrical Engineering Department building.



Figure 5.18: Linx 1.4GHz omnidirectional dipole antenna used as reference antenna. Datasheet: <https://bit.ly/2I7JDx9>.

end and front-end processing chains, meeting several difficulties due to the great amount of interference contamination found at the center of Santiago city.

For this experiment, the ROACH1 board is used, with a very similar circuit model as the one for the FM radio test. The only difference consisted in changing the decimation FIR filter coefficients to position its passband in a different frequency location²¹. Unfortunately, the ROACH1 cannot be connected directly to the SRT's analog front-end, since both the SRT's analog and digital processing chains are integrated in a single printed circuit board. For this reason, a separate analog front-end was created for the experiment. The diagram of this front-end is shown in Figure 5.19, while a picture of the plate built to hold the amplification chain is shown in Figure 5.20. The primary and reference analog chains were built to be mostly equivalent in order to avoid possible mismatches in their frequency responses.

The same decimation technique from the FM tests was used to achieve an operating bandwidth of 60 MHz. Furthermore, to locate the observable band around 1.42 GHz a technique called *undersampling* was implemented. Using undersampling, an ADC can measure frequency components higher than $F_s/2$ by detecting them at lower frequency locations, due to the wrapping effect of aliasing. In this case, the ROACH1 ADC (without considering decimation) has an operating bandwidth of 480 MHz. Then, the first spectral replication occurs between 480-960 MHz, and the second spectral replication between 960-1440 MHz, this effect is portrayed in Figure 5.21. The replicated band locations are called the *nth-Nyquist zones*, with n being the number of spectral wrapping needed to reach the baseband, plus 1. In order

²¹The model file can be downloaded from this repository: https://github.com/FrancoCalan/simulink_models/blob/master/RFI_Mitigation/ROACH1/kestfilt_60mhz_hline.slx.

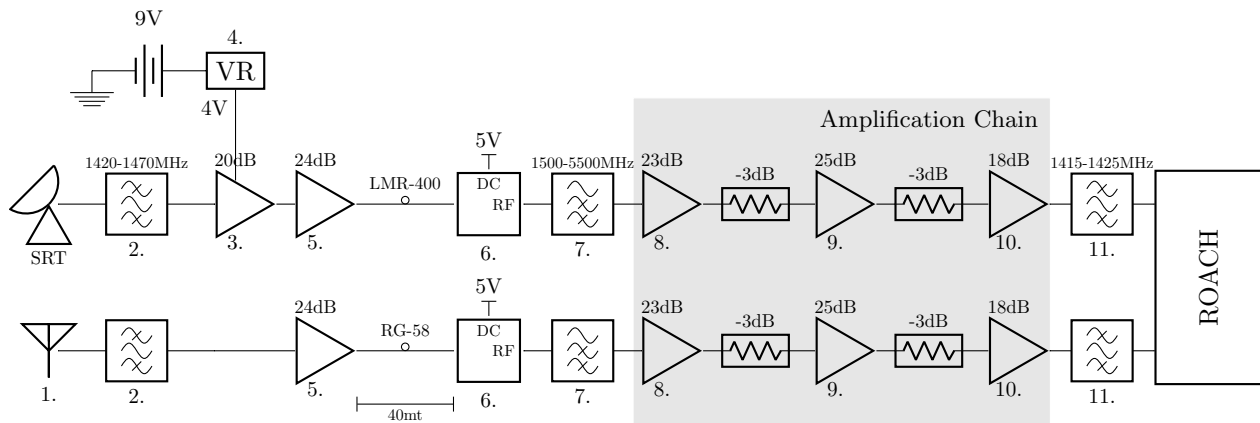


Figure 5.19: SRT analog front-end used for the beamwidth test. For a list of the exact components used see Section 8.3.3 in the Appendix.

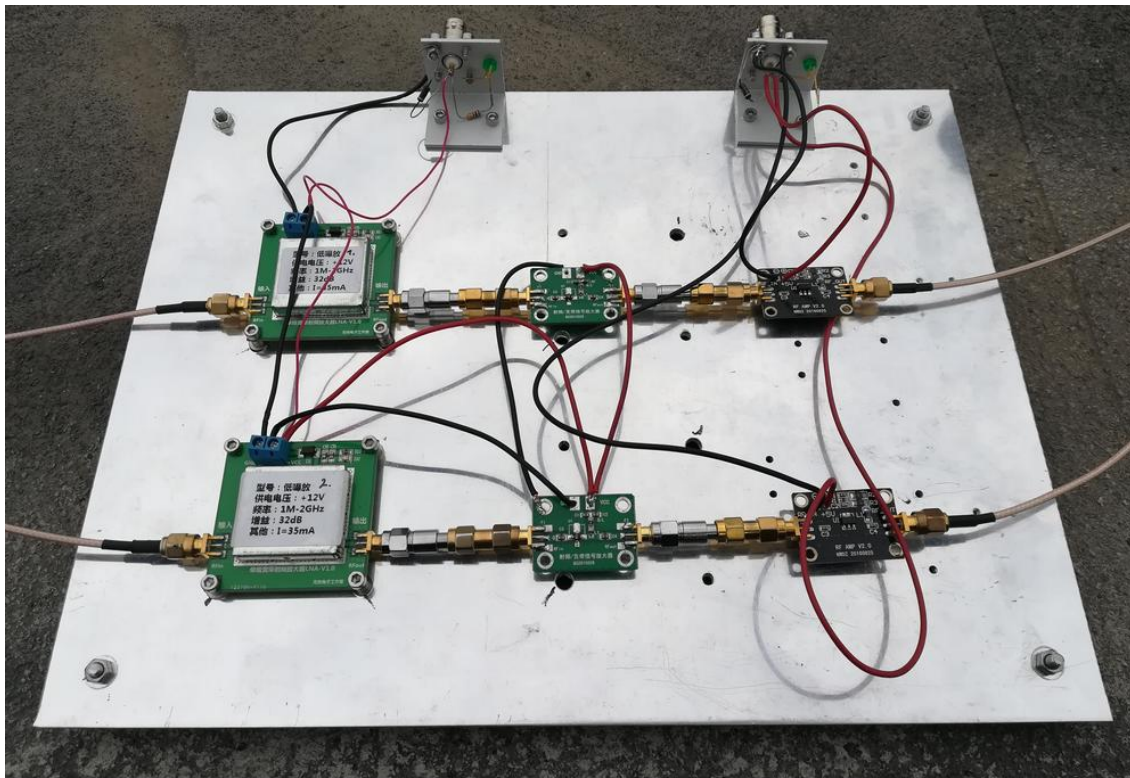


Figure 5.20: Plate with the analog front-end amplification chain.

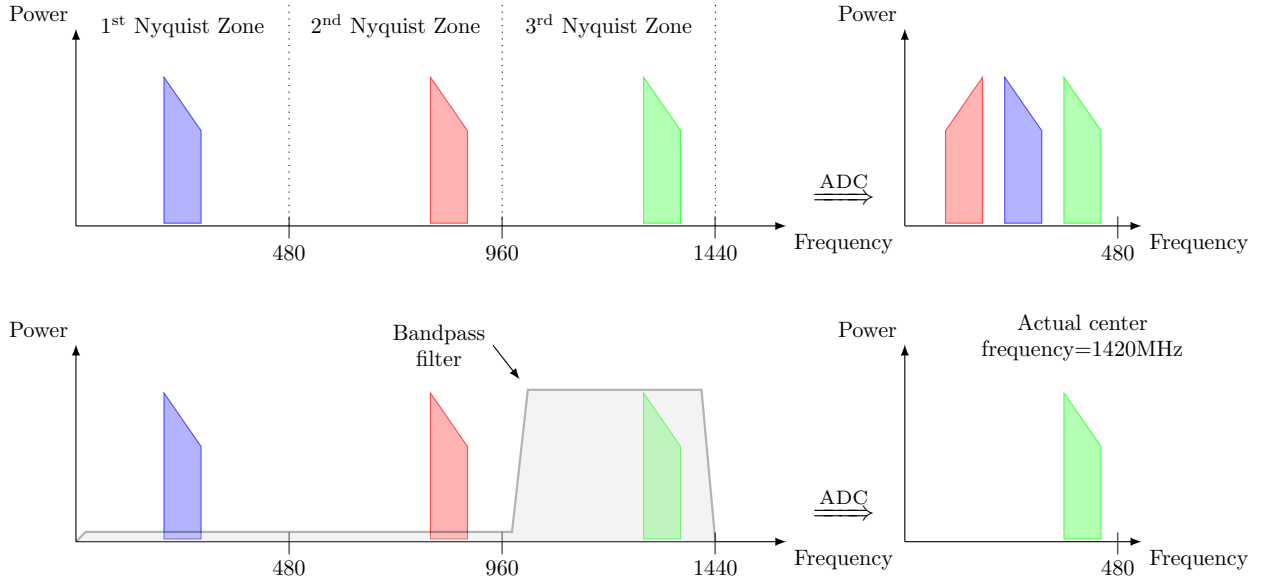


Figure 5.21: Illustration of the undersampling technique. In the first row, no filter is applied, so all the Nyquist zones get wrapped around the baseband. In the second row, a bandpass filter is applied to measure only the zone of interest with the ADC.

to correctly employ undersampling, the unused Nyquist zones must be properly canceled out using a high rejection ratio bandpass filter. For this experiment, two Radio Astronomy Supplies (RAS) bandpass filters were used. These filters were specifically designed for radio astronomy observations at the L-band, with a center frequency of 1420.405 MHz and a rejection ratio of 20 dB around ± 43 MHz. A picture of these filters is shown in Figure 5.22. By combining both the decimation and undersampling techniques, the RFI filter was set to work at the 1380-1440 MHz band.

Figure 5.23 shows the results of a beamwidth measurement with low RFI conditions. Looking at the spectral plots of the primary signal (Figure 5.23b) and filter output (Figure 5.23c), two types of interference signals are identified: electrical oscillations produced in the amplification chain, and actual RFI entering through the telescope. The electrical oscillations are most probably caused by insufficient isolation in the amplifiers DC feed path, since the first two amplifiers of both chains share the same voltage connection from the power supply. This issue is addressed by simply considering only the 1401-1440 MHz band for the beamwidth tests. It should be noticed that, even though it is not the primary concern of this work, the filter is able to partially attenuate the parasitic oscillations generated by the circuit.

From Figure 5.23a, it is seen that the SRT beamwidth can be accurately measured in both the primary signal and the filter output. This is due to the fact that the RFI power is very low and hardly varies on each measured offset (see Figure 5.23d). This types of scenarios are usually encountered around 2 hours either after sunrise, or before sunset, that is, when the SRT is mostly pointing to the West or East.

In Figure 5.24 a case of stronger, spatially changing RFI is presented. This type of scenarios occur almost at any time of the day, but more frequently around noon, when

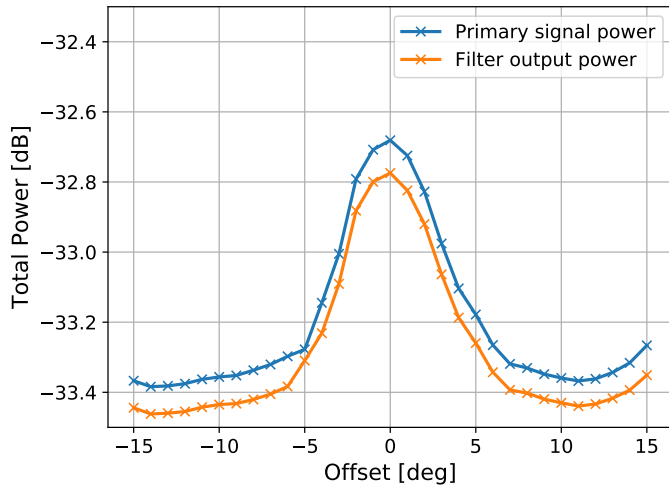


Figure 5.22: Radio Astronomy Supplies bandpass filters.

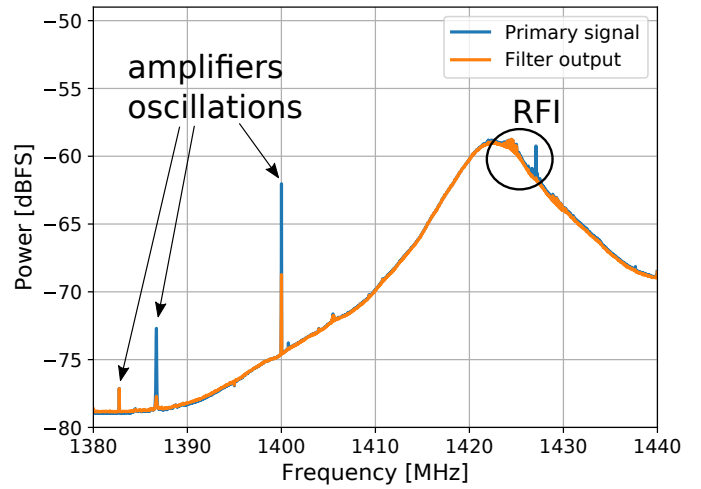
the SRT is pointing mostly to the North and to the center of Santiago. In this case, the interference power increases when the telescope moves from West to East (from a lower to a higher offset), hence corrupting the beamwidth measurement. The filter's curve shows a reduction of power in the corrupted zone, however, this attenuation is not enough to recover a clean beamwidth pattern. The spectral plots confirm that the filter is only capable to mitigate the interference by only a small fraction of its total power, in some cases with attenuations of as little as 1 dB. This interference has an unknown source, but the fact that it is seen continuously during the whole day suggests that it is a broadcast signal that covers a wide area, hence is very much affected by multipath propagation.

In Figure 5.25 a different case of a narrowband, short-time, high power interference is shown. This type of interference is very rarely seen, and can occur at any time of the day. This is also the type of RFI that more heavily damages the beamwidth measurements. In this case, the filter is able to completely remove an interference signal with 15 dB of power over the noise floor, as it is seen in both the beamwidth and the spectral figures. This RFI is successfully mitigated because of its high power, and most probably has a single direction of emission, which reduces the chances of multipath.

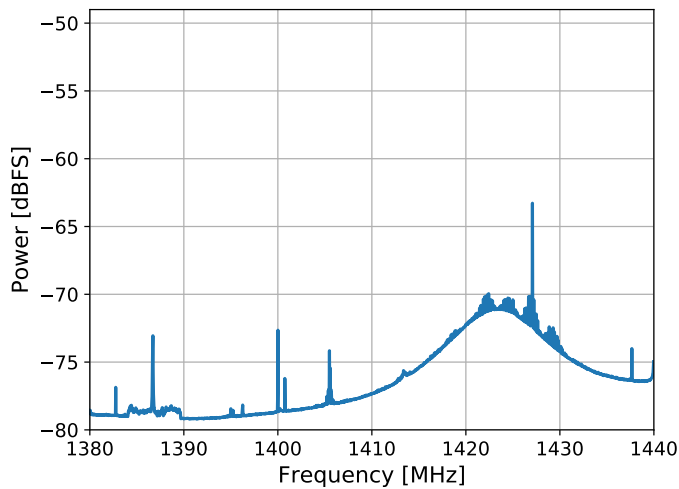
The last test performed was using self-generated interference from a walkie-talkie device put a few meters from the SRT and reference antenna. By continuously clicking the 'push-to-talk' button, a short-time broadband signal is generated, and is captured by both the SRT and the antenna. The results of this tests are presented in Figure 5.26. The plot shows that most of the high power RFI is removed and the beamwidth is almost completely cleaned. This test proves once again that the filter works better for strong, isolated and low noise RFI.



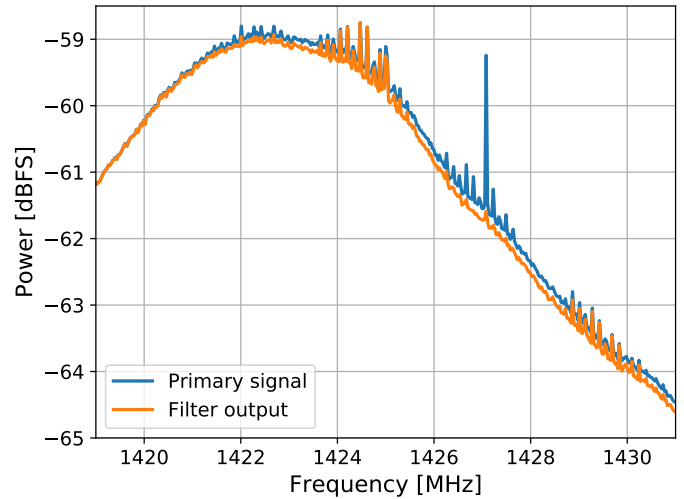
(a) Measured beamwidth at the 1401-1440MHz band.



(b) Primary signal and filter output spectra at offset 0.

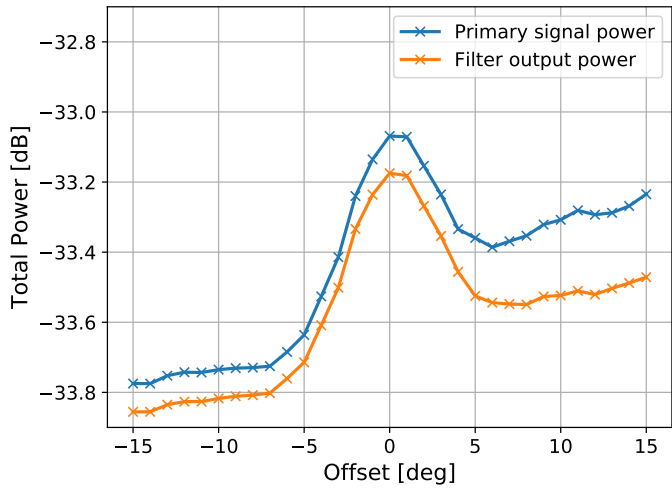


(c) Reference signal spectrum at offset 0.

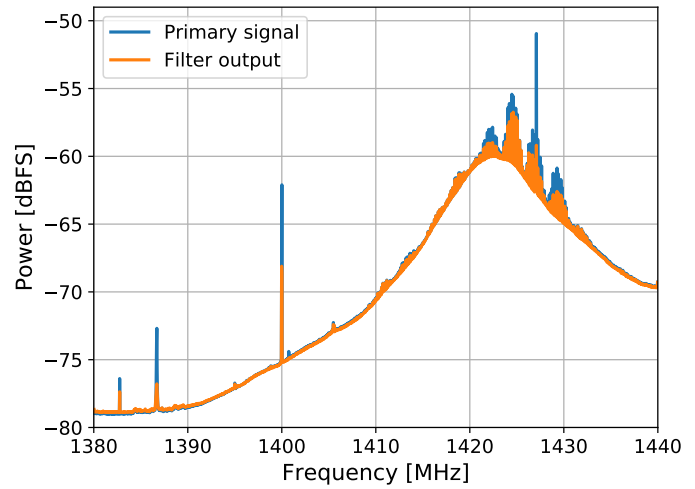


(d) Closeup to the primary signal and filter output spectra.

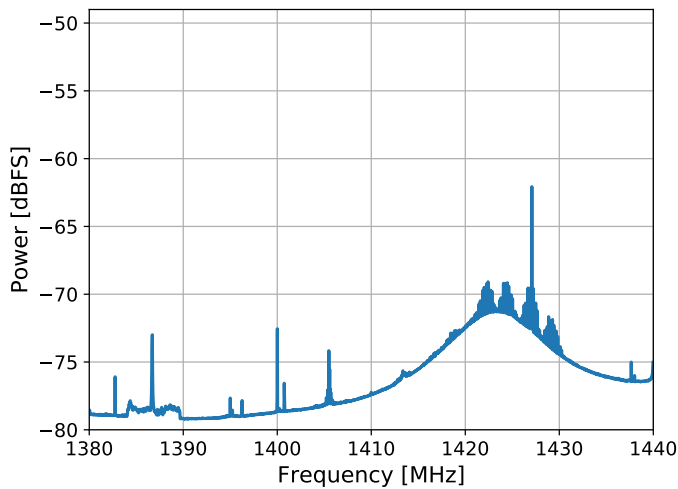
Figure 5.23: SRT test with low power, broadband, static RFI. Performed at 2018-09-08 19:04 local time (UTC-3).



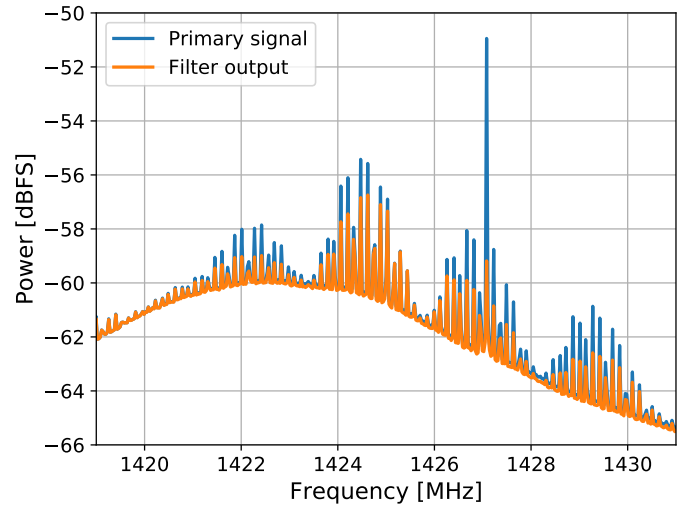
(a) Measured beamwidth at the 1401-1440MHz band.



(b) Primary signal and filter output spectra at offset 15.

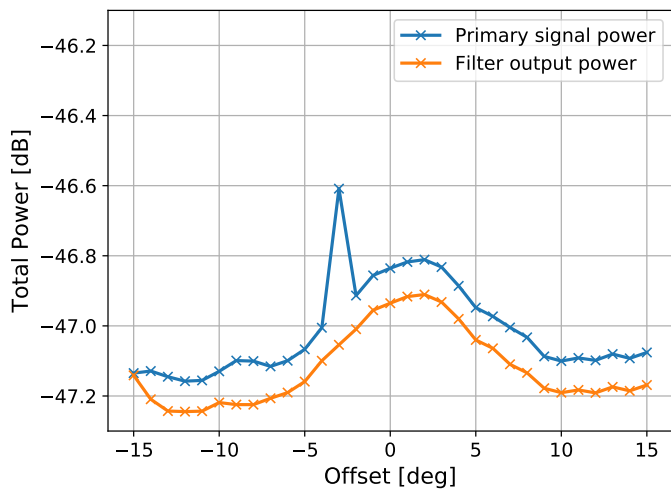


(c) Reference signal spectrum at offset 15.

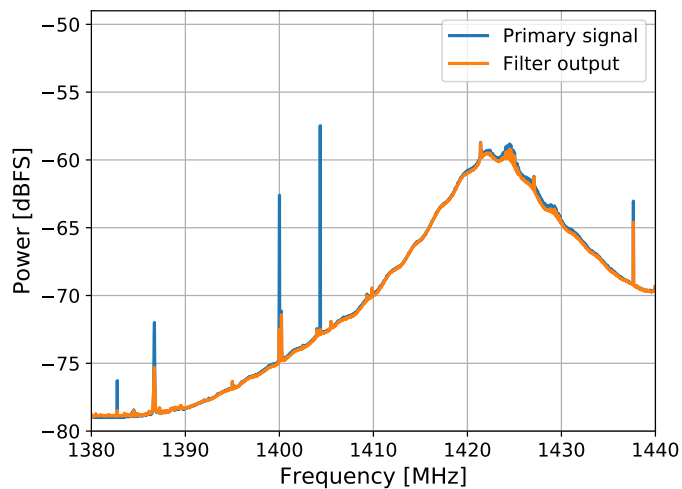


(d) Closeup to the primary signal and filter output spectra.

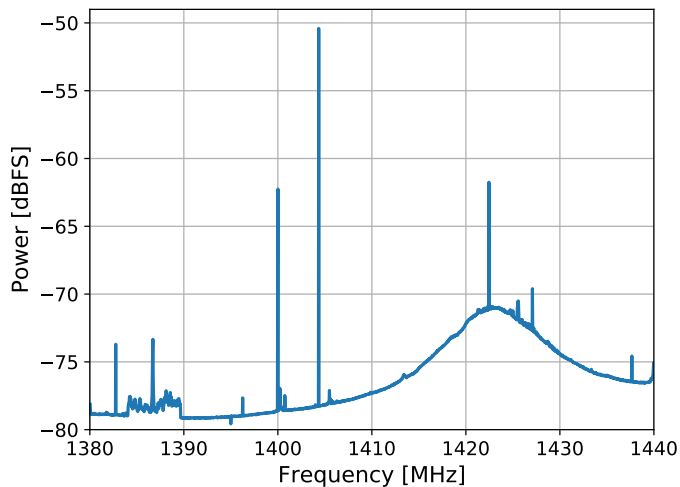
Figure 5.24: SRT test with high power, broadband, spatially changing RFI. Performed at 2018-09-08 17:33 local time (UTC-3).



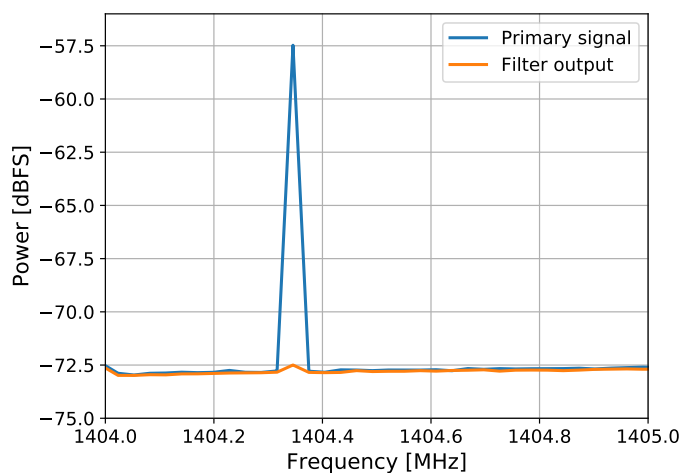
(a) Measured beamwidth at the 1401-1420MHz band.



(b) Primary signal and filter output spectra at offset -3.

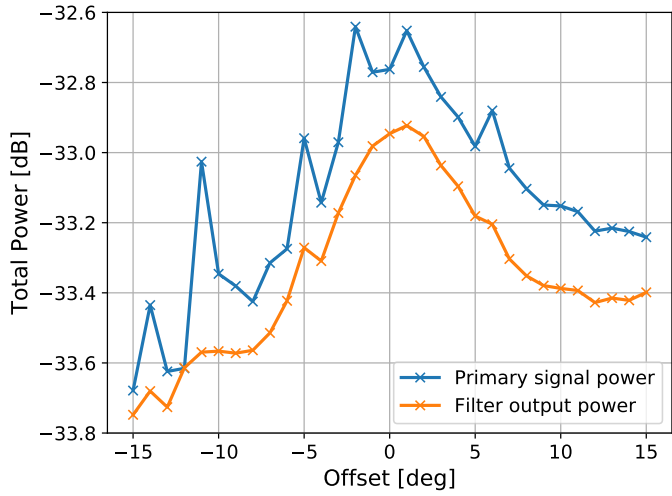


(c) Reference signal spectrum at offset -3.

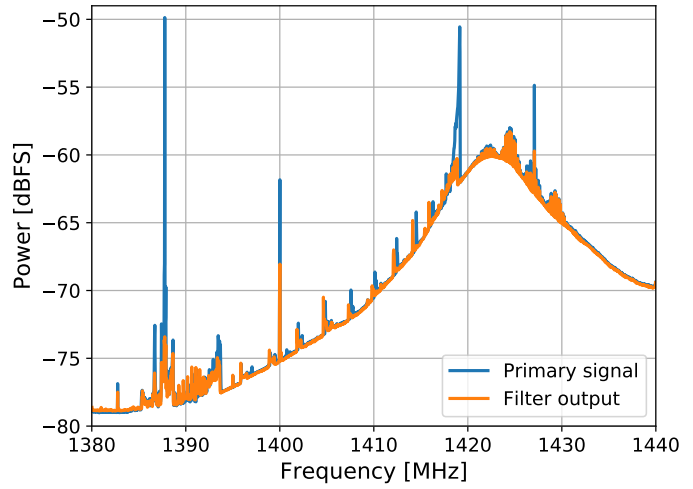


(d) Closeup to the primary signal and filter output spectra.

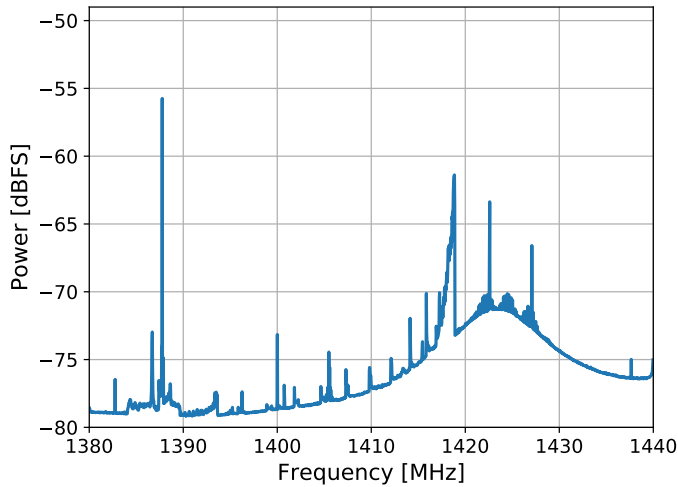
Figure 5.25: SRT test with high power, narrowband, short-time RFI. Performed at 2018-09-07 11:53 local time (UTC-3). The beamwidth was measured in a shorter band to highlight the mitigation of the filter.



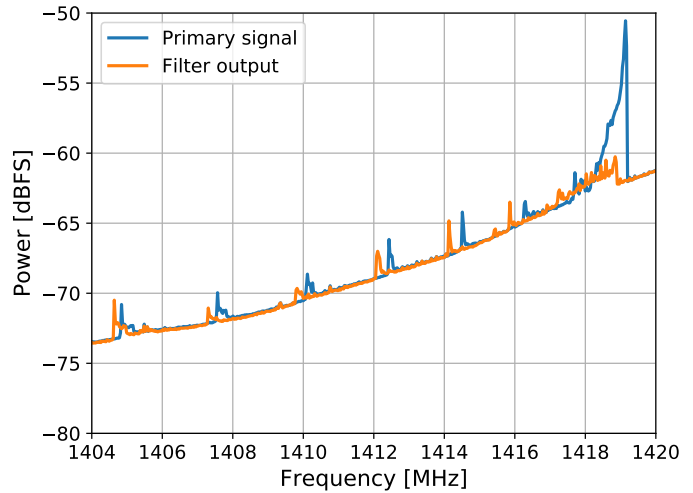
(a) Measured beamwidth at the 1401-1440MHz band.



(b) Primary signal and filter output spectra at offset -11.



(c) Reference signal spectrum at offset -11.



(d) Closeup to the primary signal and filter output spectra.

Figure 5.26: SRT test with high power, broadband, short-time RFI. Performed at 2018-09-08 16:15 local time (UTC-3). The interference is self-generated by continuously activating a walkie-talkie near the SRT and reference antenna.

5.4 Summary

The hardware implementation for the RFI mitigation filter was presented in this chapter. The final design has a bandwidth of 1 GHz, a spectral resolution of 244,24 kHz/bin and a dynamic range of 86 dB. Several test were conducted to measure the performance of the filter. The main conclusions from the tests were that, first, the filter has satisfactory results in the presence of strong narrow-band interference, and secondly, it performances degraded for low-power RFI strongly affected by multipath propagation.

Chapter 6

Conclusions

This thesis presents the design, implementation and testing of a digital radio frequency interference filter, with an emphasis in radio astronomical applications. The final implementation uses two 8 bits ADCs, and has a bandwidth of 1 GHz, a spectral resolution of 244.24 kHz/bin, and a dynamic range of 86 dB.

The proposed filter has several advantages over other studied RFI mitigation techniques, it works in real-time, it cancels out the interference instead of just blanking it, and it has a simple design. The last fact is important because it allows the filter to be implemented fast, high throughput, reconfigurable hardware that can achieve the strict requirements of radio astronomy receivers. Nowadays, many radio telescopes use reconfigurable hardware for their digital back-ends, so incorporating the RFI filter should be easy.

Unfortunately, the implemented filter also presents some disadvantages. The most prominent one is that the filter requires a reference antenna, which in turn requires its own analog front-end that has to be equivalent in bandwidth to the one at the telescope. For single dish telescopes, this means that additional hardware must be put in place, that has its own operational costs.

The mathematical formulation of the RFI filter was extensively studied, and it was proven that the filter should work for every type of interference, as long as the physical medium in which the signals travel satisfy the linear time-invariant condition during the filter convergence. Several limitations of the filter were also studied. All of these limitations have the same nature, in which additional signals are corrupting the correlation computation in the filter, whether these signals are thermal noise, multiple interference sources, or delayed replications of the same interference caused by multipath propagation. Regardless of the origin of the signals, it was proven that the filter would only attenuate the highest power interference, and only to the point where it meets the noise floor, defined as the added power of the rest of the signals.

Several experiments were conducted to test the performance of the filter. The laboratory tests showed that the filter works very well in controlled conditions, being able to completely remove interference of up to 35 dB of power over the noise floor in a span of time of around

200 μ s. More realistic experiments were, however, not completely successful. The main conclusion was that the filter performance varies greatly depending on the nature of the RFI. For high power, localized RFI, the filter was able to eliminate signals of up to 15 dB over the noise floor. On the other hand, for low power RFI, without an specific location of emission, the filter had a poor attenuation of as little as 1 dB. The performance degradation was due to the fact that, unlike the laboratory setup, all the practical limitations got manifested in the realistic experiments, specially the multipath propagation effect. These limitations got accentuated by two factors, first, the use of an omnidirectional reference antenna, which captured interference in all directions, and not only the ones affecting the telescope, and secondly, the high levels of RFI pollution that was present in the test sites. Nevertheless, for the favorable kind of interference, the filter produced successful results, cleaning astronomical data that otherwise would be heavily corrupted.

Aside from its primary function of mitigating environmental RFI, the filter can have other applications in radio astronomy. It has already been proven that the filter can attenuate spur signals generated by the circuitry of analog receivers, like amplifier oscillations and local oscillator leakage. High speed, multi-core ADCs are known to generate spur tones in the digitization process if they are not properly calibrated. By using previous ADC outputs as a reference input, the filter can act as an automatic real-time ADC calibrator. For digitally calibrated receivers, the adaptive algorithm can be used as a faster method to compute the calibration constants, as it is done in hardware rather than software, speeding up the calibration procedure.

As future work, it is suggested to perform new radio astronomical experiments in locations less polluted with RFI, where the interference sources are known and easily locatable. For the reference signal, a high directivity antenna should be used, pointing directly to the RFI source, in order to reduce most of the effect multipath and multiple sources. The relation between the filter performance and its frequency resolution should also be studied. In particular, it is recommended to test if greater resolution is a valid way to combat RFI with high levels of multipath propagation.

Mathematical Symbols

A Astronomical signal (frequency domain).

BW Bandwidth.

BW_{bin} Frequency resolution.

F Filter output.

F_s Sampling frequency.

G Filter parameters.

H_i Impulse response of primary path (frequency domain).

H_r Impulse response of reference path (frequency domain).

I Interference signal at primary telescope (frequency domain).

K Correlation between interference signals.

N Filter accumulation number.

R Interference signal at reference antenna (frequency domain).

RFI Radio frequency interference signal (frequency domain).

ε Filter gain.

a Astronomical signal (time domain).

att ratio Attenuation ratio.

h_i Impulse response of primary path (time domain).

h_r Impulse response of reference path (time domain).

i Interference signal at primary telescope (time domain).

$mean_{bin}$ Average among spectral bins.

r Interference signal at reference antenna (time domain).

r_{fi} Radio frequency interference signal (time domain).

Acronyms

ADC Analog-Digital Converter.

AF Adaptive Filter.

AIPS Astronomical Image Processing System.

ALMA Atacama Large Millimeter/submillimeter Array.

AM Amplitude Modulation.

ANN Artificial Neural Network.

ASSIA Academia Sinica Institute of Astronomy and Astrophysics.

ATCA Australia Telescope Compact Array.

AWGN Additive White Gaussian Noise.

BORPH Berkeley Operating System for ReProgrammable Hardware.

CASPER Collaboration for Astronomy Signal Processing and Electronics Research.

CDMA Code-Division Multiple Access.

CLB Configurable Logic Block.

CPU Control Processing Unit.

CW Continuous Wave.

DC Direct Current.

DFT Discrete Fourier Transform.

DSP Digital Signal Processing.

DSSS Direct Sequence Spread Spectrum.

DWT Discrete Wavelet Transform.

ENOB Effective Number Of Bits.

FAST Five hundred meter Aperture Spherical Telescope.

FDAF Frequency-Domain Adaptive Filter.

FFT Fast Fourier Transform.

FHSS Frequency-Hopping Spread Spectrum.

FIR Finite Impulse Response.

FM Frequency Modulation.

FPGA Field-Programmable Gate Array.

GLONASS GLObal NAVigation Satellite System.

GMM Gaussian Mixture Model.

GMRT Giant Metrewave Radio Telescope.

GPS Global Positioning System.

GSM Global System for Mobile communications.

GSPS GigaSamples Per Second.

HDL Hardware Description Language.

I/O Input/Output.

INR Interference-to-Noise Ratio.

ISE Integrated Synthesis Environment.

ITU International Telecommunication Union.

KATCP Karoo Array Telescope Control Protocol.

KNN K-Nearest Neighbors.

LOFAR LOw-Frequency ARray.

LTI Linear Time-Invariant.

MAD Median Absolute Deviation.

MIT Massachusetts Institute of Technology.

MSE Mean Squared Error.

MSPS MegaSamples Per Second.

PFB Polyphase Filter Bank.

PSD Power Spectral Density.

RADAR RAdio Detection And Ranging.

RAM Random Access Memory.

RAS Radio Astronomy Supplies.

RF Radio Frequency.

RFI Radio Frequency Interference.

ROACH Reconfigurable Open Architecture Computing Hardware.

RQZ Radio Quiet Zone.

SINAD Signal-to-Noise-And-Distortion ratio.

SK Spectral Kurtosis.

SKA Square Kilometre Array.

SNR Signal-to-Noise Ratio.

TCP/IP Transmission Control Protocol/Internet Protocol.

VLA Very Large Array.

WSRT Westerbork Synthesis Radio Telescope.

Chapter 7

Bibliography

- [1] RA Series. Characteristics of radio quiet zones. Technical report, International Telecommunication Union (ITU), Geneva, Switzerland, 09 2012.
- [2] RA Series. Techniques for mitigation of radio frequency interference in radio astronomy. Technical Report 1, International Telecommunication Union (ITU), Geneva, Switzerland, 09 2013.
- [3] RA Series. Protection criteria used for radio astronomical measurements. Technical Report 2, International Telecommunication Union (ITU), Geneva, Switzerland, 2003.
- [4] Federal Communications Commission et al. Fcc online table of frequency allocations. *Online:[<http://www.fcc.gov/oet/spectrum/table/fcctable.pdf>]*, 2008.
- [5] RA Series. Preferred frequency bands for radio astronomical measurements. Technical Report 10, International Telecommunication Union (ITU), Geneva, Switzerland, 06 2003.
- [6] Andriy Konovaltsev, David S De Lorenzo, Achim Hornbostel, and Per Enge. Mitigation of continuous and pulsed radio interference with gnss antenna arrays. In *Proceedings of the 21st International Technical Meeting of the Satellite Division of the Institute of Navigation (ION GNSS'08)*, pages 1291–1300, 2008.
- [7] Amir Leshem, Alle-Jan van der Veen, and Albert-Jan Boonstra. Multichannel Interference Mitigation Techniques in Radio Astronomy. *The Astrophysical Journal Supplement Series*, 131(1):355–373, November 2000.
- [8] P. A. Fridman. Radio frequency interference mitigation with phase-only adaptive beam forming: PHASE ONLY ADAPTIVE BEAM FORMING. *Radio Science*, 40(5):n/a–n/a, October 2005.
- [9] W. M. Lane, A. S. Cohen, N. E. Kassim, T. J W Lazio, R. A. Perley, W. D. Cotton, and E. W. Greisen. Postcorrelation radio frequency interference excision at low frequencies. *Radio Science*, 40(5):1–8, 2005.

- [10] B. Winkel, J. Kerp, and S. Stanko. RFI detection by automated feature extraction and statistical analysis. *Astronomische Nachrichten*, 328(1):68–79, 2007.
- [11] Enno Middelberg. Automated editing of radio interferometer data with PIEFLAG. *Publications of the Astronomical Society of Australia*, 23(2):64–68, 2006.
- [12] A. R. Offringa, A. G. de Bruyn, S. Zaroubi, and M. Biehl. A LOFAR RFI detection pipeline and its first results. *arXiv preprint arXiv:1007.2089*, 2010.
- [13] A. R. Offringa, J. J. van de Gronde, and J. B. T. M. Roerdink. A morphological algorithm for improving radio-frequency interference detection. *Astronomy & Astrophysics*, 539:A95, mar 2012.
- [14] Ramana Athreya. A new approach to mitigation of radio frequency interference in interferometric data. *Astrophysical Journal*, 696(1):885–890, may 2009.
- [15] Frazer Owen and Leonid Kogan. RFI Mitigation in AIPS. The New Task UVRFI. In *Astronomy*, 2010.
- [16] Cornelis Johannes Wolfaardt. *Machine learning approach to radio frequency interference (RFI) classification in radio astronomy*. PhD thesis, Stellenbosch University, 2016.
- [17] David Brodrick, Douglas Taylor, and Joachim Diederich. Recurrent neural networks for narrowband signal detection in the time-frequency domain. In *Bioastronomy 2002: Life Among the Stars*, volume 213, page 483, 2004.
- [18] Noppasin Niamsuwan, Joel T. Johnson, and Steven W. Ellingson. Examination of a simple pulse-blanking technique for radio frequency interference mitigation. *Radio Science*, 40(5):1–11, 2005.
- [19] Kaushal D. Buch, Yashwant Gupta, Shruti Bhatporia, Swapnil Nalawade, Kishor Naik, and B. Ajithkumar. Real-time RFI excision for the GMRT wideband correlator. In *Proceedings of 2016 Radio Frequency Interference: Coexisting with Radio Frequency Interference, RFI 2016*, pages 11–15. IEEE, 2017.
- [20] Dale E. Gary, Zhiwei Liu, and Gelu M. Nita. A Wideband Spectrometer with RFI Detection. *Publications of the Astronomical Society of the Pacific*, 122(891):560–572, 2010.
- [21] Gelu M. Nita, Dale E. Gary, Zhiwei Liu, Gordon J. Hurford, and Stephen M. White. Radio Frequency Interference Excision Using Spectral-Domain Statistics. *Publications of the Astronomical Society of the Pacific*, 119(857):805–827, 2007.
- [22] Cecilia Barnbaum and Richard F Bradley. A New Approach to Interference Excision in Radio Astronomy: Real-Time Adaptive Cancellation. *The Astronomical Journal*, 116(5):2598–2614, 1998.
- [23] F. H. Briggs, J. F. Bell, and M. J. Kesteven. Removing radio interference from contaminated astronomical spectra using an independent reference signal and closure relations.

The Astronomical Journal, 120(6):3351, 2000.

- [24] Michael Kesteven, Richard Manchester, Andrew Brown, and Grant Hampson. RFI Mitigation for Pulsar Observations. *Proceeding of Science*, pages 1–8, 2010.
- [25] Zbigniew Szadkowski, E. D. Fraenkel, and Ad M. Van Den Berg. FPGA/NIOS implementation of an adaptive FIR filter using linear prediction to reduce narrow-band RFI for Radio detection of cosmic rays. In *IEEE Transactions on Nuclear Science*, volume 60, pages 3483–3490. IEEE, 2013.
- [26] José Miguel Tarongi, GF Forte, and Adriano Camps. Experimental study of radio-frequency interference detection algorithms in microwave radiometry. In *Geoscience and Remote Sensing Symposium (IGARSS), 2011 IEEE International*, pages 4213–4216. IEEE, 2011.
- [27] Giuseppe F Forte, Jorge Querol, Adriano Camps, and Merce Vall-Llossera. Real-time rfi detection and mitigation system for microwave radiometers. *IEEE transactions on geoscience and remote sensing*, 51(10):4928–4935, 2013.
- [28] Steven W Ellingson, John D Bunton, and Jon F Bell. Removal of the GLONASS C/A signal from OH spectral line observations using a parametric modeling technique. *The Astrophysical Journal Supplement Series*, 135(1):87, 2001.
- [29] Simon S Haykin. *Adaptive filter theory*. Pearson Education India, 2008.
- [30] JM Blackledge. *Digital Signal Processing: Mathematical and Computational Methods: Software Development and Applications*. London: Horwood Publishing Limited, 2006.
- [31] Ricardo Finger, Patricio Mena, Nicolás Reyes, Rafael Rodríguez, and Leonardo Bronfman. A calibrated digital sideband separating spectrometer for radio astronomy applications. *Publications of the Astronomical Society of the Pacific*, 125(925):263, 2013.
- [32] Andrés Alvear, Ricardo Finger, Roberto Fuentes, Raúl Sapunar, Tom Geelen, Franco Curotto, Rafael Rodríguez, David Monasterio, Nicolás Reyes, Patricio Mena, et al. Fpga-based digital signal processing for the next generation radio astronomy instruments: ultra-pure sideband separation and polarization detection. In *Millimeter, Submillimeter, and Far-Infrared Detectors and Instrumentation for Astronomy VIII*, volume 9914, page 99141E. International Society for Optics and Photonics, 2016.
- [33] Kristen Rohlfs and Thomas L Wilson. *Tools of radio astronomy*. Springer Science & Business Media, 2013.
- [34] Richard G Lyons. *Understanding Digital Signal Processing, 3/E*. Pearson Education India, 2011.
- [35] Walt Kester. Mt-001: Taking the mystery out of the infamous formula, " $\text{snr} = 6.02 n + 1.76 \text{ db}$," and why you should care. *REV. 0*, pages 10–03, 2005.
- [36] Aaron Parsons, Don Backer, Chen Chang, Daniel Chapman, Henry Chen, Pierre Droz,

Christina De Jesus, David Macmahon, Andrew Siemion, Dan Werthimer, et al. A new approach to radio astronomy signal processing: packet switched, fpga-based, upgradeable, modular hardware and reusable, platform-independent signal processing libraries. In *In: Proceedings of the XXXth General Assembly of the International Union of Radio Science*. Citeseer, 2006.

- [37] Jack Hickish, Zuhra Abdurashidova, Zaki Ali, Kaushal D Buch, Sandeep C Chaudhari, Hong Chen, Matthew Dexter, Rachel Simone Domagalski, John Ford, Griffin Foster, et al. A decade of developing radio-astronomy instrumentation using casper open-source technology. *Journal of Astronomical Instrumentation*, 5(04):1641001, 2016.
- [38] Homin Jiang, Howard Liu, Kim Guzzino, Derek Kubo, Chao-Te Li, Ray Chang, and Ming-Tang Chen. A 5 giga samples per second 8-bit analog to digital printed circuit board for radio astronomy. *Publications of the Astronomical Society of the Pacific*, 126(942):761, 2014.
- [39] Hayden Kwok-Hay So and Robert W Brodersen. *BORPH: An operating system for FPGA-based reconfigurable computers*. University of California, Berkeley, 2007.
- [40] Rendong Nan, Di Li, Chengjin Jin, Qiming Wang, Lichun Zhu, Wenbai Zhu, Haiyan Zhang, Youling Yue, and Lei Qian. The five-hundred-meter aperture spherical radio telescope (fast) project. *International Journal of Modern Physics D*, 20(06):989–1024, 2011.

Chapter 8

Appendix

8.1 Mathematical Derivation of the Adaptive Filter for Multiples RFI

Consider the following definitions for the interference signals measured by the telescope and the reference antenna respectively

$$I_n = I_{1,n} + I_{2,n} \quad (8.1)$$

$$R_n = R_{1,n} + R_{2,n}. \quad (8.2)$$

Where signals generated by the same source are correlated, while signals from different sources present no correlation, as per Figure 4.4. The astronomical signal is represented as A_n . With this setup, the analysis for the filter parameters G_i become equivalent to the one in Section 3.4.3, resulting in equation (3.29),

$$G_{i+1} = \underbrace{\varepsilon \frac{1}{N} \sum_{j=Ni}^{N(i+1)-1} A_j R_j^*}_{(a)} + \underbrace{\varepsilon \frac{1}{N} \sum_{j=Ni}^{N(i+1)-1} I_j R_j^*}_{(b)} - \varepsilon G_i \underbrace{\frac{1}{N} \sum_{j=Ni}^{N(i+1)-1} R_j R_j^*}_{(c)} + G_i. \quad (8.3)$$

From this point, every term of the above expression is analyzed separately. For simplification sake, it is assumed that the accumulation number N is large enough to make uncorrelated accumulated products negligible. Then (a) becomes

$$(a) = \varepsilon \frac{1}{N} \sum_{j=Ni}^{N(i+1)-1} A_j R_j^* \quad (8.4)$$

$$= \varepsilon \frac{1}{N} \sum_{j=Ni}^{N(i+1)-1} A_j (R_{1,j} + R_{2,j})^* \quad (8.5)$$

$$= \varepsilon \frac{1}{N} \sum_{j=Ni}^{N(i+1)-1} A_j R_{1,j}^* + A_j R_{2,j}^* \quad (8.6)$$

$$= \varepsilon \frac{1}{N} \underbrace{\sum_{j=Ni}^{N(i+1)-1} A_j R_{1,j}^*}_{=0} + \varepsilon \frac{1}{N} \underbrace{\sum_{j=Ni}^{N(i+1)-1} A_j R_{2,j}^*}_{=0} \quad (8.7)$$

$$= 0. \quad (8.8)$$

For (b),

$$(b) = \varepsilon \frac{1}{N} \sum_{j=Ni}^{N(i+1)-1} I_j R_j^* \quad (8.9)$$

$$= \varepsilon \frac{1}{N} \sum_{j=Ni}^{N(i+1)-1} (I_{1,j} + I_{2,j})(R_{1,j} + R_{2,j})^* \quad (8.10)$$

$$= \varepsilon \frac{1}{N} \sum_{j=Ni}^{N(i+1)-1} I_{1,j} R_{1,j}^* + I_{1,j} R_{2,j}^* + I_{2,j} R_{1,j}^* + I_{2,j} R_{2,j}^* \quad (8.11)$$

$$= \varepsilon \frac{1}{N} \underbrace{\sum_{j=Ni}^{N(i+1)-1} I_{1,j} R_{1,j}^*}_{=K_1} + \varepsilon \frac{1}{N} \underbrace{\sum_{j=Ni}^{N(i+1)-1} I_{1,j} R_{2,j}^*}_{=0} + \varepsilon \frac{1}{N} \underbrace{\sum_{j=Ni}^{N(i+1)-1} I_{2,j} R_{1,j}^*}_{=0} + \varepsilon \frac{1}{N} \underbrace{\sum_{j=Ni}^{N(i+1)-1} I_{2,j} R_{2,j}^*}_{=K_2} \quad (8.12)$$

$$= K_1 + K_2. \quad (8.13)$$

Where $K_1 := I_{1,j} R_{1,j}^*$, and $K_2 = I_{2,j} R_{2,j}^*$. For (c),

$$(c) = \varepsilon \frac{1}{N} \sum_{j=Ni}^{N(i+1)-1} R_j R_j^* \quad (8.14)$$

$$= \varepsilon \frac{1}{N} \sum_{j=Ni}^{N(i+1)-1} (R_{1,j} + R_{2,j})(R_{1,j} + R_{2,j})^* \quad (8.15)$$

$$= \varepsilon \frac{1}{N} \sum_{j=Ni}^{N(i+1)-1} R_{1,j} R_{1,j}^* + R_{1,j} R_{2,j}^* + R_{2,j} R_{1,j}^* + R_{2,j} R_{2,j}^* \quad (8.16)$$

$$= \varepsilon \frac{1}{N} \underbrace{\sum_{j=Ni}^{N(i+1)-1} R_{1,j} R_{1,j}^*}_{=r_1^2} + \varepsilon \frac{1}{N} \underbrace{\sum_{j=Ni}^{N(i+1)-1} R_{1,j} R_{2,j}^*}_{=0} + \varepsilon \frac{1}{N} \underbrace{\sum_{j=Ni}^{N(i+1)-1} R_{2,j} R_{1,j}^*}_{=0} + \varepsilon \frac{1}{N} \underbrace{\sum_{j=Ni}^{N(i+1)-1} R_{2,j} R_{2,j}^*}_{=r_2^2} \quad (8.17)$$

$$= r_1^2 + r_2^2. \quad (8.18)$$

Where $r_1^2 := |R_{1,n}|^2 = R_{1,n} R_{1,n}^*$, and $r_2^2 := |R_{2,n}|^2 = R_{2,n} R_{2,n}^*$. Then the expression for G_i becomes

$$G_i = \varepsilon(K_1 + K_2) - \varepsilon(r_1^2 + r_2^2)G_i + G_i \quad (8.19)$$

$$= \underbrace{(1 - \varepsilon(r_1^2 + r_2^2))}_{:=\widehat{b}} G_i + \varepsilon \underbrace{(K_1 + K_2)}_{:=\widehat{K}} \quad (8.20)$$

$$G_i = \widehat{b}G_i + \varepsilon\widehat{K}. \quad (8.21)$$

As seen in Section 4.2, the solution for this type of difference equation is given by

$$G_i = \frac{\widehat{K}}{r_1^2 + r_2^2} (1 - \widehat{b}^i). \quad (8.22)$$

Replacing the obtained expression for G_i into the filter output in equation (3.26),

$$F_{i,n} = A_n + I_n - G_i R_n \quad (8.23)$$

$$= A_n + I_n - \frac{\widehat{K}}{r_1^2 + r_2^2} (1 - \widehat{b}^i) R_n \quad (8.24)$$

$$F_{i,n} = A_n + I_n - \frac{\widehat{K}}{r_1^2 + r_2^2} R_n + \frac{\widehat{K}}{r_1^2 + r_2^2} R_n \widehat{b}^i. \quad (8.25)$$

For simplification sake, it is assumed that the filter has already converged, that is $\widehat{b}^i \xrightarrow{i \rightarrow \infty} 0$. Then,

$$F_{i,n} = A_n + I_n - \frac{\widehat{K}}{r_1^2 + r_2^2} R_n \quad (8.26)$$

$$= A_n + I_n - \frac{K_1 + K_2}{r_1^2 + r_2^2} (R_{1,n} + R_{2,n}) \quad (8.27)$$

$$= A_n + I_n - \frac{1}{r_1^2 + r_2^2} \underbrace{K_1 R_{1,n}}_{=r_1^2 I_{1,n}} - \frac{1}{r_1^2 + r_2^2} K_1 R_{2,n} - \frac{1}{r_1^2 + r_2^2} K_2 R_{1,n} - \frac{1}{r_1^2 + r_2^2} \underbrace{K_2 R_{2,n}}_{=r_2^2 I_{2,n}} \quad (8.28)$$

$$= A_n + I_n - \frac{r_1^2}{r_1^2 + r_2^2} I_{1,n} - \frac{1}{r_1^2 + r_2^2} I_{1,n} R_{1,n}^* R_{2,n} - \frac{1}{r_1^2 + r_2^2} I_{2,n} R_{2,n}^* R_{1,n} - \frac{r_2^2}{r_1^2 + r_2^2} I_{2,n} \quad (8.29)$$

$$= A_n + I_{1,n} + I_{2,n} - \frac{r_1^2}{r_1^2 + r_2^2} I_{1,n} - \frac{R_{1,n}^* R_{2,n}}{r_1^2 + r_2^2} I_{1,n} - \frac{R_{1,n} R_{2,n}^*}{r_1^2 + r_2^2} I_{2,n} - \frac{r_2^2}{r_1^2 + r_2^2} I_{2,n} \quad (8.30)$$

$$= A_n + \underbrace{\left(1 - \frac{r_1^2}{r_1^2 + r_2^2} - \frac{R_{1,n}^* R_{2,n}}{r_1^2 + r_2^2}\right)}_{:=J_{1,n}} I_{1,n} + \underbrace{\left(1 - \frac{r_2^2}{r_1^2 + r_2^2} - \frac{R_{1,n} R_{2,n}^*}{r_1^2 + r_2^2}\right)}_{:=J_{2,n}} I_{2,n} \quad (8.31)$$

$$F_{i,n} = A_n + J_{1,n} + J_{2,n}. \quad (8.32)$$

To quantify the effect of the multiple RFI, the magnitude $|J_{1,n}|$ is computed,

$$|J_{1,n}| = \left| 1 - \frac{r_1^2}{r_1^2 + r_2^2} - \frac{R_{1,n}^* R_{2,n}}{r_1^2 + r_2^2} \right| |I_{1,n}| \quad (8.33)$$

$$= \left| 1 - \frac{r_1^2}{r_1^2 + r_2^2} - \frac{R_{1,n} R_{2,n}^*}{r_1^2 + r_2^2} \right| |I_{1,n}| \quad (8.34)$$

$$\leq \left(\left| 1 - \frac{r_1^2}{r_1^2 + r_2^2} \right| + \left| \frac{R_{1,n}^* R_{2,n}}{r_1^2 + r_2^2} \right| \right) |I_{1,n}| \quad (8.35)$$

$$= \left(\frac{r_2^2}{r_1^2 + r_2^2} + \frac{r_1 r_2}{r_1^2 + r_2^2} \right) |I_{1,n}| \quad (8.36)$$

$$= \frac{r_1 r_2 + r_2^2}{r_1^2 + r_2^2} |I_{1,n}| \quad (8.37)$$

$$\Rightarrow |J_{1,n}| \leq \frac{\frac{r_1}{r_2} + 1}{\left(\frac{r_1}{r_2}\right)^2 + 1} |I_{1,n}|. \quad (8.38)$$

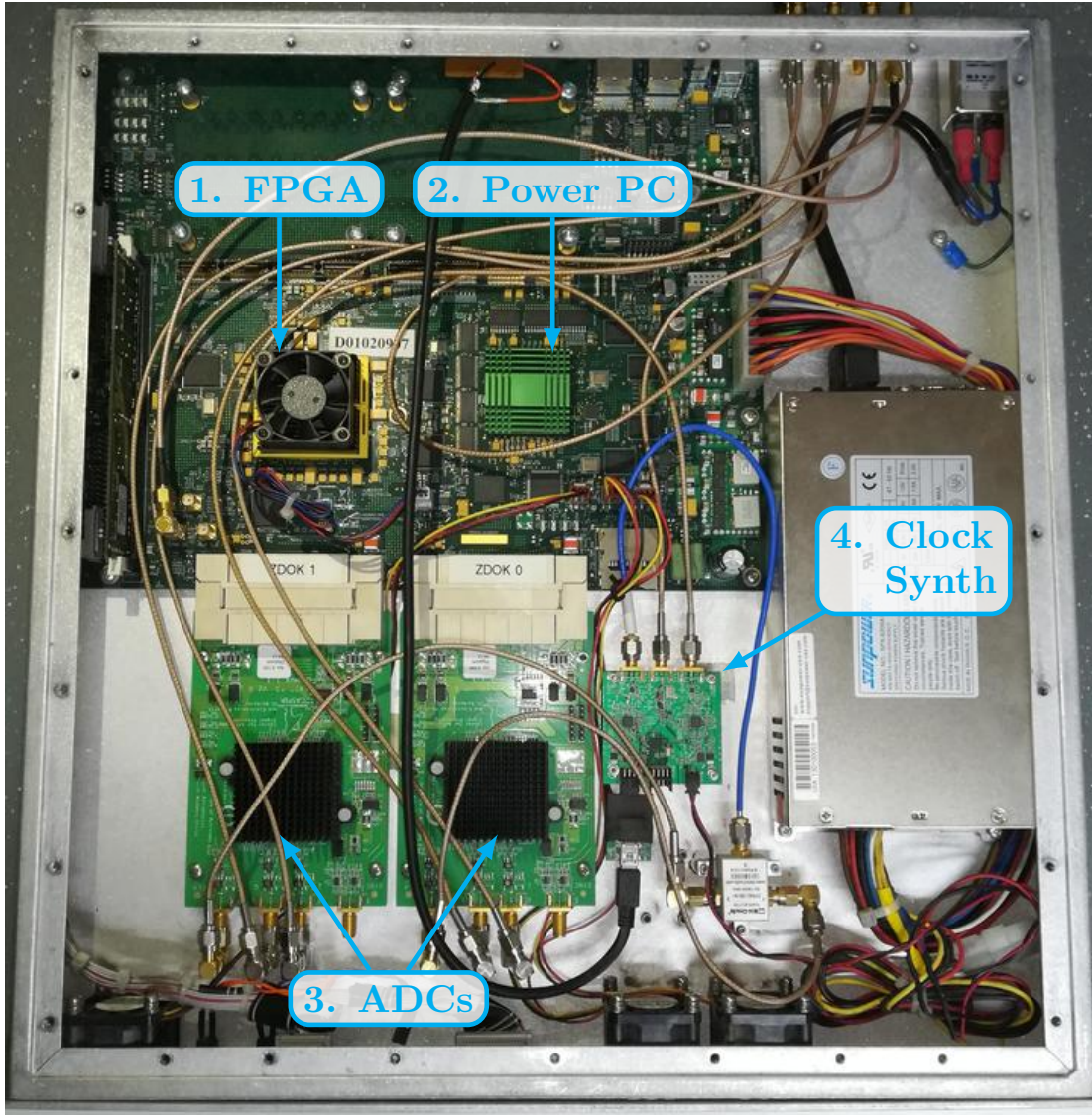
In (8.35) the triangular inequality is used. Similarly for $|J_{2,n}|$,

$$|J_{2,n}| \leq \frac{\frac{r_2}{r_1} + 1}{\left(\frac{r_2}{r_1}\right)^2 + 1} |I_{2,n}|. \quad (8.39)$$

Then it is proven that for the RFI filter, the multiple RFI scenario is equivalent to the high noise scenario.

8.3 List of Datasheets

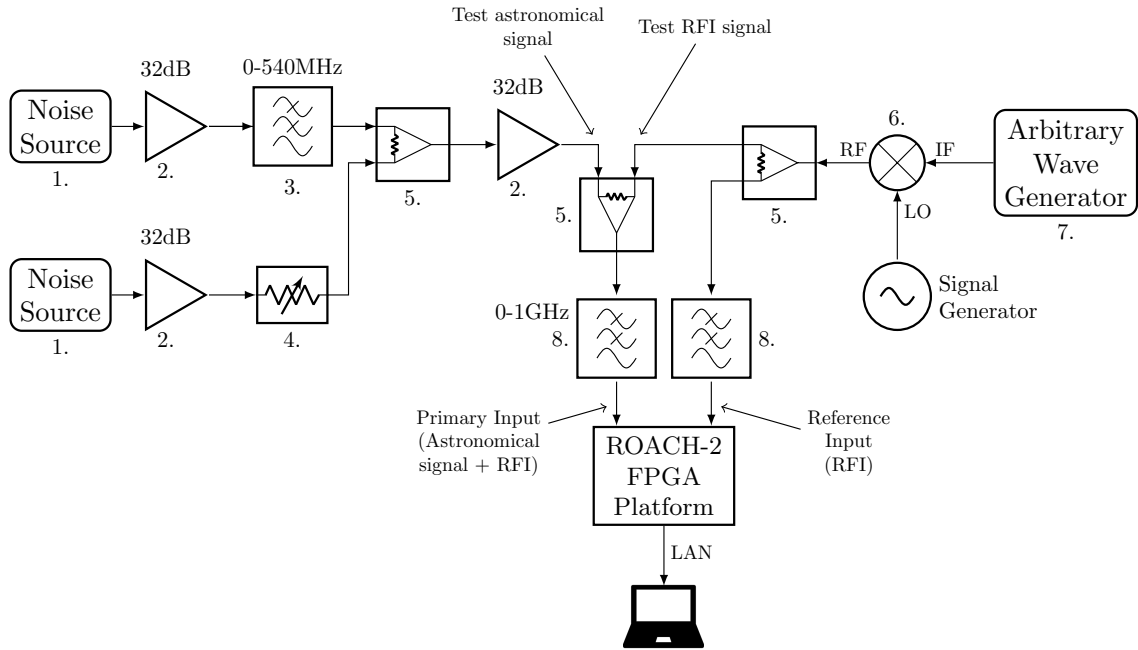
8.3.1 ROACH2 Hardware



Label	Component	Datasheet/webpage link
1.	Xilinx Virtex-6	https://bit.ly/2DvKLM6
2.	440EPx PowerPC Processor	https://bit.ly/2xrXAlp
3.	e2V EV8AQ160 ADC	https://bit.ly/2psiFYt
4.	Valon 5007 Synthesizer	https://bit.ly/2xIXepN

Table 8.1: ROACH2 Components.

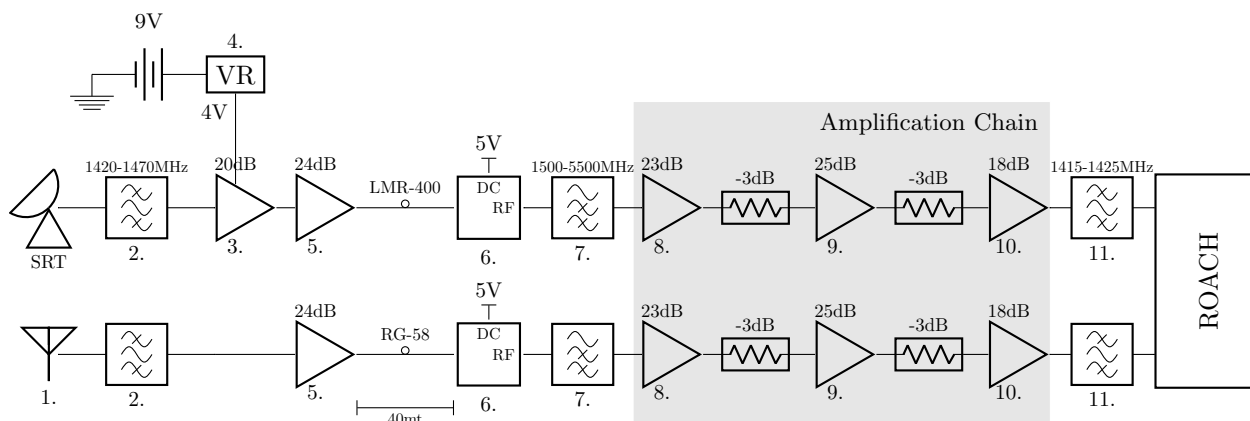
8.3.2 Laboratory Test Components



Label	Component	Datasheet/webpage link
1.	Agilent 346B Noise Source	https://bit.ly/20KrGXU
2.	Ebay RF Amplifier	https://ebay.to/2DkNecp
3.	Mini-Circuits VLFX-400 Low Pass Filter	https://bit.ly/2I8x7x8
4.	Agilent 355D Variable Attenuator	https://bit.ly/2PWn00C
5.	Mini-Circuits ZFSC-2-4+ Power Splitter	https://bit.ly/205mQao
6.	Mini-Circuits ZFM-2+ Frequency Mixer	https://bit.ly/2DnxRzM
7.	MHS-5200A Arbitrary Wave Generator	https://bit.ly/2DpAQbf
8.	Mini-Circuits VLF-800+ Low Pass Filter	https://bit.ly/2pshKat

Table 8.2: Laboratory Test Components.

8.3.3 SRT Test Components



Label	Component	Datasheet/webpage link
1.	Linx ANT-1.4-CW-HWR-SMA Dipole Antenna	https://bit.ly/2I7JDx9
2.	Mini-Circuits VBF-1445+ Band pass Filter	https://bit.ly/2pxzAsM
3.	Mini-Circuits ZX60-P162LN+ Low Noise Amplifier	https://bit.ly/2I9DVuq
4.	LM137T Voltage Regulator	https://bit.ly/2NIwSiw
5.	Agilent ATF-34143 Low Noise Amplifier	https://bit.ly/204W7ej
6.	Mini-Circuits ZFBT-4R2G+ Bias Tee	https://bit.ly/2QRoUS5
7.	Mini-Circuits VHF-1500+ High Pass Filter	https://bit.ly/2Dmzm1q
8.	Ebay RF Amplifier	https://ebay.to/2DkNecp
9.	Ebay RF Amplifier	https://ebay.to/2pw5q9j
10.	Ebay RF Amplifier	https://ebay.to/2xFol54
11.	Radio Astronomy Supplies 1420MHz Band Pass Filter	https://bit.ly/2pw5Kox

Table 8.3: SRT Test Components.

Number used as ILOGICE1s:	0			
Number used as ISERDESE1s:	64			
Number of OLOGICE1/OSERDESE1s:	2 out of	1,080	1%	
Number used as OLOGICE1s:	2			
Number used as OSERDESE1s:	0			
Number of BSCAMs:	0 out of	4	0%	
Number of BUFHCEs:	0 out of	216	0%	
Number of BUFIDDQs:	0 out of	108	0%	
Number of BUFRRs:	2 out of	54	3%	
Number of LOCed BUFRRs:	2 out of	2	100%	
Number of CAPTUREs:	0 out of	1	0%	
Number of DSP48E1s:	948 out of	2,016	47%	
Number of EFUSE_USRs:	0 out of	1	0%	
Number of FRAME_ECCs:	0 out of	1	0%	
Number of GTXE1s:	0 out of	36	0%	
Number of IBUFDS_GTXE1s:	0 out of	18	0%	
Number of ICAPs:	0 out of	2	0%	
Number of IDELAYCTRLs:	4 out of	27	14%	
Number of IODELAYE1s:	64 out of	1,080	5%	
Number of MMCM_ADVs:	3 out of	18	16%	
Number of PCIE_2_0s:	0 out of	2	0%	
Number of STARTUPS:	1 out of	1	100%	
Number of SYSMONs:	0 out of	1	0%	
Number of TEMAC_SINGLES:	0 out of	4	0%	

Overall effort level (-ol): High
Router effort level (-rl): High

Starting initial Timing Analysis. REAL time: 2 mins 47 secs
Finished initial Timing Analysis. REAL time: 2 mins 52 secs

WARNING:Par:288 - The signal
kestfilt_4096ch_1080mhz_asiaa_adc5g1/kestfilt_4096ch_1080mhz_asiaa_adc5g1/FIFO/BU2/U0/grf.rf/mem/gdm.dm/Mram_RAM16_RAMD_D1_0 has no load.
PAR will not attempt to route this signal.

WARNING:Par:288 - The signal
kestfilt_4096ch_1080mhz_asiaa_adc5g1/kestfilt_4096ch_1080mhz_asiaa_adc5g1/FIFO/BU2/U0/grf.rf/mem/gdm.dm/Mram_RAM18_RAMD_D1_0 has no load.
PAR will not attempt to route this signal.

WARNING:Par:288 - The signal
kestfilt_4096ch_1080mhz_asiaa_adc5g1/kestfilt_4096ch_1080mhz_asiaa_adc5g1/FIFO/BU2/U0/grf.rf/mem/gdm.dm/Mram_RAM21_RAMD_D1_0 has no load.
PAR will not attempt to route this signal.

WARNING:Par:288 - The signal
kestfilt_4096ch_1080mhz_asiaa_adc5g1/kestfilt_4096ch_1080mhz_asiaa_adc5g1/FIFO/BU2/U0/grf.rf/mem/gdm.dm/Mram_RAM22_RAMB_D1_DPO has no load.
PAR will not attempt to route this signal.

WARNING:Par:288 - The signal
kestfilt_4096ch_1080mhz_asiaa_adc5g1/kestfilt_4096ch_1080mhz_asiaa_adc5g1/FIFO/BU2/U0/grf.rf/mem/gdm.dm/Mram_RAM22_RAMC_D1_DPO has no load.
PAR will not attempt to route this signal.

WARNING:Par:288 - The signal
kestfilt_4096ch_1080mhz_asiaa_adc5g1/kestfilt_4096ch_1080mhz_asiaa_adc5g1/FIFO/BU2/U0/grf.rf/mem/gdm.dm/Mram_RAM22_RAMD_D1_0 has no load.
PAR will not attempt to route this signal.

WARNING:Par:288 - The signal
kestfilt_4096ch_1080mhz_asiaa_adc5g1/kestfilt_4096ch_1080mhz_asiaa_adc5g1/FIFO/BU2/U0/grf.rf/mem/gdm.dm/Mram_RAM15_RAMD_D1_0 has no load.
PAR will not attempt to route this signal.

WARNING:Par:288 - The signal
kestfilt_4096ch_1080mhz_asiaa_adc5g1/kestfilt_4096ch_1080mhz_asiaa_adc5g1/FIFO/BU2/U0/grf.rf/mem/gdm.dm/Mram_RAM6_RAMD_D1_0 has no load.
PAR will not attempt to route this signal.

WARNING:Par:288 - The signal
kestfilt_4096ch_1080mhz_asiaa_adc5g1/kestfilt_4096ch_1080mhz_asiaa_adc5g1/FIFO/BU2/U0/grf.rf/mem/gdm.dm/Mram_RAM14_RAMD_D1_0 has no load.
PAR will not attempt to route this signal.

WARNING:Par:288 - The signal
kestfilt_4096ch_1080mhz_asiaa_adc5g1/kestfilt_4096ch_1080mhz_asiaa_adc5g1/FIFO/BU2/U0/grf.rf/mem/gdm.dm/Mram_RAM20_RAMD_D1_0 has no load.
PAR will not attempt to route this signal.

WARNING:Par:288 - The signal
kestfilt_4096ch_1080mhz_asiaa_adc5g1/kestfilt_4096ch_1080mhz_asiaa_adc5g1/FIFO/BU2/U0/grf.rf/mem/gdm.dm/Mram_RAM19_RAMD_D1_0 has no load.
PAR will not attempt to route this signal.

WARNING:Par:288 - The signal
kestfilt_4096ch_1080mhz_asiaa_adc5g1/kestfilt_4096ch_1080mhz_asiaa_adc5g1/FIFO/BU2/U0/grf.rf/mem/gdm.dm/Mram_RAM13_RAMD_D1_0 has no load.
PAR will not attempt to route this signal.

WARNING:Par:288 - The signal
kestfilt_4096ch_1080mhz_asiaa_adc5g1/kestfilt_4096ch_1080mhz_asiaa_adc5g1/FIFO/BU2/U0/grf.rf/mem/gdm.dm/Mram_RAM7_RAMD_D1_0 has no load.
PAR will not attempt to route this signal.

WARNING:Par:288 - The signal
kestfilt_4096ch_1080mhz_asiaa_adc5g1/kestfilt_4096ch_1080mhz_asiaa_adc5g1/FIFO/BU2/U0/grf.rf/mem/gdm.dm/Mram_RAM8_RAMD_D1_0 has no load.
PAR will not attempt to route this signal.

WARNING:Par:288 - The signal
kestfilt_4096ch_1080mhz_asiaa_adc5g1/kestfilt_4096ch_1080mhz_asiaa_adc5g1/FIFO/BU2/U0/grf.rf/mem/gdm.dm/Mram_RAM17_RAMD_D1_0 has no load.
PAR will not attempt to route this signal.

WARNING:Par:288 - The signal
kestfilt_4096ch_1080mhz_asiaa_adc5g1/kestfilt_4096ch_1080mhz_asiaa_adc5g1/FIFO/BU2/U0/grf.rf/mem/gdm.dm/Mram_RAM2_RAMD_D1_0 has no load.
PAR will not attempt to route this signal.

WARNING:Par:288 - The signal
kestfilt_4096ch_1080mhz_asiaa_adc5g1/kestfilt_4096ch_1080mhz_asiaa_adc5g1/FIFO/BU2/U0/grf.rf/mem/gdm.dm/Mram_RAM5_RAMD_D1_0 has no load.
PAR will not attempt to route this signal.

WARNING:Par:288 - The signal
kestfilt_4096ch_1080mhz_asiaa_adc5g1/kestfilt_4096ch_1080mhz_asiaa_adc5g1/FIFO/BU2/U0/grf.rf/mem/gdm.dm/Mram_RAM3_RAMD_D1_0 has no load.
PAR will not attempt to route this signal.

WARNING:Par:288 - The signal
kestfilt_4096ch_1080mhz_asiaa_adc5g1/kestfilt_4096ch_1080mhz_asiaa_adc5g1/FIFO/BU2/U0/grf.rf/mem/gdm.dm/Mram_RAM10_RAMD_D1_0 has no load.
PAR will not attempt to route this signal.

WARNING:Par:288 - The signal
kestfilt_4096ch_1080mhz_asiaa_adc5g1/kestfilt_4096ch_1080mhz_asiaa_adc5g1/FIFO/BU2/U0/grf.rf/mem/gdm.dm/Mram_RAM1_RAMD_D1_0 has no load.
PAR will not attempt to route this signal.

WARNING:Par:288 - The signal
kestfilt_4096ch_1080mhz_asiaa_adc5g1/kestfilt_4096ch_1080mhz_asiaa_adc5g1/FIFO/BU2/U0/grf.rf/mem/gdm.dm/Mram_RAM11_RAMD_D1_0 has no load.
PAR will not attempt to route this signal.

WARNING:Par:288 - The signal

Updating file: system.ncd with current fully routed design.

Phase 7 : 0 unrouted; (Setup:192, Hold:76937, Component Switching Limit:0) REAL time: 49 mins 24 secs
 Phase 8 : 0 unrouted; (Setup:192, Hold:76937, Component Switching Limit:0) REAL time: 49 mins 24 secs
 Phase 9 : 0 unrouted; (Setup:192, Hold:0, Component Switching Limit:0) REAL time: 49 mins 34 secs
 Phase 10 : 0 unrouted; (Setup:0, Hold:0, Component Switching Limit:0) REAL time: 50 mins 17 secs
 Total REAL time to Router completion: 50 mins 17 secs
 Total CPU time to Router completion: 53 mins 11 secs

Partition Implementation Status

No Partitions were found in this design.

Generating "PAR" statistics.

Generating Clock Report

Clock Net	Resource	Locked	Fanout	Net Skew(ns)	Max Delay(ns)
adc0_clk	BUFGCTRL_X0Y5	No	41852	0.749	2.709
adc0_psclk	BUFGCTRL_X0Y31	No	1188	0.536	2.501
sys_clk	BUFGCTRL_X0Y2	No	4	0.009	2.191
adc1_clk	BUFGCTRL_X0Y3	No	375	0.427	2.447
kestfilt_4096ch_1080					
mhz_asiaa_adc5g1/ctr					
l_clk90_out	BUFGCTRL_X0Y4	No	32	0.136	2.409
adc0_clk90	BUFGCTRL_X0Y6	No	32	0.148	2.350
infrastructure_inst/clk_200	BUFGCTRL_X0Y0	No	4	0.186	2.239
kestfilt_4096ch_1080					
mhz_asiaa_adc5g0/kes					
tfilt_4096ch_1080mhz					
_asiaa_adc5g0/MMCM0_ML_NEW_I1	Local		3	0.000	2.000
kestfilt_4096ch_1080					
mhz_asiaa_adc5g0/kes					
tfilt_4096ch_1080mhz					
_asiaa_adc5g0/MMCM0_ML_NEW_OUT	Local		2	0.000	0.359
kestfilt_4096ch_1080					
mhz_asiaa_adc5g1/kes					
tfilt_4096ch_1080mhz					
_asiaa_adc5g1/MMCM0_ML_NEW_I1	Local		3	0.000	3.977
kestfilt_4096ch_1080					
mhz_asiaa_adc5g1/kes					
tfilt_4096ch_1080mhz					
_asiaa_adc5g1/MMCM0_ML_NEW_OUT	Local		2	0.000	0.359
infrastructure_inst/infrastructure_inst/MMCM_BASE_sys_clk_ML_NEW_I1	Local		3	0.000	2.537
infrastructure_inst/infrastructure_inst/infrastructure_inst/MMCM_BASE_sys_clk_ML_NEW_OUT	Local		2	0.000	0.366
MMCM_PHASE_CALIBRATI					
DN_ML_LUT2_596_ML_NE					
W_CLK	Local		3	0.120	0.824
MMCM_PHASE_CALIBRATI					
DN_ML_LUT2_588_ML_NE					
W_CLK	Local		3	0.274	0.746
MMCM_PHASE_CALIBRATI					
DN_ML_LUT2_580_ML_NE					
W_CLK	Local		3	0.742	1.098

* Net Skew is the difference between the minimum and maximum routing only delays for the net. Note this is different from Clock Skew which is reported in TRCE timing report. Clock Skew is the difference between

the minimum and maximum path delays which includes logic delays.

* The fanout is the number of component pins not the individual BEL loads, for example SLICE loads not FF loads.

Timing Score: 0 (Setup: 0, Hold: 0, Component Switching Limit: 0)

Number of Timing Constraints that were not applied: 9

Asterisk (*) preceding a constraint indicates it was not met. This may be due to a setup or hold violation.

Constraint	Check	Worst Case Slack	Best Case Achievable	Timing Errors	Timing Score
PERIOD analysis for net "kestfilt_4096ch_1080mhz_asiaa_adc5g0/kestfilt_4096ch_1080mhz_asiaa_adc5g0/mcmm_clkout1" derived from PERIOD analysis for net "kestfilt_4096ch_1080mhz_asiaa_adc5g0/kestfilt_4096ch_1080mhz_asiaa_adc5g0/adc_clk_div" derived from NET "kestfilt_4096ch_1080mhz_asiaa_adc5g0/kestfilt_4096ch_1080mhz_asiaa_adc5g0/adc_clk" PERIOD = 3.7037 ns HIGH 50%	SETUP HOLD	0.006ns 0.003ns	7.401ns	0 0	0 0
TS_epb_clk_in = PERIOD TIMEGRP "epb_clk_in" 67 MHz HIGH 50%	SETUP HOLD	0.111ns 0.059ns	14.814ns	0 0	0 0
TS_infrastructure_inst_infrastructure_inst_clk_200_mmcm = PERIOD TIMEGRP "infrastructure_inst_infrastructure_inst_clk_200_mmcm" TS_sys_clk_n * 2 HIGH 50%	MINPERIOD	0.239ns	4.761ns	0	0
PERIOD analysis for net "kestfilt_4096ch_1080mhz_asiaa_adc5g1/kestfilt_4096ch_1080mhz_asiaa_adc5g1/mcmm_clkout1" derived from PERIOD analysis for net "kestfilt_4096ch_1080mhz_asiaa_adc5g1/kestfilt_4096ch_1080mhz_asiaa_adc5g1/adc_clk_div" derived from NET "kestfilt_4096ch_1080mhz_asiaa_adc5g1/kestfilt_4096ch_1080mhz_asiaa_adc5g1/adc_clk" PERIOD = 3.7037 ns HIGH 50%	SETUP HOLD	1.329ns 0.071ns	6.078ns	0 0	0 0
NET "kestfilt_4096ch_1080mhz_asiaa_adc5g0/kestfilt_4096ch_1080mhz_asiaa_adc5g0/adc_clk" PERIOD = 3.7037 ns HIGH 50%	MINPERIOD	2.037ns	1.666ns	0	0
NET "kestfilt_4096ch_1080mhz_asiaa_adc5g1/kestfilt_4096ch_1080mhz_asiaa_adc5g1/adc_clk" PERIOD = 3.7037 ns HIGH 50%	MINPERIOD	2.037ns	1.666ns	0	0
PERIOD analysis for net "kestfilt_4096ch_1080mhz_asiaa_adc5g0/kestfilt_4096ch_1080mhz_asiaa_adc5g0/adc_clk_div" derived from NET "kestfilt_4096ch_1080mhz_asiaa_adc5g0/kestfilt_4096ch_1080mhz_asiaa_adc5g0/adc_clk" PERIOD = 3.7037 ns HIGH 50%	MINLOWPULSE	3.406ns	4.000ns	0	0
PERIOD analysis for net "kestfilt_4096ch_1080mhz_asiaa_adc5g1/kestfilt_4096ch_1080mhz_asiaa_adc5g1/adc_clk_div" derived from NET "kestfilt_4096ch_1080mhz_asiaa_adc5g1/kestfilt_4096ch_1080mhz_asiaa_adc5g1/adc_clk" PERIOD = 3.7037 ns HIGH 50%	MINLOWPULSE	3.406ns	4.000ns	0	0
TS_sys_clk_n = PERIOD TIMEGRP "sys_clk_n" 100 MHz HIGH 50%	MINLOWPULSE	6.000ns	4.000ns	0	0
PERIOD analysis for net "kestfilt_4096ch_1080mhz_asiaa_adc5g0/kestfilt_4096ch_1080mhz_asiaa_adc5g0/mcmm_clkout2" derived from PERIOD analysis for net "kestfilt_4096ch_1080mhz_asiaa_adc5g0/kestfilt_4096ch_1080mhz_asiaa_adc5g0/adc_clk_div" derived from NET "kestfilt_4096ch_1080mhz_asiaa_adc5g0/kestfilt_4096ch_1080mhz_asiaa_adc5g0/adc_clk" PERIOD = 3.7037 ns HIGH 50%	MINPERIOD	5.978ns	1.429ns	0	0
PERIOD analysis for net "kestfilt_4096ch_1080mhz_asiaa_adc5g1/kestfilt_4096ch_1080mhz_asiaa_adc5g1/mcmm_clkout2" derived from PERIOD analysis for net "kestfilt_4096ch_1080mhz_asiaa_adc5g1/kestfilt_4096ch_1080mhz_asiaa_adc5g1/adc_clk_div" derived from NET "kestfilt_4096ch_1080mhz_asiaa_adc5g1/kestfilt_4096ch_1080mhz_asiaa_adc5g1/adc_clk" PERIOD = 3.7037 ns HIGH 50%	MINPERIOD	5.978ns	1.429ns	0	0

ns HIGH 50%						
TS_infrastructure_inst_infrastructure_ins	SETUP	7.086ns	2.914ns	0	0	0
t_sys_clk_mmcm = PERIOD TIMEGRP	HOLD	0.109ns		0	0	0
infrastructure_inst_infrastructure_inst_s						
ys_clk_mmcm" TS_sys_clk_n	HIGH 50					
%						
TS_sys_clk = PERIOD TIMEGRP "TNM_sys_clk"	MINHIGHPULSE	9.168ns	0.832ns	0	0	0
100 MHz HIGH 50%						

Derived Constraint Report

Review Timing Report for more details on the following derived constraints.

To create a Timing Report, run "trce -v 12 -fastpaths -o design_timing_report design.ncd design.pcf"

or "Run Timing Analysis" from Timing Analyzer (timingan).

Derived Constraints for kestfilt_4096ch_1080mhz_asiaa_adc5g0/kestfilt_4096ch_1080mhz_asiaa_adc5g0/adc_clk

Constraint	Period Requirement	Actual Period		Timing Errors		Paths Analyzed	
		Direct	Derivative	Direct	Derivative	Direct	Derivative
kestfilt_4096ch_1080mhz_asiaa_a dc5g0/kestfilt_4096ch_1080mhz_a siaa_adc5g0/adc_clk	3.704ns	1.666ns	3.700ns	0	0	0	97679237
kestfilt_4096ch_1080mhz_asiaa_ adc5g0/kestfilt_4096ch_1080mhz_ _asiaa_adc5g0/adc_clk_div	7.407ns	4.000ns	7.401ns	0	0	0	97679237
kestfilt_4096ch_1080mhz_asiaa _adc5g0/kestfilt_4096ch_1080m hz_asiaa_adc5g0/mmcm_clkout2	7.407ns	1.429ns	N/A	0	0	0	0
kestfilt_4096ch_1080mhz_asiaa _adc5g0/kestfilt_4096ch_1080m hz_asiaa_adc5g0/mmcm_clkout1	7.407ns	7.401ns	N/A	0	0	97679237	0

Derived Constraints for kestfilt_4096ch_1080mhz_asiaa_adc5g1/kestfilt_4096ch_1080mhz_asiaa_adc5g1/adc_clk

Constraint	Period Requirement	Actual Period		Timing Errors		Paths Analyzed	
		Direct	Derivative	Direct	Derivative	Direct	Derivative
kestfilt_4096ch_1080mhz_asiaa_a dc5g1/kestfilt_4096ch_1080mhz_a siaa_adc5g1/adc_clk	3.704ns	1.666ns	3.039ns	0	0	0	3114
kestfilt_4096ch_1080mhz_asiaa_ adc5g1/kestfilt_4096ch_1080mhz_ _asiaa_adc5g1/adc_clk_div	7.407ns	4.000ns	6.078ns	0	0	0	3114
kestfilt_4096ch_1080mhz_asiaa _adc5g1/kestfilt_4096ch_1080m hz_asiaa_adc5g1/mmcm_clkout2	7.407ns	1.429ns	N/A	0	0	0	0
kestfilt_4096ch_1080mhz_asiaa _adc5g1/kestfilt_4096ch_1080m hz_asiaa_adc5g1/mmcm_clkout1	7.407ns	6.078ns	N/A	0	0	3114	0

Derived Constraints for TS_sys_clk_n

Constraint	Period Requirement	Actual Period		Timing Errors		Paths Analyzed	
		Direct	Derivative	Direct	Derivative	Direct	Derivative
TS_sys_clk_n	10.000ns	4.000ns	9.522ns	0	0	0	186
TS_infrastructure_inst_infrast _ructure_inst_sys_clk_mmcm	10.000ns	2.914ns	N/A	0	0	186	0
TS_infrastructure_inst_infrast _ructure_inst_clk_200_mmcm	5.000ns	4.761ns	N/A	0	0	0	0

All constraints were met.

Generating Pad Report.

All signals are completely routed.

WARNING:Par:283 - There are 48 loadless signals in this design. This design will cause Bitgen to issue DRC warnings.

Total REAL time to PAR completion: 50 mins 59 secs

Total CPU time to PAR completion: 53 mins 52 secs

Peak Memory Usage: 5091 MB

Placer: Placement generated during map.

Routing: Completed - No errors found.

Timing: Completed - No errors found.

Number of error messages: 0

Number of warning messages: 50

Number of info messages: 0

Writing design to file system.ncd

PAR done!

8.5 RFI Filter Model Figures

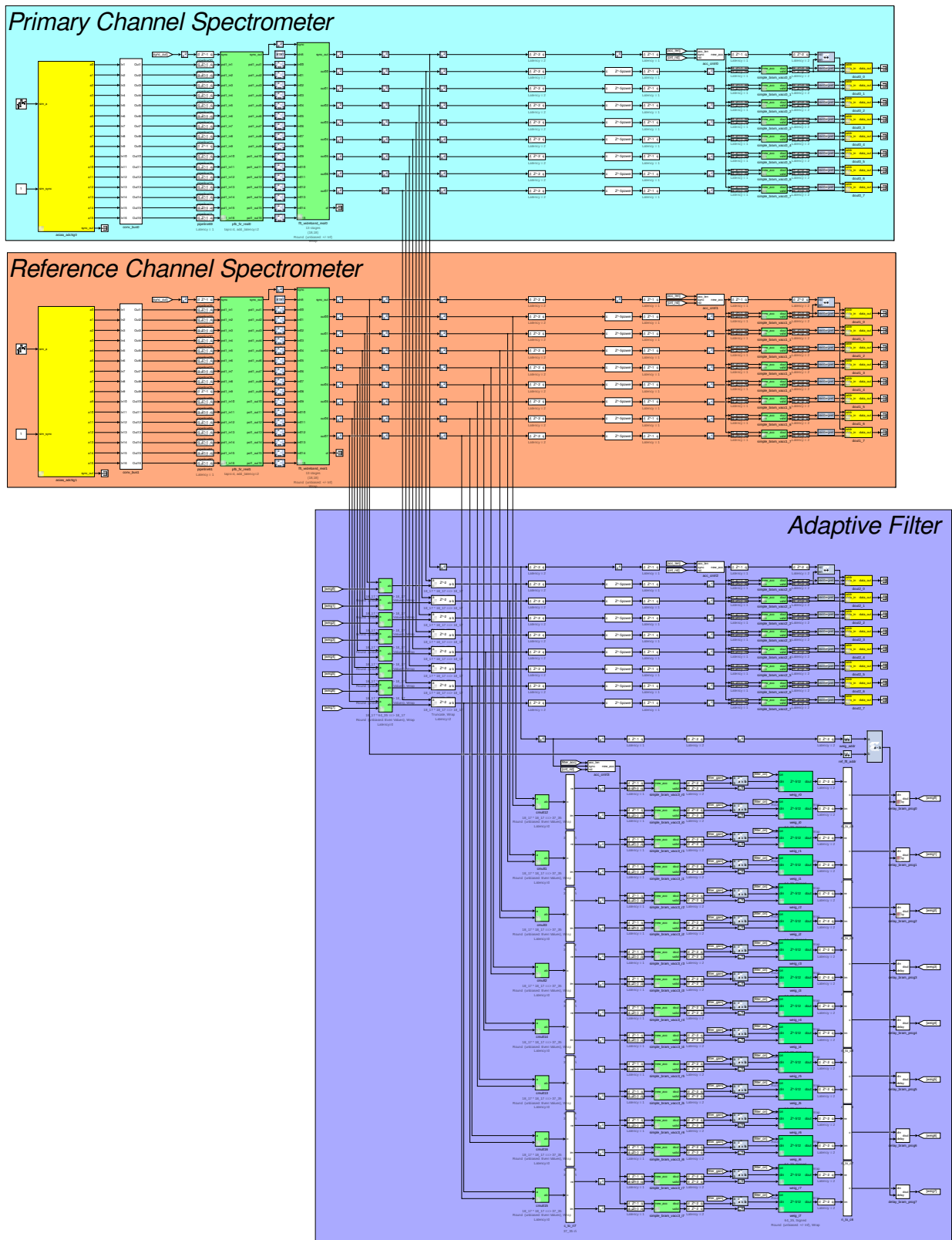


Figure 8.2: RFI filter full model. Some control signals were removed to avoid the clutter.

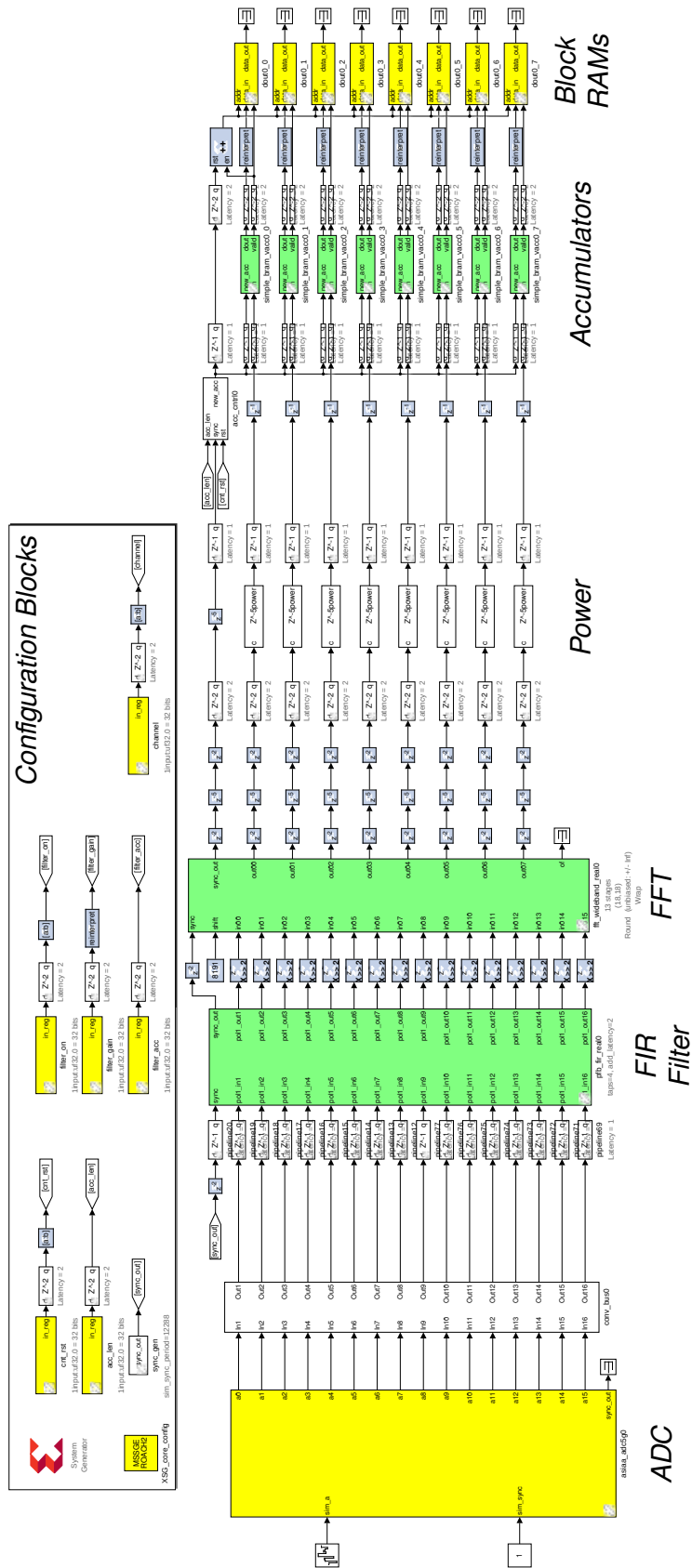


Figure 8.3: RFI filter spectrometer. This circuit is used for both the primary and the reference channel, while the filter output uses the last segment (power, accumulators and block RAMs). The 16 lines (8 after the FFT) are the parallel dataflows inside the FPGA.

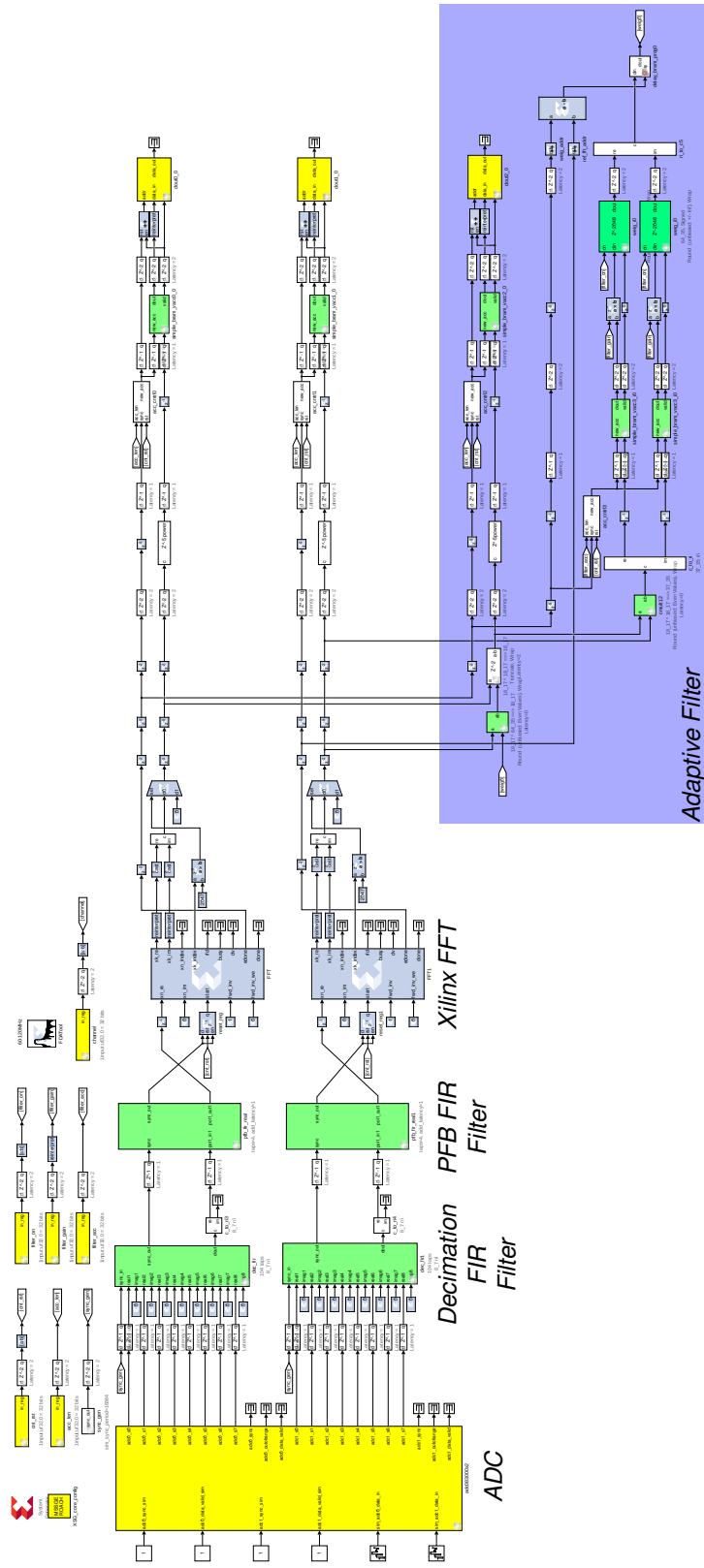


Figure 8.5: RFI filter for the FM test. The changes from the original model are the addition of the decimation FIR filter, the use of a ROACH1 ADC, and the use of the Xilinx FFT block instead of the one from CASPER, as is more efficient for single input signals. This same model with different FIR filter coefficients is used for the radio telescope test.